

Scuola Normale Superiore

Tesi di Perfezionamento in Fisica

**Modeling the interstellar medium of high
redshift galaxies**

Supervisor: Prof. Andrea Ferrara

Co-supervisor: Dott.ssa Simona Gallerani

Candidate: Livia Vallini



List of acronym and symbols

Acronym	Extended name
AGN	Active Galactic Nucleus
ALMA	Atacama Large Millimeter-submillimeter Array
CMB	Cosmic Microwave Background
CNM	Cold Neutral Medium
CO	Carbon Monoxide
CO SLED	Carbon Monoxide Spectral Line Energy Distribution
FIR	Far Infrared
FWHM	Full width half maximum
FUV	Far Ultraviolet (non ionizing) band: $6 < h\nu < 13.6 \text{ eV}$
GADGET	GALaxies with Dark matter and Gas intEracT
HIM	Hot Ionized Medium
HST	Hubble Space Telescope
IGM	Intergalactic Medium
ISM	Interstellar Medium
LAE	Lyman Alpha Emitter
LBG	Lyman Break Galaxy
LTE	Local Thermal Equilibrium
LW	Lyman Werner
MC	Molecular Cloud
PAH	Polycyclic Aromatic Hydrocarbons
PDR	Photodissociation Region
PDF	Probability Distribution Function
PdBI	Plateau de Bure Interferometer
<i>PopIII</i>	Population III
SED	Spectral Energy Distribution
SFR	Star Formation Rate
JWST	James Webb Space Telescope
WIM	Warm Ionized Medium
WNM	Warm Neutral Medium
VLT	Very Large Telescope

Symbol	Extended name
$a(t)$	scale factor
$A(\lambda)$	dust extinction at wavelength λ
A_{ul}	Einstein coefficient of spontaneous emission
$B_\nu(T)$	Planck function
B_{ul} (B_{lu})	stimulated emission (absorption) coefficients
C_{ul} (C_{lu})	collisional de-excitation (excitation) rates
[C II]	ionized carbon
ε	line emissivity
f_{esc}	escape fraction of H ionizing photons
Φ	gravitational potential
G_0	FUV flux scaled to the Habing value
Γ_{pe}	Heating rate due to photoelectric effect on dust grains
Γ_{CR}	Heating rate due to cosmic rays
Γ_{XR}	Heating rate due to X-rays
[H I]	neutral hydrogen
[H II]	ionized hydrogen
J	rotational quantum number
k_B	Boltzman constant
Ly α	Lyman- α
Λ_i^m	Cooling rate for the metal \mathcal{M} for collision with the i -th species
Λ_{gr}	Cooling rate due to the recombination on dust grains
λ_J	Jeans length
M_J	Jeans Mass
\mathcal{M}	Mach number
n_H	number density of hydrogen atoms
n_e	number density of free electrons
n_{crit}	critical density
[N II]	ionized nitrogen
[O I]	neutral oxygen
[O III]	doubly ionized oxygen
Ω_m	density parameter for the matter
Ω_b	density parameter for the baryons
\mathcal{R}	rate coefficient for H ₂ formation on dust grains

Continued on next page

Symbol	Extended name
r_d	dust grain radius
ρ	material density of the gas
T_d	dust temperature
τ	optical depth
x_e	ionized fraction
Z_*	metallicity of the stars
Z	gas metallicity

Abstract

THE NATURE of the galaxies that formed within the first billion year of the Cosmic history is still poorly constrained, despite observations performed with increasingly sensitive telescopes and sophisticated cosmological simulations running on powerful computers. Even if we are living in a golden era for the extragalactic astrophysics, several fundamental questions are only partially answered:

1. Are the first galaxies that appeared in the Universe similar to those observed at later epochs?
2. What is the metal and dust content of these galaxies?
3. How much the metal abundance affects the physical conditions of their interstellar medium (ISM)?
4. What are the thermal and dynamical properties of various gas phases of their ISM?

In the near future, an huge breakthrough in solving these crucial issues will be achieved with the Atacama Large Millimeter/submillimeter Array (ALMA), the most powerful millimeter/sub-millimeter interferometer on the Earth. One of the ALMA scientific goals is to observe the redshifted far-infrared (FIR) metal cooling and molecular lines arising from the interstellar medium of the galaxies that emerged from the cosmic Dark Ages billions of years ago. So far, the mere detection of these objects has been the main purpose of the observational campaigns, however, with its unprecedented sensitivity and spatial resolution, ALMA will be able to revolutionize the observational Cosmology revealing the cold gas and the dust *within* these galaxies. The aim of this work is to devise a self-consistent theoretical model describing the ISM properties of high redshift galaxies that allows

to predict the luminosities of various metal and molecular lines observable with ALMA. We want to study the correlation between the line luminosities and fundamental galaxy properties, such as the star formation rate (SFR) and the metallicity (Z). We perform high resolution cosmological simulations of star forming galaxies at the end of the Epoch of Reionization ($z \simeq 6$), and we build on top of them a sub-grid model describing the cooling and the heating processes that take place in the neutral diffuse ISM. While the cosmological simulation allows to follow, on Mpc scales, the galaxy formation starting from the primordial quantum fluctuations, the sub-grid model provides a sub-kpc description of the thermodynamic equilibrium within the ISM. The Thesis is structured as follows:

1. In Chapter 1, we present the standard model for the structure formation in the Universe, we describe the main processes shaping the evolution of the Reionization, and the observational techniques adopted to detect high redshift galaxies.
2. In Chapter 2 we discuss in details the physics of the thermodynamic equilibrium of the ISM and that of the molecular clouds.
3. The analytical model developed to infer the abundance of molecular gas, and the luminosity of molecular tracers, in a sample of simulated high redshift galaxies is outlined in Chapter 3.
4. Chapter 4 is focused on the sub-grid model constructed during this Thesis to describe the thermodynamical equilibrium of the neutral diffuse gas in the ISM of the high redshifts galaxies.
5. The contribution of the photodissociation regions to the the far-infrared line emissivity is outlined in Chapter 5.
6. In the subsequent Chapter we discuss the relation between FIR line luminosity, the star formation rate, and the metallicity of high- z galaxies.
7. The predictions achieved in this work have been successfully tested against the few sub-millimeter data from high- z galaxies so far available and they have been used as a theoretical support in several ALMA proposals. The reader can find an extensive discussion about these points in Chapter 7.
8. We present the conclusions and the future prospects in the last Chapter.

Contents

Abstract	v
Contents	1
1 The cosmic evolution	3
1.1 The cosmological model	3
1.2 From the Big Bang to the Dark Ages	5
1.3 The Dark Ages	7
1.4 First stars	12
1.5 The Epoch of Reionization	13
1.6 Observations at high redshift	15
2 The interstellar medium	23
2.1 The phases of the interstellar medium	23
2.2 Molecular clouds	26
2.3 Photodissociation regions	28
2.4 The dust	31
2.5 Heating processes in the diffuse neutral gas	33
2.6 Cooling processes in the diffuse neutral gas	36
3 Molecular hydrogen in LAEs	43
3.1 The cosmological simulations	45
3.2 Molecular hydrogen physics	47
3.3 Results	53
3.4 Summary	63
4 FIR line emission from the diffuse gas	67

4.1	Numerical Simulations	69
4.2	Multiphase ISM model	70
4.3	Results	74
4.4	Comparison with observations	75
4.5	ALMA predictions	77
4.6	Summary	77
5	FIR line emission from PDRs	81
5.1	The diffuse neutral medium	82
5.2	Including the molecular clouds	85
5.3	Far infrared line emission	86
5.4	The CO(6–5) emission	89
5.5	Summary and conclusions	92
6	The [C II]-SFR relation at high redshift	95
6.1	Physics of the [C II] emission	96
6.2	Results	100
6.3	[C II]-SFR relation	102
6.4	Summary and Discussion	104
7	Interpreting the observations	107
7.1	Searching [CII] line in $z > 6.5$ galaxies	107
7.2	ALMA observations of $z \approx 7$ galaxies	117
7.3	Summary	122
8	Conclusions	125
8.1	Novelty of the Thesis and future prospects	129
	Bibliography	131

The cosmic evolution 1

THE HUMAN BEING has always questioned the nature about its origins, its meaning and its end. The history of Science has known several heroic attempts to unveil the mysteries of the Universe, even with scarce or almost non-existent data to describe it. However, only at the beginning of the XXth century with the publication of the General Relativity theory (Einstein, 1916), the Cosmology from being a philosophic attempt to answer the most profound questions of human nature, became a precision Science. Modern Cosmology is founded on two pillars: the aforementioned theory of the General Relativity and the cosmological principle. The first one describes the space-time structure of the Universe as a result of the matter distribution, while the second states that the Universe appears the same to any observer, regardless of its position. According to that, the Universe, *on sufficiently large scales*, is isotropic and homogeneous.

In this Chapter we briefly discuss the standard cosmological model, and the formation of variety of structures that we see today in the Universe (clusters of galaxies, galaxies, stars, planets) from the original singularity of the Big Bang. We also provide an overview of the current status of the selection techniques and instruments developed to observe galaxies and stars at the end of the Epoch of Reionization. Our aim is to highlight the open questions concerning the first billion years of the cosmic history to answer which this Thesis has been conceived.

1.1 The cosmological model

In general relativity the space-time geometry is mathematically expressed by the so called *metric tensor* $g_{\mu\nu}$ which allows to measure the interval ds between two

events in the space-time:

$$ds^2 = g_{\mu\nu} dx^\mu dx^\nu \quad (1.1)$$

The appropriate expression of ds for a spatially homogeneous and isotropic space is the one that results from Friedman Robertson Walker (FRW) metric :

$$ds^2 = c^2 dt^2 - a(t) \left[\frac{dr^2}{1 - kr^2} - r^2(d\theta^2 + \sin^2\theta d\varphi^2) \right] \quad (1.2)$$

where $a(t)$ is the cosmic scale factor which describes the expansion of the Universe as function of time, k is the curvature, and (R, θ, φ) are the spherical comoving coordinates. In this scenario, all the cosmology is completely specified once we know k and $a(t)$.

The metric expressed in Eq. (1.2) enters in the Einstein field equations:

$$R_{\mu\nu} - \frac{1}{2}g_{\mu\nu}R = 8\pi GT_{\mu\nu} + \Lambda g_{\mu\nu} \quad (1.3)$$

where $R_{\mu\nu}$ is the Ricci tensor, describing the local curvature of space-time, R is the curvature scalar, $T_{\mu\nu} = (\rho c^2 + P)U^\mu U^\nu - g^{\mu\nu}P$ is the energy-momentum tensor and Λ is the cosmological constant . This equation drives, after the substitution of the FRW metric $g_{\mu\nu}$ and some algebraic manipulations, to the Friedman equation:

$$\left(\frac{\dot{a}}{a}\right)^2 \equiv H(t)^2 = \frac{8\pi G}{3}\rho - \frac{kc^2}{a^2} + \frac{\Lambda c^2}{3} \quad (1.4)$$

which relates the expansion of the Universe, mathematically indicated with the Hubble constant $H(t)$, to the matter-energy density.

The density ρ in Eq. (1.4) is the sum of three contributes $\rho = \rho_m + \rho_r + \rho_\Lambda$ where ρ_m is the non-relativistic matter energy density, ρ_r is the radiation energy density, and ρ_Λ is the vacuum energy density. If we define the critical density as:

$$\rho_c(t) = \frac{3H^2(t)}{8\pi G} \quad (1.5)$$

we can introduce the density parameter Ω for each type of energy density: $\Omega_m = \rho_m/\rho_c$, $\Omega_r = \rho_r/\rho_c$ and $\Omega_\Lambda = \rho_\Lambda/\rho_c$. The matter density parameter $\Omega_m = \Omega_{DM} + \Omega_b$ is the sum of the the Dark Matter (DM) and baryon contributions. With Ω_m , Ω_Λ and Ω_r denoting the present ($z = 0$) cosmological parameters, the Friedmann equation

becomes:

$$\frac{H(t)}{H_0} = \left[\frac{\Omega_m}{a^3} + \Omega_\Lambda + \frac{\Omega_r}{a^4} + \frac{\Omega_m}{a^2} \right] \quad (1.6)$$

where H_0 is the present value of the Hubble constant. The cosmological model is completely defined once the values of the density parameters are specified. Recent observations provided by [Planck Collaboration et al. \(2015\)](#) (Planck+WP) constrain the standard model in a relatively narrow range: $\Omega_m = 0.3089 \pm 0.0062$, $\Omega_\Lambda = 0.6911 \pm 0.0062$, and $H_0 = 100h \text{ km s}^{-1} \text{ Mpc}^{-1}$ with $h = 0.6774 \pm 0.0046$.

1.2 From the Big Bang to the Dark Ages

According to the standard cosmological model, the history of the Universe began ~ 13.7 billions years ago from a singularity; this event is referred as Big Bang. Immediately after, during a brief period at early epochs ($t \approx t^{-35} - t^{-33}$ s) called *Inflation* ([Linde, 1982](#)), the Universe increased its size by ~ 60 orders of magnitudes. As a result of this process, quantum fluctuations generated at the Big Bang were almost completely erased on large scales, remaining only on small scales as overdense seeds for the subsequent structure formation. Along with the expansion, the temperature T of the Universe was decreasing with the redshift, as $T \propto (1+z)$. Around $t \sim 3$ min, the temperature of the Universe reached $T \sim 10^9$ K, lower enough so that protons and neutrons could combine into atomic *nuclei* (H, deuterium, ^4He , traces of ^7Li and ^7Be). This process, called *Big Bang nucleosynthesis*, lasted until about ~ 20 minutes when the temperature became too low to allow nuclear fusion processes. The Universe remained hot enough for the matter to be fully ionized and efficiently coupled to the radiation for $t \sim 10^5$ yr. At $z \approx 1200$ the temperature decreased below ~ 3000 K so that protons and electrons could recombine to form neutral hydrogen atoms and, slightly after ($z \approx 1100$), the Universe became transparent to the propagation of light. Hence, though simple atomic nuclei formed within the first minutes after the Big Bang, thousands of years passed before the first electrically neutral *atoms* could appear. The relic radiation from the decoupling is observed today as a Cosmic Microwave Background (CMB), imaged and measured by several satellites such as COBE, WMAP and Planck.

The radiation has a black body spectrum with a mean temperature $T = 2.72548 \pm 0.00057$ K ([Fixsen, 2009](#)) and fluctuations (see Fig. 1.1) of order of $\sim 10^{-5}$ ([Planck Collaboration et al., 2013](#)) which reflect the density inhomogeneities caused by the

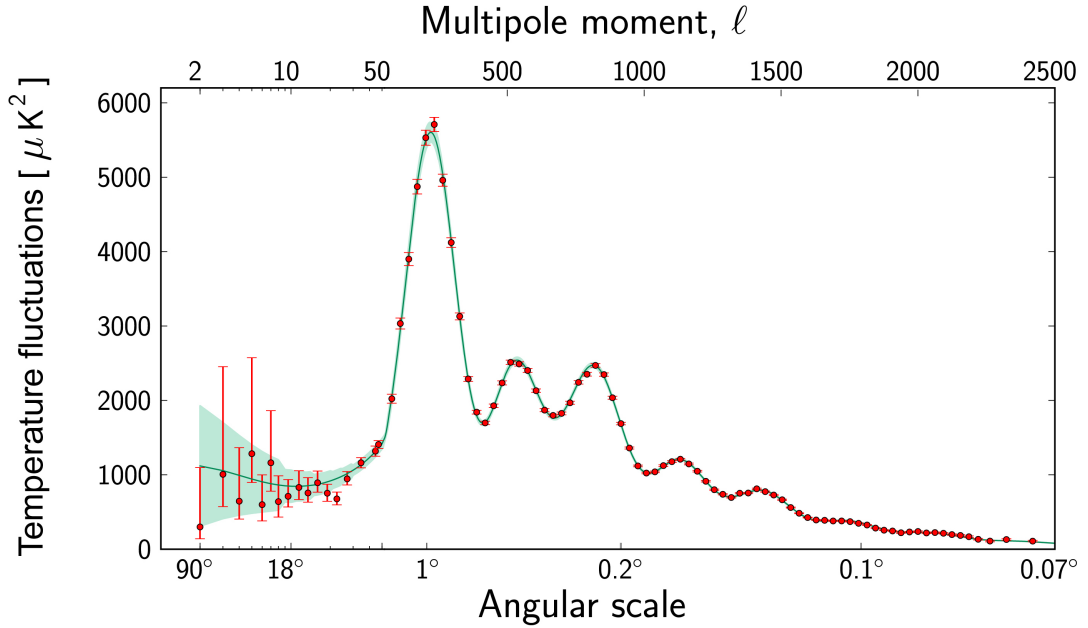


Figure 1.1: The temperature fluctuations in the CMB detected by the Planck satellite at different angular scales on the sky. The red dots are measurements made with Planck. The green curve represents the best fit of the 'standard model of cosmology' to the Planck data. The green shaded area around the curve shows the predictions of all the variations of the standard model that best agree with the data. Copyright: ESA and the Planck Collaboration.

quantum fluctuations not erased at the end of the Inflation.

Nowadays, the astronomer can use the CMB radiation to have a picture of the Universe when it was only ≈ 380000 yr old, but the farthest galaxy ever observed is at $z \approx 7.51$ (Finkelstein et al., 2013), when the Universe was only ≈ 700 Myr old. What happened in between? The epoch ranging from $z \approx 1100$ to $z \approx 30 - 20$ is called *Dark Ages* and it corresponds to the transition from a dark and relatively homogeneous Universe, to the complexity that we observe today. Around, $z \approx 30 - 20$ the first gravitationally bound objects were formed (metal free stars, galaxies) and complex chemical and radiative processes entered the scene. This event opened up the way to the Reionization of the Universe, which will be described more thoroughly in the Sec. 1.5.

1.3 The Dark Ages

To understand the formation of gravitationally bound structures, it is necessary to model and follow the evolution of the small inhomogeneities which appeared in the primordial Universe. The fate of the primordial fluctuations is described by the gravitational instability scenario that explains how regions that were denser than the average value, first on small spatial scales, and later on larger ones, collapsed due to their enhanced self-gravity. When the deviations from homogeneity are small, the dark matter can be treated as a pressureless fluid and it evolves by very simple equations, following the so-called *linear* regime. On the contrary, when the density is significantly higher than the background, the full Newtonian theory of gravity must be included in the so-called *non-linear* regime. Hereafter we provide a schematic introduction about these topics, for a complete review see [Barkana & Loeb \(2001\)](#).

1.3.1 Linear regime

Suppose to model the expanding Universe as a fluid with an average mass density $\bar{\rho}(t)$ and let consider a slightly overdense region with an initial density $\bar{\rho} + d\rho$. To obtain a rigorous model of the growth of perturbations we need a set of equations that gives the evolution of the density ρ of a fluid in a gravitational field with potential Φ . From classical fluid dynamics we know that, for a fluid with velocity \mathbf{v} , and pressure P , this set of equations holds:

$$\frac{D\rho}{Dt} + \rho \nabla_r \mathbf{v} = 0 \quad (\text{continuity}) \quad (1.7)$$

$$\frac{D\mathbf{v}}{Dt} = -\frac{\nabla_r P}{\rho} - \nabla_r \Phi \quad (\text{Euler}) \quad (1.8)$$

$$\nabla_r^2 \Phi = 4\pi G \rho \quad (\text{Poisson}) \quad (1.9)$$

where:

$$\frac{D}{Dt} \equiv \frac{\partial}{\partial t} + \mathbf{v} \nabla_r \quad (1.10)$$

is the material derivative, and $G = 6.67 \times 10^{-8} \text{ cm}^3 \text{ g}^{-1} \text{ s}^{-2}$ is the gravitational constant. Given the fact that we want to study the density fluctuations of the fluid in an expanding Universe, it is convenient to consider the comoving coordinates

replacing $\mathbf{r} = a(t)\mathbf{x}$ and:

$$\mathbf{v} = \dot{\mathbf{r}} = \dot{a}(t)\mathbf{x} + a(t)\dot{\mathbf{x}}. \quad (1.11)$$

In the previous relations \mathbf{x} is the comoving distance, and the parameter $a(t)$ is called scale factor and it represents the relative expansion of the Universe. It relates the proper distance between a pair of objects moving with the Hubble¹ flow in an expanding Universe at any arbitrary time t .

In these new coordinates, the density fluctuations can be expressed as $\rho(\mathbf{x}, t) = \bar{\rho}(t)[1 + \delta(\mathbf{x}, t)]$. If we neglect non-linear terms, we combine continuity and Euler equations, we suppose that pressure $P = \rho^\gamma$ is a function of density alone, and we consider the Fourier transform of the perturbation:

$$\delta(\mathbf{x}, t) = \int d^3\mathbf{k} \delta_k(t) \exp(i\mathbf{k} \cdot \mathbf{x}) \quad (1.12)$$

we obtain the evolution equation of the perturbation for each \mathbf{k} -mode:

$$\frac{d^2\delta_k}{dt^2} + 2\left(\frac{\dot{a}}{a}\right) \frac{d\delta_k}{dt} = \left[4\pi G\bar{\rho} - \frac{k^2 c_s^2}{a^2}\right] \delta_k \quad (1.13)$$

where $c_s^2 = (dP/d\rho)$ is the speed of sound. Eq. 1.13 tell us that the growth of the perturbations due to gravitational collapse is counteracted by both the pressure and the expansion of the Universe. To examine this equation we define the Jeans length as:

$$\lambda_J \equiv \frac{2\pi a}{k_J} = c_s \sqrt{\frac{\pi}{G\bar{\rho}}} \quad (1.14)$$

we have two possibilities:

1. if $\lambda < \lambda_J$ we have $\omega^2 = k^2 c_s^2 - 4\pi G\bar{\rho} = c_s^2(k^2 - k_J^2) > 0$ hence the solutions of the Eq. (1.13) – neglecting for now the expansion of the Universe and setting $2\left(\frac{\dot{a}}{a}\right) \frac{d\delta_k}{dt} = 0$ – are $\delta_k = \delta_0 e^{i(kr \pm \omega t)}$. In this situation the pressure is able to prevent the collapse and the density perturbation propagates as waves with the speed of sound. The perturbations do not grow.
2. if $\lambda > \lambda_J$ we have $\omega^2 = k^2 c_s^2 - 4\pi G\bar{\rho} = c_s^2(k^2 - k_J^2) < 0$ hence in this case the solution of Eq. (1.13) represents a non-propagating stationary wave with an

¹Edwin Hubble observed for the first time that external galaxies are receding at a speed (v) which is proportional to their distance from us (r): $v = H_0 r$. The constant of proportionality has been named Hubble constant H_0 . It is actually a function of the cosmic time: $H(t) \equiv \dot{a}(t)/a(t)$.

amplitude that increases with time exponentially.

The previous analysis shows that the Jeans length provides the minimum scale that is required for a non-relativistic fluid in the linear regime to collapse under its self-gravity. As a final remark, we note that the equations derived in the linear theory apply both to dark and baryonic matter, because in this regime the densities of baryons are low enough to assure that the complications of baryonic physics (such as the radiation transfer) can be neglected.

1.3.2 Non-linear regime

In order to have a complete picture of the structure formation process, we need to follow it into the non-linear regime, with analytic approximations or numerical simulations. We start by noticing that, unlike what found in the previous Section, the equations presented hereby to describe collapse of the highly overdense patches of the Universe are strictly applicable only to the dark matter. This is because in the non-linear regime, the density of the baryons reach values that make the radiative and thermodynamical processes impossible to be neglected.

The dynamical collapse of a dark matter halo can be solved analytically only in cases of particular symmetry. Let suppose that, at some time, there is a spherically symmetric density fluctuation in the expanding Universe, such that its associate over-density is δ_i . The structure collapse, supposing that the mass M_h inside the sphere is constant, is described by the Newtonian equation:

$$\frac{d^2r}{dt^2} = -\frac{GM_h}{r^2(t)} \quad (1.15)$$

where $r(t)$ is the time evolution of the radius of the material, The solution of the previous equation can be written parametrically as $r(t) = b(1 - \cos \eta)$, where:

$$t = \sqrt{\frac{b^3}{GM_h}}(\eta - \sin \eta) \quad (1.16)$$

The turnaround radius, $r_{TA} = 2b$, is defined as the radius at which the expansion stops and the collapse phase begins. It occurs when $\eta = \pi$. It is possible to demonstrate that the time between the initial fluctuation and the begin of the

collapse can be written as:

$$t_{TA} = \pi \sqrt{\frac{b^3}{GM_h}} \approx 1.095 \frac{t_i}{\delta_i^{3/2}} \quad (1.17)$$

hence the higher is the initial overdensity the sooner the collapse begins.

The model briefly discussed above is oversimplified because the density fluctuations are neither spherically symmetric nor isolated, and the collapsing material undergoes relaxation and eventually settles into an equilibrium configuration, called a halo. An accurate modeling of the non-linear regime collapse (see e.g. [Barkana & Loeb, 2001](#)) leads to the following analytic expressions for the virial radius, the circular velocity, and the virial temperature of the halo of mass M_h which collapses at redshift z :

$$r_{vir} = 0.784 \left(\frac{M_h}{10^8 h^{-1} M_\odot} \right)^{1/3} \left[\frac{\Omega_m \Delta_c}{18\pi^2 \Omega_m(z)} \right]^{-1/3} \left(\frac{1+z}{10} \right)^{-1} h^{-1} \text{ kpc} \quad (1.18)$$

$$v_h = 23.4 \left(\frac{M_h}{10^8 h^{-1} M_\odot} \right)^{1/3} \left[\frac{\Omega_m \Delta_c}{18\pi^2 \Omega_m(z)} \right]^{1/6} \left(\frac{1+z}{10} \right)^{1/2} \text{ km s}^{-1} \quad (1.19)$$

$$T_{vir} = 2 \times 10^4 \left(\frac{\mu}{0.6} \right) \left(\frac{M_h}{10^8 h^{-1} M_\odot} \right)^{2/3} \left[\frac{\Omega_m \Delta_c}{18\pi^2 \Omega_m(z)} \right]^{1/3} \left(\frac{1+z}{10} \right)^{-1} \text{ K} \quad (1.20)$$

where m_p is the proton mass, μ the mean molecular weight, and ([Norman et al., 1998](#)):

$$\Delta_c = 18\pi^2 + 82(\Omega_m(z) - 1) - 39(\Omega_m(z) - 1)^2 \quad (1.21)$$

is the final overdensity relative to the critical density at the collapse redshift. This method provides excellent predictions for the main physical quantities of the halo but it does not allow to determine the relative abundance of halos of a specific mass or size. To do that, it is necessary to describe the density field and its fluctuations on a given scale.

Firs of all, we introduce the concept of window function $W(\mathbf{r})$ normalized so that $\int d^3r W(\mathbf{r}) = 1$. By using this function we obtain the smoothed density perturbation field $\int d^3\delta(\mathbf{x}) W(\mathbf{r})$ on a particular scale. If we assume a spherical top-hat window function:

$$W_R(\mathbf{r}) = \begin{cases} 1 & \text{if } \mathbf{r} < R \\ 0 & \text{if } \mathbf{r} > R \end{cases} \quad (1.22)$$

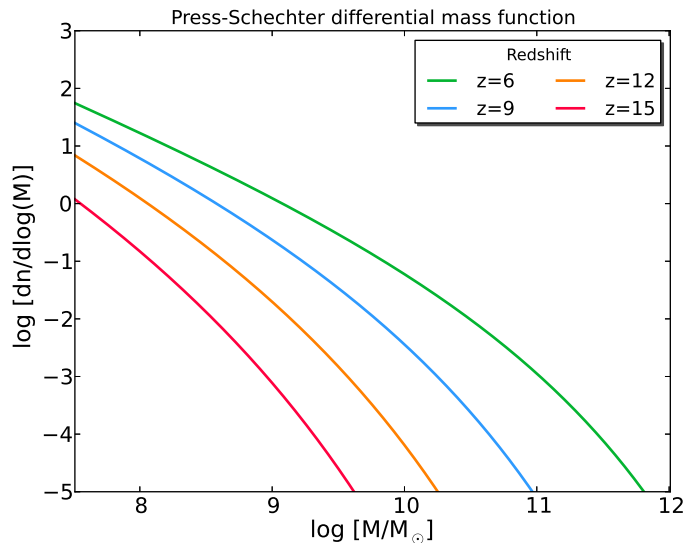


Figure 1.2: The Press-Schechter differential halo mass function at several redshifts: $z = 6$ (green curve), $z = 9$ (blue curve), $z = 12$ (orange curve), $z = 15$ (red curve).

we are able to follow the growth of perturbations on the scale R . In this case the smoothed perturbation field is denoted with δ_R or δ_M where $M = 4\pi\rho_m R^3/3$. The variance of $\langle\delta_M\rangle$ is:

$$\sigma^2(M) = \sigma^2(R) = \int_0^{\text{inf}} \frac{dk}{2\pi^2} k^2 P(k) |\widetilde{W}_R(k)|^2 \quad (1.23)$$

where $\widetilde{W}_R(k)$ is the Fourier transform of the real-space window function $W_R(\mathbf{r})$. The variance $\sigma(M)$ is a key parameter in order to achieve the abundance of dark matter halos of a given mass.

There are two main methods to evaluate this quantity: (a) numerical simulations that solve the equations of gravitational collapse, and (b) analytical techniques that approximate these results with simple one-dimensional functions. Clearly, only a numerical approach can give the spatial distribution of halos, however, analytical techniques are extremely useful because they allow the analysis of a wide range of parameters and they are much faster. The most commonly adopted analytic method was first developed by [Press & Schechter \(1974\)](#) (subsequently refined by [Sheth & Tormen, 1999](#)) and it is greatly successful in describing the formation of structures and in reproducing the numerical results. In [Press & Schechter \(1974\)](#) approach, the abundance of halos at a redshift z is determined from the linear density field by

applying a model of spherical collapse to associate peaks in the field with virialized objects in a full non-linear treatment. The method provides the comoving number density of halos, dn , with mass between M and $M + dM$ as:

$$M \frac{dn}{dM} = \left(\frac{2}{\pi}\right)^{1/2} \frac{-d(\ln\sigma)}{d(\ln M)} \frac{\rho_0}{\ln M} \nu_c e^{-\nu_c^2/2} \quad (1.24)$$

where ρ_0 is the present mean mass density, σ is the standard deviation of the density contrast smoothed through a certain window function $W(r)$ and ν_c is the minimum number of standard deviations of a collapsed fluctuation (see Fig. 1.2).

1.4 First stars

So far we briefly outlined the formation of dark matter halos during the *Dark Ages*, however the equations presented in the previous section (i.e. in the non-linear regime) are no longer valid for the baryons.

The gas collapsing into the dark matter potential wells drives the formation, at around $z \approx 20 - 30$, of the first generation (*PopIII*) of stars (see e.g. Ciardi & Ferrara, 2005; Bromm & Yoshida, 2011, for exhaustive reviews). The way in which the fragmentation happens and its relation with the thermodynamical conditions of the gas are still far to be completely understood, however some fundamental properties of the *PopIII* stars are already quite well established. First of all, *PopIII* stars are thought to be very different from local stars because they were very metal poor. Their metal abundance was comparable to that of the Universe immediately after the Big Bang, i.e. $Z_* \sim 10^{-10}$, while for comparison, a standard *PopII* star is nowadays characterized by $Z_* \approx 10^{-3} - 10^{-4}$. The *PopIII* stars were also characterized by (i) large masses, (ii) high surface temperatures. To understand why these stars were much more massive than the ones formed in the subsequent epochs let consider the relation between the Jeans mass (M_J) and the temperature of the gas. It is possible to demonstrate that $M_J \propto T^{3/2}$, therefore in the early (and hotter compared to present-day) Universe, the characteristic mass scale of a *PopIII* star is larger than that of a *PopII* ($M_{PopIII} \sim 10^2 - 10^3 M_\odot$). In addition, because of the lack of metals, the CNO cycle was not active, and this forced them to fragment in only relative large units. Effectively, only massive stars, that reach very high temperatures and densities, are able to produce enough energy by nuclear fusion through the $p - p$ chain to counterbalance the collapse due to their self-gravity.

In order to collapse, the gas needs to cool. The cooling happens mainly through the radiative de-excitation of H_2 hence, the fate of a virialized clump, conclusively depends on its ability to rapidly increase its molecular hydrogen content in timescales comparable to that of the collapse. The modeling of the formation of *PopIII* stars requires: (i) the understanding of the various channels available for the gas to cool, (ii) the evaluation of their efficiency and (iii) to take into account of feedbacks – like the shock heating of the collapsing gas – which set the scales of fragments.

These unusually massive stars burned their fuel in a short period of time since the stellar lifetime τ is inversely proportional to the cube of its mass: $\tau \propto M^{-3}$. They eventually exploded as supernovae and, if sufficiently large, collapsed into compact objects. The metals produced during their lifetime were then dispersed during the supernova explosion, enriching the surrounding gas.

Finally, we note that the amount of UV ionizing photons arising from *PopIII* stars, and the fraction which escapes from the star-forming sites are fundamental parameters that shape the evolution of the subsequent phase of the cosmic history: the Epoch of Reionization.

1.5 The Epoch of Reionization

The formation of the *PopIII* stars led to the emission of high-energy photons that progressively penetrated the surrounding intergalactic medium (IGM) at increasingly larger scales. For the second time in its history, the matter inside the Universe results ionized, hence the reionization marked the second phase transition for the cosmic gas (see e.g. Zaroubi, 2013, and references therein for an extensive review). The current constraints strongly suggest that the Epoch of Reionization occurs within the redshift range $z \sim 15 - 6$ (e.g. McGreer et al., 2014; Planck Collaboration et al., 2015).

The reionization process, according to the terminology introduced by Gnedin (2000), can be divided in three phases: (i) *pre-overlap* phase, during which several sources started to produce ionizing radiation, while the ionization fronts were still detached, (ii) *overlap* phase, throughout which individual [H II] regions overlapped, and (iii) *post-overlap* stage, that marks the period when the remaining high-density regions were gradually ionized.

A theoretical parametrization of the evolution of the reionization needs an accurate modeling of galaxy formation, and a proper treatment of the radiative transfer of ionizing photons. A fundamental parameter for the radiative transfer is the so called escape fraction (f_{esc}), namely the fraction of ionizing radiation that escapes the galaxy into the IGM. Theoretical and observational constraints on f_{esc} are either difficult to be achieved: on the theoretical side, the main issues reside in the modeling of the star formation process, and in the determination of the production rate of ionizing photons; on the observational side, the difficulties are especially due to the fact that high redshift sources are very faint. However, observational and theoretical approaches agree to bound the value of the escape fraction in the range $f_{esc} = 0.1 - 0.5$.

The main parameter used to describe the evolution of the cosmic reionization is the filling factor Q_{HII} , i.e. the fraction of the volume of the Universe which is filled by [H II] regions. If, on the one side, it is commonly accepted that the more the Universe is clumped, the longer is the time required for the reionization to be completed, on the other side, there is an open debate about the specific kind of sources, and their relative importance, that caused the reionization of the Universe. Five possible classes of sources have been identified: (1) *PopIII* stars, (2) galaxies, (3) quasars, (4) Gamma Ray Bursts and (5) decaying/annihilating dark matter particles.

1. *PopIII* stars are able to release large amount of ionizing photons because of the high temperatures reached in their inner parts. As pointed out before, much efforts have been made to model the formation of this first generation of stars. Currently, *PopIII* stars are thought to account for the leading contribution to the reionization.
2. To constrain the contribution of the first galaxies to the reionization is necessary to model their intrinsic [H I] ionizing photon rate as well as the escape fraction from their interstellar medium. To do that, a correct evaluation of the star formation rate and a detailed description the physical conditions of the ISM are either fundamental. Much work has been done on the theoretical side to model the escape fraction of high- z galaxies (e.g. Verhamme et al., 2008; Dayal & Ferrara, 2011; Ferrara & Loeb, 2013, just to mention fews), and a step forward is also provided with the work carried out in this Thesis even though focused on the emissivity of far-infrared lines. On the observational

side, a major contribution will be provided by the forthcoming James Webb Space Telescope (JWST) that will allow a sensitive search of the UV emission from galaxies at $z > 10$.

3. Quasars are very efficient sources of ionizing photons. Their spectrum is harder than that from stellar sources, their efficiency is greater than that of the stars and, for a given density distribution of the host galaxy, the escape fraction is larger than that achieved for photons emitted by stars. The farthest quasar discovered to date is at $z \approx 7.085$ (Mortlock et al., 2011), is well inside the reionization period.
4. Gamma Ray Bursts (GRBs) are amongst the most luminous electromagnetic events known in the Universe. They are flashes of gamma rays associated with extremely energetic explosions. They produce a flux that is comparable to that of a QSOs and therefore they outshine any other sources of radiation, such as the ubiquitous dwarf galaxies. Currently, the most distant GRB event observed is at $z \approx 8.2$ (Tanvir et al., 2009), again during the reionization process.
5. The photons produced by the decaying dark matter particles could in principle represent an additional contribution to the reionization. However, several theoretical works point out that their effect on this process is actually very small (e.g. Mapelli et al., 2006).

1.6 Observations at high redshift

1.6.1 Optical and near infrared imaging

In the last twenty years the number of high- z observations has known a vigorous growth thanks to the employ of increasingly sensitive telescopes and sophisticated selection techniques (for an exhaustive review on the topic see Dunlop, 2013).

Starting from the '90s of the XXth century, the Hubble Space Telescope (HST), the Very Large Telescope (VLT), the Keck and Subaru telescopes, the remarkable performance of the Spitzer and Herschel Space Telescopes, have opened a window to the deep Universe. Their high sensitivity make it possible the the use of observational strategies conceptually simple, but technologically demanding, that have

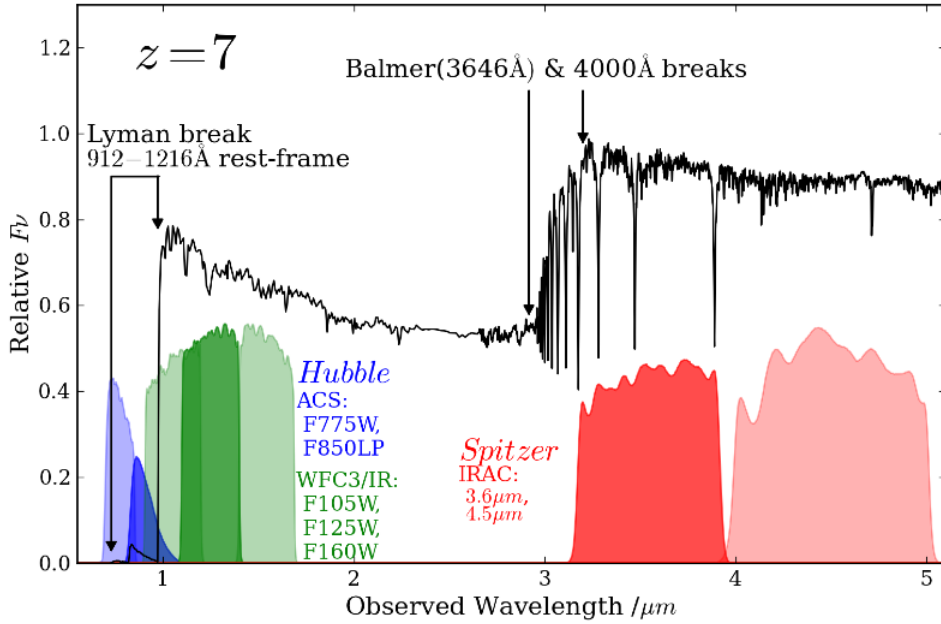


Figure 1.3: The redshifted form of the rest-frame UV SED from a young galaxy at $z \approx 7$, showing how the ultraviolet light is sampled by the red optical, and near infrared filters on-board of the Hubble Space Telescope (blue and green shaded regions). The longer-wavelength rest-frame optical light is probed by the IRAC channels on-board Spitzer (red shaded regions). Wavelength is plotted in the observed frame, while flux-density is shown per unit frequency f_ν and plotted as relative. The spectrum shows the sharp drop at $\lambda_{obs} \approx 1 \mu\text{m}$ (corresponding to $\lambda_{rest} = 1216 \text{ \AA}$) due to the strong Gunn-Peterson absorption by intervening neutral hydrogen. This drop is used to detect high- z galaxies with the Lyman Break selection technique. The SED presented in this figure does not include the Lyman- α emission line which is produced by excitation/ionization of hydrogen atoms in the inter-stellar medium of the galaxy; the Ly α offers the main current alternative route for the selection and spectroscopic confirmation of high-redshift galaxies. Figure from Dunlop (2013)

now been successfully applied to discover thousands of galaxies at $z > 5$. This is the reason why high redshift sources are often named according to the selection method adopted to detect them. In what follows, we present the main properties of the Lyman Break Galaxies (LBGs), and of the Lyman Alpha Emitters (LAEs) that are the two classes of objects considered in this Thesis.

Lyman Break Galaxies: the Lyman-break technique allows to identify galaxies by searching for the (redshifted) drop of the flux beyond the, so called, Lyman limit (912 \AA). Blueward of $\lambda = 912 \text{ \AA}$, the photoelectric absorption by intervening sources of neutral hydrogen sharply truncates the spectrum of the galaxies that, instead, is roughly flat up to this wavelength. At the highest redshifts, the increasing number of intervening neutral hydrogen clouds in the intergalactic medium produces

Lyman- α absorptions resulting in the so called Lyman- α forest. At $z > 6$ the forest becomes so optically thick that it kills virtually all of the galaxy light at $\lambda_{rest} < 1216 \text{ \AA}$, the so called "Gunn-Peterson effect", rendering the original 912 \AA break irrelevant. The Lyman-break selection in effect becomes the selection of objects with a sharp break at $\lambda_{rest} = 1216 \text{ \AA}$ (see Fig. 1.3).

For example, a LBGs at $z \sim 3$ shows the break shifted in the U band and the source become undetectable if observed with this filter. Galaxies at higher redshift drops out when observed in B-band ($z \sim 4$), V-band ($z \sim 5$) and even in the I-band ($z \sim 6$). LBG are young system with intense SFR, and the period of elevated star formation seems to coincide with a large dust opacity.

Lyman Alpha Emitters: Another selection method is the spectroscopic narrow-band search for sources with intense Lyman- α emission. The lines of the Lyman series are created when an electron falls from any higher energy level back to the ground state of the hydrogen atom. Ly α , the strongest line with a wavelength $\lambda = 1215.67 \text{ \AA}$, corresponds to transitions from the first excited level to the ground state. Generally LAEs are observed by using narrow band filters to select Ly α sources in different redshift ranges. After the narrow band selection, a spectroscopic follow-up is needed in order to confirm the redshift of the candidate. One of the upsides of the Ly α selection technique, is that the line has a characteristic asymmetric profile produced by neutral hydrogen absorption of the blue wing of the emission line (e.g. Hu et al., 2010). Moreover, the high sensitivity of narrow-band filters, make the LAE selection a method able to detect galaxies at $z \approx 7$ with a star formation rate comparable to that of the Milky Way. More precisely, modern narrow-band imaging searches are sensitive to Ly α rest-frame equivalent widths down to $EW \approx 15 \text{ \AA}$ and limiting line flux-densities that corresponds to a Lyman- α luminosity $L_\alpha \approx 2.5 \times 10^{42} \text{ erg s}^{-1}$ which, in the absence of obscuration, is equivalent to a star-formation rate $\text{SFR} \approx 2 M_\odot \text{ yr}^{-1}$ achieved with the Kennicutt (1998) relation in case B recombination theory. However, as well as for Lyman Break Galaxies, the term Lyman- α emitter represents a selection method rather than a physically distinct category of galaxies.

Several physical processes may cause the atom to emit Lyman- α photons. These processes can be divided into two classes: (i) recombinations following the ionization of the hydrogen or (ii) collisions with other atoms. Generally, the former channel is the dominant one, accounting for the major fraction of Ly α emission in galaxies.

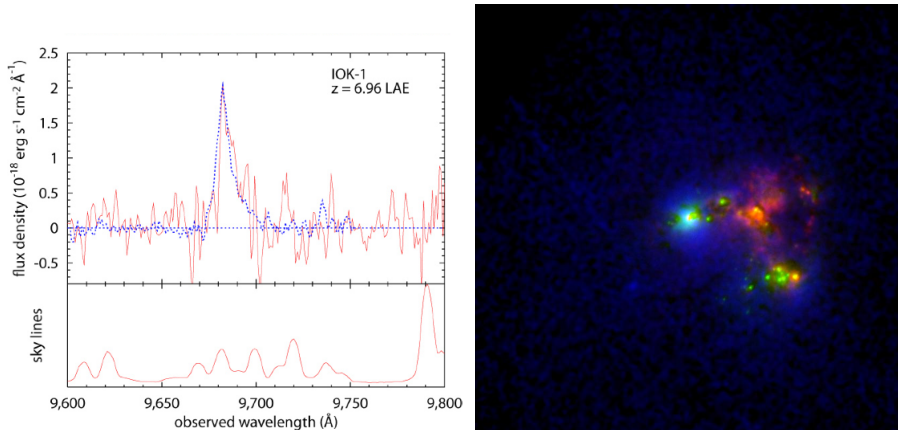


Figure 1.4: On the left hand side: the most distant spectroscopically-confirmed LAE selected via narrow-band imaging: IOK-1 (see Sec. 7.1 and 7.1.3 for further details and discussion about this galaxy). The spectrum clearly shows an asymmetric Lyman- α emission line at a wavelength corresponding to a redshift $z = 6.96$. Figure from Iye et al. (2006). On the right hand side: Haro11 (see also Sec. 4.4.2 for further details), a nearby star-forming galaxy observed as part of the HST Ly α imaging program LARS. The Lyman- α image is shown in blue, UV continuum in green, and H α tracing ionized gas in red. This figure reveals that a galaxy detected in Ly α is morphologically very different from its image in H α . This is due to the resonant scattering of the Lyman- α photons and it is at least qualitatively similar to what is found for high-redshift LAEs, in which the Lyman- α emission is in general more extended and diffuse than the UV continuum light. Credit: Hayes et al. (2009); Östlin et al. (2009)

As a matter of fact, star formation produces photons with energy larger than 13.6 eV that ionize the neutral hydrogen in the ISM. Due to the extremely high density of the ISM, the resulting electrons and protons recombine on short timescales and give rise to a Ly α line. However, as shown by Dayal et al. (2010) also the cooling of collisionally excited H I can contribute to the total emission.

Even though the Lyman Break and Ly α selection techniques have been proved to be very successful in finding high- z galaxies, there are several drawbacks that we must consider. On the technical side, the detections of LAEs via narrow-band imaging are increasingly difficult as we approach $z \approx 7$, due to the declining sensitivity of the detectors at $\approx 1 \mu\text{m}$ given the increasing brightness of night sky emission. Moreover, the higher is the redshift the larger is the neutral hydrogen fraction in the intergalactic medium, and hence the resonant scattering of the Ly α photons.

On the theoretical side, the characterization of fundamental galaxy properties (such as the star formation rate and the stellar mass) with the sole detection of the redshifted Ly α line and/or FUV continuum is extremely hard. First of all, because for any reasonable stellar initial mass function, the UV continuum in a galaxy is

always dominated by the light arising from a relatively small number of short-lived massive stars, and hence it depends critically only on the *recent* star-formation activity. Secondly, the UV continuum is strongly affected by dust extinction and without a proper correction it can provide only lower limits on the SFR (Kennicutt & Evans, 2012). Finally, any tentative imaging making use of the Ly α line is affected by resonant scattering of Ly α photons by the neutral hydrogen in the IGM, hence results in general more extended and diffuse emitting regions than the UV continuum light (see the right-hand side of Fig. 1.4) (Östlin et al., 2014; Hayes et al., 2014).

1.6.2 Submillimeter observations in the ALMA era

From the previous discussion it appears clear that the detection of other lines beside the Ly α will be fundamental to characterize the ISM properties of high- z galaxies, their star formation history, their current SFR, and their dust mass.

The far infrared (FIR) emission lines and the dust continuum emission are suitable tracers of all these quantities. From high- z , they are redshifted in the submillimeter/millimeter bands that are at present day covered by the Atacama Large Millimeter/submillimeter Array (ALMA), the most powerful (sub)millimeter interferometer on the Earth. ALMA, starting from its *early science* operations in 2011, has opened a new window to explore and understand the infancy of the Universe. Its giant array of 12 m antennas, with baselines up to 16 km, and the additional compact array of 7 m and 12 m antennas used to image large scale structures that are not well sampled by the long baseline array, are expected to detect and image redshifted FIR atomic/molecular line emission from faint normal galaxies at the end of the *Dark Ages* previously selected only through optical surveys (e.g. LBGs, LAEs).

The FIR atomic lines (mainly fine structure transition of C, N, O) trace the neutral/ionized gas and provide information about the thermodynamical and chemical properties of the gas. The strongest one is the $^2P_{3/2} \rightarrow ^2P_{1/2}$ transition of the ionized carbon ([C II]) at 158 μm (Stacey et al., 1991). [C II] is the dominant coolant of the interstellar medium arising from various environments such as the neutral diffuse gas in the ISM and the photodissociation regions. In addition, nitrogen and oxygen lines ([N II], [O I] and [O III]), despite their lower luminosity, are fundamen-

tal to constrain the metallicity and the strength of the radiation field within the galaxies. Moreover, FIR lines, being completely unaffected by the dust extinction or resonant scattering such as the Ly α , are superb redshift estimators.

The molecular (mainly CO rotational transitions) emission arises from the molecular clouds, the birthplaces of the stars. Hence CO lines are unique tracers of the gas fueling the star formation. ALMA band coverage not only allows to detect CO rotational transition from galaxies located at various redshifts across the Universe, but it also permits to reconstruct a significative part the so called CO Spectral Line Energy Distribution (CO SLED) of single objects at a given ($z > 4$) redshift (see Fig. 1.5). Examples of the science that can be carried out using these lines range from the understanding of the link between the star formation and the presence of molecular gas, to the study of inflow/outflow processes.

Before the ALMA advent, atomic/molecular lines and continuum from high- z have been studied using for instance the Plateau de Bure Interferometer in France or the CARMA observatory in the US. Despite the great capabilities of these interferometers, only extreme sources such as quasar hosts or submillimeter galaxies, characterized by star formation rates of the order of $\approx 1000 M_{\odot} \text{ yr}^{-1}$ have been detected at through cooling lines or continuum: (e.g. Maiolino et al., 2005; Cox et al., 2011; De Breuck et al., 2011; Gallerani et al., 2012; Venemans et al., 2012, CII detections), (e.g Ferkinhoff et al., 2011; Nagao et al., 2012; Decarli et al., 2012; Combes et al., 2012, NII detections) (e.g. Sturm et al., 2010, for OI detection in two lensed Ultra-Luminous Infrared Galaxies at $z=1.3$ and $z=2.3$).

As pointed out in the introduction of this section, ALMA is expected to greatly improve the sensitivity of its precursors and therefore it would in principle allow to observe FIR lines arising from normal galaxies within the Epoch of Reionization. However, after two ALMA observing Cycles (even if not with its full capabilities) only a handful of galaxies at $z \approx 4 - 5$ with modest star formation rates ($50 - 300 M_{\odot} \text{ yr}^{-1}$) have been detected in [C II] or in continuum (Carilli et al., 2013; Carniani et al., 2013; Williams et al., 2014; Riechers et al., 2014) and any normal galaxy at $z \approx 7$ (Ouchi et al., 2013; Ota et al., 2014; Schaerer et al., 2015).

What is the reason of these initial difficulties? Is it only a matter of technical capabilities of the interferometer, and hence we have to wait for the ALMA full array to be able carry out these observations? Or, instead, are we learning something about the internal properties of the first galaxies that emerged from the *Dark*

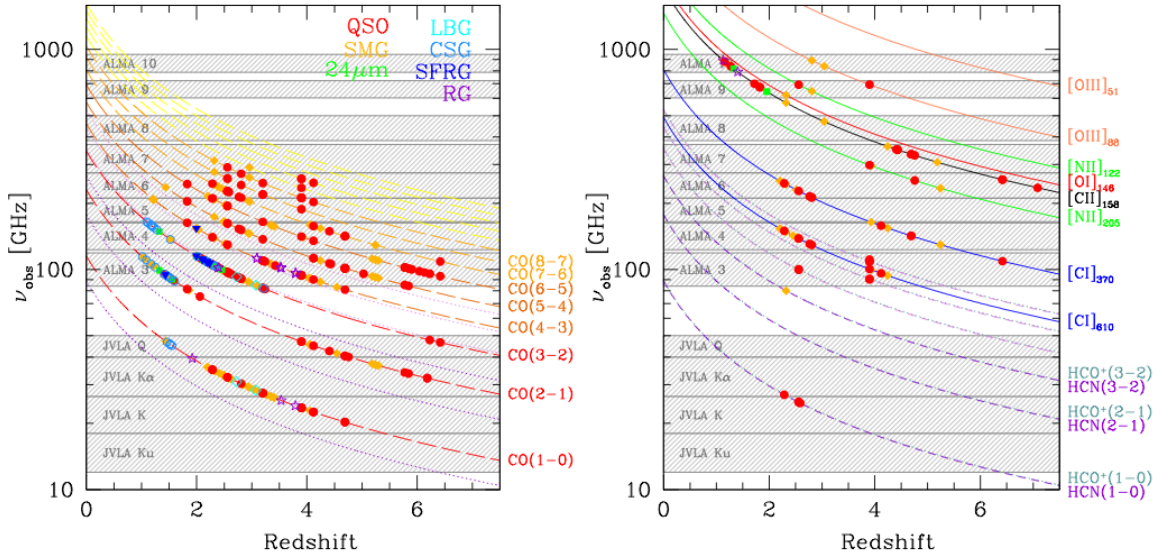


Figure 1.5: This plot shows the ALMA band coverage and the transitions that can be observed arising from various redshifts. Figure from: [Carilli & Walter \(2013\)](#)

Ages? Were the ISM physical properties of the first galaxies completely different with respect to those observed in the nearby Universe? Were the metallicity and dust mass so low that the effect on the visibility of the lines became substantial? Did the higher temperature of the CMB radiation affect the observed line fluxes as already discussed in a seminal paper by [da Cunha et al. \(2013\)](#)?

The model developed during this PhD Thesis provides answers to these questions.

Before entering in the details of the work we devote the next Chapter to the discussion of the physics behind the metal and molecular FIR line excitation and the emission of the dust continuum. We will show their undeniable potential in disentangling the properties of the interstellar medium.

The interstellar medium 2

UNDERSTANDING the physical processes that govern the behavior of the interstellar medium is central to much of modern astronomy and astrophysics. The ISM is a very complex environment composed by different structures that are the result of the continuous interplay between radiative and dynamical processes that take place on different scales. We cannot understand the large-scale dynamics of the ISM without profound knowledge of the underlying quantum physical and chemical processes. Vice versa, the dynamics on large galactic scales determine the local properties of the different phases of the ISM, such as their ability to cool and collapse, and to give birth to new stars. The interstellar medium is intrinsically linked to the life cycle of the stars being not only their birthplace, but also the environment into which they deposit energy, momentum and metals as they die.

This chapter aims at providing a general introduction about the current knowledge of the ISM physics that represents the theoretical background on which we constructed the models developed in this Thesis. In the first section we will address the description of the various phases of the ISM, in the second we discuss the physics of the interaction between radiation and matter and the various heating and cooling processes that determine the thermodynamic response of the various phases.

2.1 The phases of the interstellar medium

The thermal and chemical state of the ISM are conventionally described in terms of a number of distinct phases (neutral, ionized, and molecular) whose properties are summarized in Tab. 2.1 and discussed extensively in what follows.

Neutral gas

The fundamentals of the understanding of the physical properties of neutral gas in the ISM were established for the first time by [Field et al. \(1969\)](#). In their seminal paper the authors demonstrated that warm and cold neutral gas must coexist in pressure equilibrium to account for the [H I] 21-cm line observation either in absorption and in emission. Much of the [H I] mass is visible in absorption (and therefore cold) and concentrated in a small fraction of the volume, whereas much of the volume of the ISM is filled by neutral hydrogen visible only in emission (and therefore warm).

In the subsequent years the [Field et al. \(1969\)](#) work was improved by taking into account of the heating and the cooling mechanisms of the ISM that were not considered in the original paper (see e.g. [Wolfire et al., 1995, 2003](#))¹. However [Wolfire](#)

Component	Temperature (K)	density (cm ⁻³)	x_e
Molecular gas	10 – 20	> 100	10 ⁻⁶
Cold Neutral Medium (CNM)	50 – 100	20 – 50	10 ⁻⁴
Warm Neutral Medium (WNM)	6000 – 10 ⁴	0.2 – 0.5	0.1
Warm Ionized Medium (WIM)	8000	0.2 – 0.5	1.0
Hot Ionized Medium (HIM)	10 ⁶	10 ⁻²	1.0

Table 2.1: In this table are listed the typical temperatures, densities and ionized fractions of the various ISM phases. Adapted from the review by [Klessen & Glover \(2014\)](#).

[et al. \(1995\)](#) results do not alter the general conclusion that cold and warm interstellar [H I] may coexist in thermal pressure balance and, moreover, confirm that two-phase model is in good agreement with a wide variety of data on the ISM in the solar vicinity.

As pointed out before, the warm neutral medium (WNM) occupies a substantial fraction ($\sim 40\%$ e.g. [Carilli et al., 1998](#); [Heiles & Troland, 2003](#)) of the ISM volume, it has characteristic temperatures of $\sim 5000 - 10^4$ K and densities of $\sim 0.1 \text{ cm}^{-3}$ ([Wolfire et al., 2003](#)). On the other hand, the cold neutral medium (CNM) is distributed in sheets and filaments, it has a volume filling factor of $f_{\text{CNM}} \sim 0.01$, temperatures of $\sim 50 - 100$ K and densities of $\sim 20 - 50 \text{ cm}^{-3}$ ([Wolfire et al., 2003](#); [Klessen & Glover, 2014](#)). In the CNM the primary cooling mechanism is the radiative de-excitation of collisionally excited fine-structure lines of metals, while the WNM is the result of the onset of Ly α cooling at about 8000 K. Being the primary

¹A detailed description of the heating and cooling processes is presented in Sec. 2.5 and Sec. 2.6 respectively

cooling mechanism, the fine-structure lines of the metals are the main tracer of the neutral gas in the ISM.

Ionized gas

The two-phase model of the ISM proposed by [Field et al. \(1969\)](#) was extended by [McKee & Ostriker \(1977\)](#) who pointed out that blast waves racing outward from supernova explosions in the ISM would create large, collisionally ionized bubbles filled with very hot gas ($T \sim 10^6$ K) in pressure equilibrium with the neutral diffuse gas. Although this gas would eventually cool, the temperature dependence of the atomic cooling curve is such that the cooling time around $T \sim 10^6$ K is considerably long. Hence, rather than this hot gas having a wide range of temperatures, one would instead expect to find most of it close to that temperature. This hot, low density, ionized phase is known as the Hot Ionized medium (HIM) (or *coronal* gas) and is observed mainly through X-rays surveys.

There is also the evidence of another ionized phase in the ISM: the so called warm ionized medium (WIM). The WIM is maintained ionized by the radiation from recently formed hot massive O-type stars. These extended photo ionized regions are characterized by temperatures of $\sim 10^4$ K and densities $\sim 0.1 \text{ cm}^{-3}$, hence comparable to that of the WNM ([Draine, 2010](#)). Overall, $\approx 90\%$ of the total ionized gas within the galactic ISM is located in the WIM and it is mainly traced by optical emission lines produced by ionized species such as [O III] and [N II].

Molecular gas

The most abundant molecule in the Universe is by far the molecular hydrogen (H_2) which has an abundance that is orders of magnitude larger than that of any other. The direct detection of H_2 is very challenging due to its strongly forbidden rotational transitions. This is due to the homopolar nature of the molecule that has two distinct forms: (i) para-hydrogen with anti-parallel proton spins, and an even rotational quantum number J , and (ii) ortho-hydrogen with parallel proton spins, and odd rotational quantum number J . Radiative transitions between $J + 1 \rightarrow J$ states require a change in the nuclear spin, which is highly unlikely and results in small transition rates. The first accessible rotational transition is the $J = 2 \rightarrow J = 0$ that has an associated energy separation of ≈ 500 K attainable only under somewhat extreme conditions involving intense irradiation or shock waves ([Solomon & Vanden](#)

Bout, 2005). This is the reason why the H_2 cooling is effective only at relatively high temperature $T > 100\text{K}$ but becomes insignificant in comparison to fine structure line cooling or carbon monoxide (CO) rotational emission at $T < 100\text{K}$.

Actually, CO is the most widely used tracer to infer the presence of H_2 because it is a very stable molecule and the most abundant after H_2 , moreover it has a weak dipole moment and its rotational levels are easily excited by collisions with molecular hydrogen. CO cooling dominates once the gas density reach $n \approx 1000\text{ cm}^{-3}$, values typical of the internal cores of the Molecular Clouds (MCs).

2.2 Molecular clouds

The molecular cloud (MC) formation and their subsequent evolution are intrinsically linked with the physical properties of the surrounding ISM being the result of the complex interplay between the turbulence, the action of the magnetic field, and the effect of gravitation.

One of the simplest descriptions for molecular cloud formation is the coagulation model, (e.g. Tasker & Tan, 2009). This model is based on a picture of the ISM in which the cold atomic and molecular gas is organized into a series of discrete clouds that form directly from the WNM. The warm neutral gas breaks-up into dense clumps that efficiently dissipate energy and tend to coagulate forming successively larger clouds. Once the clouds have grown large enough, they become self-shielded from the external radiation field and hence dominated by molecular gas. The survival of H_2 molecules is guaranteed also by the presence of dust grains that further shield the molecular hydrogen and prevent its dissociation under the effect Lyman-Werner photons. The dust is the fundamental catalyst of the H_2 production (Gould et al., 1963; Hollenbach & Salpeter, 1971) providing the surface on which the hydrogen molecule forms. Hydrogen atoms have a non-zero probability to hit the surface of a dust grain present in the ISM, and they are able to diffuse some distance under the effect of the thermal vibration of the grain. However it may happen that they arrive in a site where the thermal energy is unable to free them for further exploration of the surface and, therefore, they become stuck to the grain. If eventually one of the newly arrived H atoms encounters a previously bound H, the two hydrogen atoms react to form H_2 . The energy released in the reaction that produces H_2 in the ground state is $\Delta E = 4.5\text{ eV}$, large enough to overcome the forces that were binding the two H atoms to the grain, hence the

H₂ molecule is ejected from the grain surface. Gas-phase reactions that lead to the formation of molecular hydrogen are instead very inefficient because the only allowed channels involve reaction with at least three species: $\text{H}^- + \text{H} \rightarrow \text{H}_2 + e^-$ (e.g. McDowell, 1961; Palla et al., 1983).

The mass and size of the molecular clouds range from small clumps with $M_{\text{C}} \sim M_{\odot}$ (or less) and $r_{\text{C}} < 10^{-2}$ pc, to large structures, called giant molecular clouds (GMCs), with $M_{\text{C}} \sim 10^3 - 10^6 M_{\odot}$ and $r_{\text{C}} \sim 10 - 30$ pc. Typical temperatures within MCs, inferred from the CO luminosity and theoretically reproduced through numerical simulations, ranges from $T \simeq 10$ K up to $T \simeq 50 - 60$ K typical of the CNM (see Tab. 2.1).

The density of the gas (ρ) inside molecular clouds is intrinsically related to the turbulence that develops within the gas. A fluid becomes turbulent when advection strongly dominates over dissipation, i.e. when the velocity increases so that the flow becomes unstable; this holds true in the ISM. Convergent flows lead to spatially and temporally confined regions of increased density and expansion creates lower-density voids. Consequently, the overall distribution of density in the ISM is a sensitive function of the statistical properties of the underlying turbulent flow, with key parameters being the Mach number \mathcal{M} , the magnetic field strength, and the thermodynamic properties of the gas. Analytical models as well as numerical simulations show that the distribution of the gas density in isothermal, non self-gravitating, turbulent media follows a log-normal probability distribution function (PDF) (Padoan & Nordlund, 2011):

$$\text{PDF}(s) = \frac{1}{\sqrt{2\pi\sigma_s^2}} \exp\left(-\frac{(s - s_0)^2}{2\sigma_s^2}\right) \quad (2.1)$$

where $s = \ln(\rho/\rho_0)$ and $\rho_0 = \langle \rho \rangle$, $s_0 = \langle s \rangle$. For a purely Gaussian distribution, the mean s_0 is related to the variance σ_s^2 of the logarithmic density s via the equation:

$$s_0 = \frac{1}{2}\sigma_s^2 \quad (2.2)$$

This results from the normalization and mass-conservation constraints of the PDF (Vazquez-Semadeni, 1994). In turn, we can relate σ_s^2 to the Mach number \mathcal{M} , to the forcing parameter b , and to the ratio of the thermal energy density to the magnetic

energy density ω :

$$\sigma_s^2 = \ln \left(1 + b^2 \mathcal{M}^2 \frac{\omega}{\omega + 1} \right) \quad (2.3)$$

The density PDF (Eq. 2.1) affects the mass spectrum of the clumps that, eventually, under the effect of gravitation, collapse and form stars. The star formation has a quenching effect on the subsequent life of the MC that results completely dissociated/ionized once the radiation from the stars becomes strong enough. We refer to [Hennebelle & Falgarone \(2012\)](#); [Klessen & Glover \(2014\)](#) for a full explanation of the star formation process that is beside the scope of this Thesis.

2.3 Photodissociation regions

The molecular clouds are, by definition, dominated by molecular gas, while the gas in the diffuse phases of the ISM is almost entirely atomic. Hence cloud formation must involve a chemical transition from a mainly atomic to a mainly molecular gas; the aforementioned transition, happens in the so called photodissociation Regions (PDRs).

PDRs are defined as regions where far-ultraviolet ($6 < h\nu < 13.6$ eV) photons from stellar sources control the gas heating and chemistry and they are, on the one side, bounded by an *ionization front*, on the other, by the surface, called *photodissociation front*, where the hydrogen is 50% atomic and 50% molecular (see Fig. 2.2).

Radiative transfer in the FUV is largely regulated by small dust grains, which dominate the opacity, and by the presence of molecules that absorb far-ultraviolet radiation in strong lines and dissociate. The latter effect is the so-called *self-shielding* and refers to the fact that in a region with a high H_2 column density ($N_{\text{H}_2} > 10^{14} \text{ cm}^{-2}$), the photons with energies corresponding to the main absorption lines of molecular hydrogen are absorbed in the outskirts of the PDR. To let emerge the importance of the dust in the FUV radiative transfer often the depth into the PDR is measured with the amount of visual extinction $A_V = A_\lambda(5500\text{\AA})$ of the incident radiation field caused by the dust column to this depth. For instance, $A_V = 1$ corresponds to a reduction by a factor of 2.5 in the incident visual flux and, because of the assumed constant ratio of gas to dust, corresponds to a hydrogen nucleus column density of about $2 \times 10^{21} \text{ cm}^{-2}$.

In general, the penetrating far-ultraviolet photons drive the chemistry through photoionization and photodissociation processes. The main chemical reactions that take place in the PDRs are: (a) the formation and the photodissociation of H_2 , (b) the formation and the photodissociation of CO , and (c) the photoionization of C in $[\text{C II}]$. In what follows we briefly discuss these three classes of processes. However, the chemical network within a photodissociation region is even more complex, involving reactions in which also the nitrogen, the sulfur and the silicon take part.

As pointed out in the previous Section the radiative association of two hydrogen atoms is inefficient and the main channel to form H_2 molecules involves reactions on dust grain surfaces. Given the uncertainties in interstellar dust properties, the more straightforward solution is to derive the rate coefficient semiempirically by comparison of PDR models with observations (e.g. [Jura, 1975](#)):

$$\mathcal{R} \approx 3 \times 10^{-17} n n_H \quad (2.4)$$

where n_H is the number density of atomic hydrogen and n is the total number density of gas particles. A more detailed modeling of the rate coefficient for H_2 formation on dust grains adopted in this Thesis is presented in Sec. 3.2.1. Photodissociation of H_2 occurs via a process that involves the absorption a UV photon with energy $E > 11.2 \text{ eV}$, placing it in an excited electronic state. If the electronically excited state fluoresces to the vibrational continuum of the ground electronic state (this happens with a probability of $\approx 15\%$ [Draine & Bertoldi, 1996](#)) the molecule dissociates. The photodissociation rate of H_2 per unit volume, $\mathcal{R}_{\text{diss}}$, is given by [Hollenbach & Tielens \(1999\)](#):

$$\mathcal{R}_{\text{diss}} = f_{\text{shield}}(N_{\text{H}_2})e^{-\tau}I_{\text{diss}}(0)n_{\text{H}_2} \quad (2.5)$$

where n_{H_2} is the H_2 number density, $I_{\text{diss}}(0)$ is the unshielded dissociation rate per H_2 , τ is the optical depth of the dust at 1000 \AA , N_{H_2} is the H_2 column density, and f_{shield} is the self shielding factor.

The $[\text{C II}]/\text{C}$ balance is generally dominated by the two simple photo-ionization and radiative recombination reactions: $\text{C}^+ + e^- \rightarrow \text{C} + \gamma$ and $\text{C} + \gamma \rightarrow \text{C}^+ + e^-$. Instead, the carbon monoxide forms via a complex chemical network that includes OH and OH^+ , or CH and CH_2 . The interested reader can find the complete

of the transition it is necessary to take into account of either the entire chemical network and the effect of the clumpyness of the gas on the efficiency of the chemical reactions. As a matter of fact, the clumpy nature of interstellar clouds can have a profound influence on the penetration of far-ultraviolet radiation creating large fluctuations in the mean intensity at a given depth (e.g. Spaans, 1996).

Then there are two main strategies to simplify the problem: a) shrinking the chemical model down to the essential (i.e. only to those reactions that affect abundances of H, H₂, C⁺, C and CO) while continuing to use a detailed description of the hydrodynamical evolution of the gas (e.g. Dobbs, 2008; Glover et al., 2010; Glover & Clark, 2012), or b) retaining the chemical complexity of the full network, choosing to simplify instead the geometry and the dynamical treatment of the gas. This is the strategy used, for example, in most PDR codes (e.g. Bell et al., 2005; Meijerink & Spaans, 2005; Röllig et al., 2007)

2.4 The dust

The presence of the dust, produced (i) during the AGB phase of low-mass stars and/or (ii) in expanding supernovae ejecta, was first recognized for its obscuring and reddening effects on the starlight in the Galactic ISM. The dust enters in a variety of fundamental processes in the interstellar medium such as the formation of molecules on the grain surface, the subtraction of selected elements from the gas phase which then coagulates to form the solid grains, or the photoelectrons emission from grain surface that dominates the heating of the gas in neutral regions.

The photons, passing through dusty regions are absorbed and scattered by the dust grains in a wavelength-selective way such that the bluer is the radiation the more the extinction is strong. To a first approximation, individual grains absorb only photons with wavelengths smaller than their physical size. Hence, the fact that the dust absorption has a peak in the ultraviolet provides hints about the dust grain size distribution. The first parametrization, valid over a range of radii from $r_{d,min} = 50$ nm to $r_{d,max} = 0.25$ μ m and in the local Universe, was proposed by Mathis et al. (1977) and refined by Draine & Lee (1984): $N(r)dr \propto r^{-3/5}dr$. In the high redshift Universe, when the low-mass stars have not yet evolved, grain condensation in supernova ejecta provides the only viable explanation for the existence of dust. This affects the previous equation, that results shifted towards smaller grains (Todini &

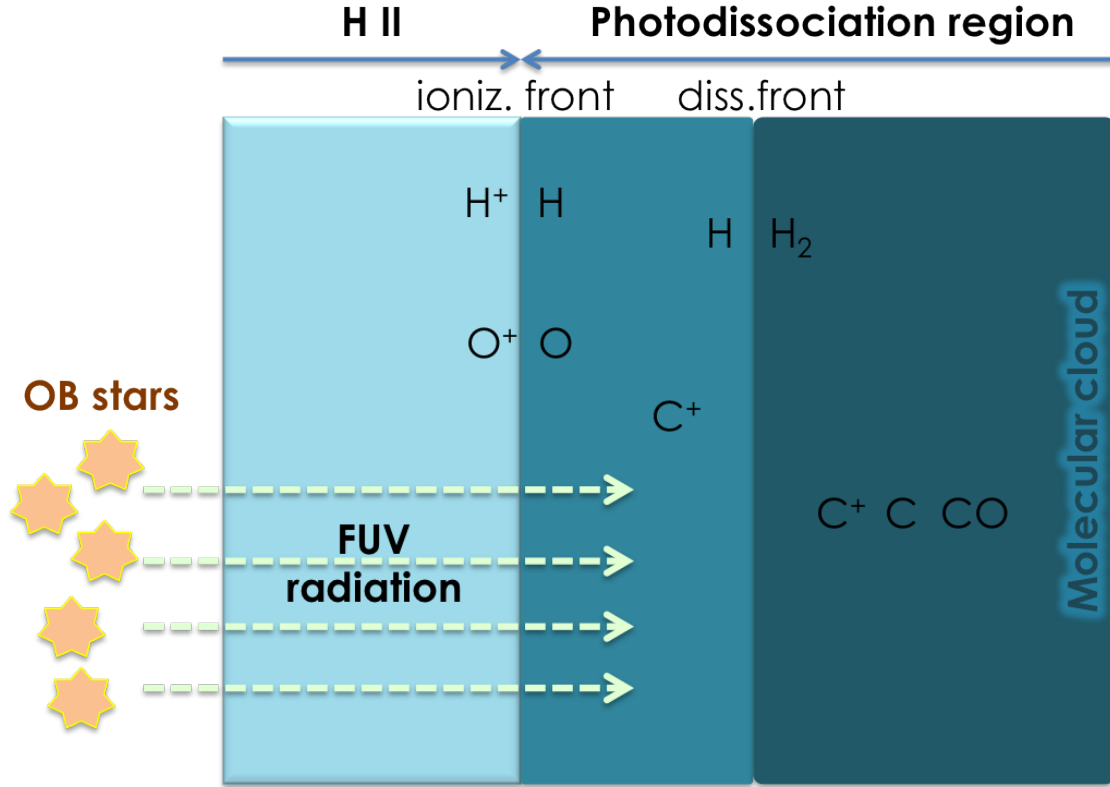


Figure 2.2: A schematic picture of the structure of a PDR. Starting from the left side we have the [H II] region produced by FUV ionizing photons arising from OB stars. The FUV photons penetrate and dissociate the molecules into H, C, and O atoms. This part of the cloud is also characterized by the presence of ionized carbon (C^+). This is due to the fact that C ionization energy is lower than that of hydrogen. The innermost region of the cloud remains fully molecular with predominantly H_2 and CO content.

Ferrara, 2001), and in general the shape of dust extinction curve $A(\lambda)$ (e.g. for the local Universe and at high- z respectively: Calzetti et al., 2000; Bianchi & Schneider, 2007). Detailed measurements of the spectral shape of $A(\lambda)$ give also information about the dust composition. For instance, the 217.5 nm bump is produced by carbonaceous grains, while the silicates produce features at $9.7 - 18 \mu\text{m}$.

The incident photons absorbed by the grains cause the heating of the dust which re-emits this energy as thermal continuum radiation in the FIR band, with a spectrum of a modified black-body:

$$J_\nu \propto B_\nu(T_d)(\nu/\nu_0)^\beta. \quad (2.6)$$

In the previous equation J_ν is the mean specific intensity of the radiation field, $B_\nu(T_d)$ is the Planck function, T_d is the mean temperature of the dust grains, and β is the spectral index that in the Milky Way is $\beta = 1.62$ (Planck Collaboration et al.,

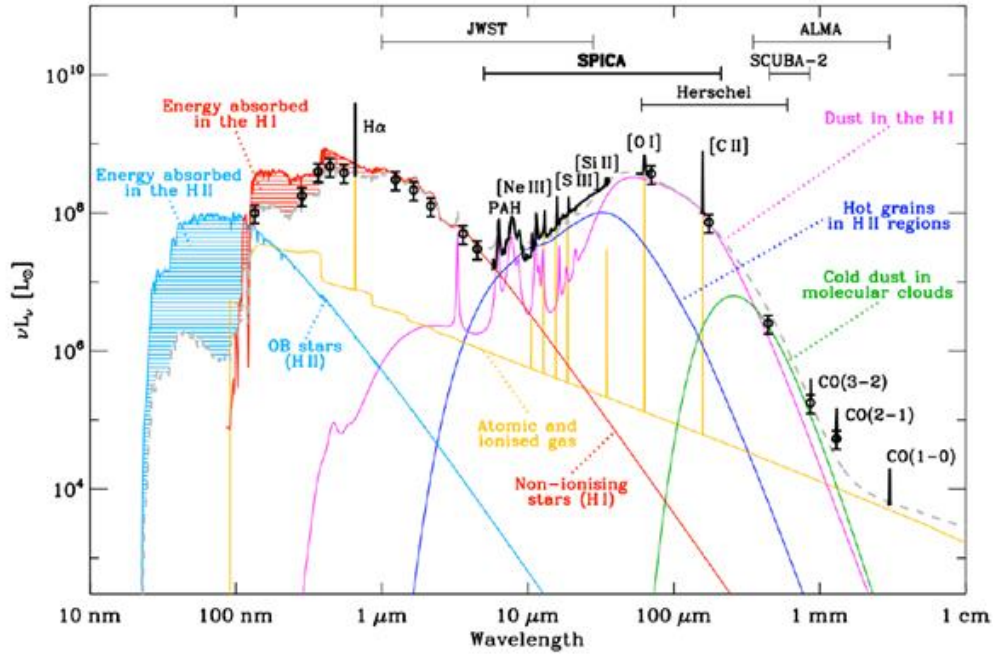


Figure 2.3: Synthetic spectral energy distribution of a galaxy, highlighting the contribution of the stellar sources, the dust emission and the gas lines. The observational windows available in past (Herschel), present (ALMA, SCUBA) or planned (JWST, SPICA) telescopes are plotted on top of the SED. The dust emission is shown in blue, purple, and green for decreasing T_d respectively. Hence the peaks of the emission shift toward longer wavelength. In light-blue is shown the emission from young stars, in red that arising from old stars, in yellow the fir line emission of atomic and ionized metals in the interstellar gas. Finally, the black points represent the rotational transition of CO molecules. Adapted from Galliano et al. (2008).

2014). As shown in Fig. 2.3, the peak of the emission depends on the temperature of the dust: the lower is the temperature the more the peak is shifted toward longer wavelengths. In the same figure are clearly shown several other distinct peaks at wavelengths $\lambda = 3.3, 6.2, 7.7, 8.6, 11.3$ and $12.7 \mu\text{m}$. These features correspond to vibrational emission bands produced by the polycyclic aromatic hydrocarbons (PAHs), large organic molecules, containing one or more aromatic rings.

2.5 Heating processes in the diffuse neutral gas

Generally speaking, the gas heating always happens through the transfer of kinetic energy to atoms, molecules and ions. In what follows we focus on the processes that take place in the neutral diffuse phase of the ISM. Each of the main heating channels that we are going to describe – (i) photo-electric ejection of electrons from dust grains (ii) cosmic-ray heating (ii) X-ray heating – begins with the extraction

of an electron from the atoms or from the dust grains, by an energetic particle or photon. Then, the supra thermal electrons produced in these different channels heat the gas through collisions.

2.5.1 Photoelectric heating

One of the most important mechanisms of radiative heating in the diffuse ISM is the photoelectric effect produced by the interaction between dust grains and UV photons. It happens when UV photons cause the detach of the electrons from the grain surface. The resulting free e^- has an energy $E_e = h\nu - W$, where W is the work necessary to extract the electrons from the grain (work function), and $h\nu$ is the energy of the photon. For instance, the work function for carbonaceous grains is $W \approx 5$ eV and hence $E_e \geq$ eV. This energy excess is rapidly redistributed among the other gas particles in the form of heat.

The dust grain size distribution is a critical parameter to calculate the heating resulting from the photoelectric effect. Smaller grains have a much larger photoelectric efficiency so that half of the contribution to the heating is due to grains with size $r_d < 15$ Å and to PAHs (Wolfire et al., 2003).

The fraction (ϵ) of FUV radiation absorbed by grains and converted to heating is (Bakes & Tielens, 1994; Wolfire et al., 1995):

$$\epsilon = \frac{0.049}{1 + 4 \times 10^{-3}(G_0 T^{1/2}/n_e)^{0.73}} + \frac{0.037(T/10^4)^{0.7}}{1 + 2.0 \times 10^{-4}(G_0 T^{1/2}/n_e)} \quad (2.7)$$

where n_e is the free electron number density, and G_0 is the FUV flux scaled to the Habing (1968) value ($= 1.6 \times 10^{-3}$ ergs cm^{-2} s^{-1}). In practice Eq. 2.7 tell us that the dependence of the photoelectric heating rate on the physical conditions in the gas is function of a single parameter $x \equiv G_0 T^{1/2}/n_e$ proportional to the rate of ionization divided by the rate of recombination. At small values of x grains are mainly neutral (or negatively charged) and the efficiency is at maximum ($\epsilon = 0.05 - 0.09$), at higher values of x the efficiency drops due to the positive charging of the grains. The resulting heating rate per unit volume is (Wolfire et al., 1995):

$$n_H \Gamma_{pe} = 1.3 \times 10^{-24} n_H \epsilon G_0 \text{ erg cm}^{-3} \text{ s}^{-1} \quad (2.8)$$

where n_H is the hydrogen nuclei density.

2.5.2 Cosmic ray heating

Cosmic rays are very energetic charged particles (mostly being nuclei $\approx 99\%$ with a small fraction of electrons $\approx 1\%$) originated in various processes such as supernovae explosions, stellar winds, and active galactic nuclei accretion. Their energy spans a wide range, from 100 MeV up to more than 1 TeV and their energy density in the ISM is approximately 2 eV cm^{-3} , within a factor of a few of the mean thermal energy density.

Cosmic rays play an important role in the energy balance of the ISM when the gas is well shielded from the interstellar radiation field, so that the photoelectric heating become unimportant. In this regime, cosmic rays are the main sources of heat through the following process:

1. A cosmic ray hits an atom of the interstellar gas and ionizes it (*primary ionization*), resulting in an ejection of an energetic ($\langle E \rangle \sim 35 \text{ eV}$) *secondary electron*.
- 2a. The secondary electron loses its energy by ionizing (*secondary ionization*) or exciting other atoms.
- 2b. When the energy of e^- is $\leq 10 \text{ eV}$, the electron dissipates it through elastic collisions with other e^- , resulting in heating the gas.

The contribution of the secondary ionization to the heating depends on the amount of free electrons in the gas: when the electron fraction is $> 10^{-3}$ there are so many electrons around that $e^- - e^-$ collisions dominate and secondary ionization is suppressed. In this situation the primary electron has a high probability of losing its energy by Coulomb scattering and $\sim 100\%$ of the initial kinetic energy is converted to heat. On the other hand, secondary ionization can contribute as much as 80% in regions where the electron fraction is small.

Wolfire et al. (1995) parametrize the energy density per unit time gained by the gas through ionizations produced by cosmic rays with this expression:

$$n_H \Gamma_{CR} = n \zeta_{CR} E_h(E, x_e) \text{ erg cm}^{-3} \text{ s}^{-1} \quad (2.9)$$

where n_H is the hydrogen density, $\zeta_{CR} \sim 1.8 \times 10^{-17} \text{ s}^{-1}$ (Wolfire et al., 1995) is the primary ionization rate, and $E_h(E, x_e)$ is the energy deposited by each primary e^- of energy E (see Appendix A of Shull & van Steenberg, 1985).

2.5.3 X-ray heating

X-rays, emitted by compact objects or by the hot interstellar plasma, contribute to the gas heating through a mechanism that is similar to the one described in the previous section for the cosmic rays. The absorption of soft X-rays in the ISM causes the production of very energetic photoelectrons that heat the gas, mainly by ionizing H and He atoms. The helium plays an important role in this circumstance because the cross-section for absorption of X-rays by He atoms is substantially larger than for H atoms. The *primary* ionization rate of species i due to soft X-rays is given by:

$$n_H \zeta_{XR}^i = 4\pi n \int \frac{J_\nu}{h\nu} \exp(-\sigma_\nu N_W) \sigma_\nu^i d\nu \quad (2.10)$$

where J_ν is the X-ray spectrum, and the exponential factor in previous equation accounts for an absorbing layer of gas of column density N_W . Unlike cosmic rays, X-rays are more sensitive to the effects of absorption, since their mean free paths are typically much smaller. Therefore, although X-ray heating can be important in the diffuse ISM, it is generally not efficient in the dense gas inside molecular clouds, unless these clouds are located close to a strong X-ray source such as an Active Galactic Nucleus (AGN).

The total energy density per unit time released by the X-ray heating is (Wolfire et al., 1995):

$$n_H \Gamma_{XR} = 4\pi n \sum_i \int \frac{J_\nu}{h\nu} \exp(-\sigma_\nu N_W) \sigma_\nu^i E_h(E^i, x_e) d\nu \text{ erg cm}^{-3} \text{ s}^{-1} \quad (2.11)$$

where the sum extends over species which suffer primary ionization.

2.6 Cooling processes in the diffuse neutral gas

The cooling of the gas in the interstellar medium happens through processes that convert kinetic energy into radiation which escapes from the gas. This is possible if the photons emitted are not re-absorbed, i.e. if the gas is optically thin to the radiation. The main cooling channels are:

1. Radiative cooling through: (a) collisional excitation of fine structure lines of metals, and (b) hydrogen and helium excitation, ionization and recombination.

2. Electronic recombination on dust grains.

2.6.1 Radiative cooling

As a starting point to explain how radiative cooling operates in the ISM let consider a two-level atom with an energy difference between the upper (u) and lower (l) level $\Delta E_{ul}/k_B = (E_u - E_l)/k_B = T_*$. The transition $l \rightarrow u$ can be excited by collisions with electrons, protons (but also other species such as He atoms, or molecules) and by radiative excitation due to an external radiation field with intensity I_ν . The downwards transition is instead produced by stimulate and spontaneous emission, and by collisional de-excitation. The ratio of the level population can be found by solving the statistical balance equation:

$$\frac{n_u}{n_l} = \frac{B_{lu}I_\nu + \sum_i n_i C_{lu}^i}{B_{ul}I_\nu + A_{ul} + \sum_i n_i C_{ul}^i} \quad (2.12)$$

where C_{lu}^i (C_{ul}^i) are the collisional excitation and de-excitation rates (in $\text{cm}^3 \text{s}^{-1}$) for collisions with the i -th species, A_{ul} is the Einstein coefficient of spontaneous emission, B_{ul} and B_{lu} are the stimulated emission and absorption coefficients, and n_i is the number density of the colliding atoms/electrons/molecules.

From requiring that the level population follows the Boltzmann distribution, and denoting with T_k the kinetic temperature of the gas, the following relations must hold:

$$\begin{aligned} C_{lu}^i(T_k) &= \frac{g_u}{g_l} e^{-T_*/T_k} C_{ul}^i(T_k), \\ g_l &= g_u \frac{B_{ul}}{B_{lu}}, \\ A_{ul} &= \frac{2h\nu^3}{c^2} B_{ul}. \end{aligned} \quad (2.13)$$

The first equation states that in local thermal equilibrium (LTE), the rate at which collisions cause transitions from level l to level u must be the same as the rate at which they cause transitions from level u to level l . A simplification that we can often make in the ISM is to ignore the effects of the incident radiation field in Eq. 2.12 which then becomes:

$$\frac{n_u}{n_l} = \frac{\sum_i n_i C_{lu}^i}{A_{ul} + \sum_i n_i C_{ul}^i} \quad (2.14)$$

This is justified if the gas is optically thin and the strength of the interstellar radi-

ation field at the frequency ν_{ul} is small. Before going ahead, we note that a critical density exists such that the collisional de-excitation and spontaneous emission rates are equal:

$$n_{crit}^i \equiv A_{ul}/C_{ul}^i. \quad (2.15)$$

For densities $n_i \gg n_{crit}^i$ the radiative emission rate will be strongly reduced as de-excitation predominantly proceeds through collisions and hence the process do not result in a photon emission. On the contrary, if the density n_i is much lower than the critical density, from Eq. 2.14, where for simplicity we consider only the collisions with a single i species, we have:

$$n_u \simeq \frac{n_i C_{lu}^i}{A_{ul}} n_l \quad (2.16)$$

and hence the emissivity $\varepsilon \equiv A_{ul} n_u$ becomes:

$$\varepsilon \simeq n_i n_l C_{lu}^i(T_k) \simeq n_i n C_{lu}^i(T_k). \quad (2.17)$$

In the previous equation $n = n_l + n_u$ is the total density of the atoms that we are considering in our toy-model. The radiative cooling rate Λ_{ul}^i of our collection of atoms for collisions with the i species, i.e. the emissivity multiplied by the energy of the photons, becomes:

$$\Lambda_{ul}^i(T_k) = n_i n \Delta E_{ul} C_{lu}^i(T_k) \quad (2.18)$$

where $\Delta E_{ul} C_{lu}^i(T_k) \equiv L^i(T)$ is the so called cooling efficiency (Dalgarno & McCray, 1972). In the high-density case, in which $A_{ul} \ll n_i C_{ul}^i$, we have instead:

$$n_u \simeq \frac{C_{lu}^i}{C_{ul}^i} n_l = \frac{g_u}{g_l} e^{-T_*/T_k} n_l \quad (2.19)$$

and therefore:

$$\varepsilon \simeq A_{ul} n_l \frac{g_u}{g_l} e^{-T_*/T_k} = A_{ul} n \frac{(g_u/g_l) e^{-T_*/T_k}}{1 + (g_u/g_l) e^{-T_*/T_k}} \quad (2.20)$$

that results in a cooling rate:

$$\Lambda_{ul}^i(T_k) = n A_{ul} \frac{(g_u/g_l) e^{-T_*/T_k}}{1 + (g_u/g_l) e^{-T_*/T_k}} \Delta E_{ul}. \quad (2.21)$$

Transition		
Initial state	Final state	L_e^m [erg cm ³ s ⁻¹]
C ⁺ (² P _{1/2})	C ⁺ (² P _{3/2})	$7.9 \times 10^{-20} T^{-1/2} \exp(-92/T)$
Si ⁺ (² P _{1/2})	Si ⁺ (² P _{3/2})	$7.9 \times 1.9^{-18} T^{-1/2} \exp(-413/T)$
Fe ⁺ (⁶ D _{9/2})	Fe ⁺ (⁶ D _{7/2})	$1.1 \times 10^{-18} T^{-1/2} [\exp(-554/T) + 1.3 \exp(-961/T)]$
Fe ⁺ (⁶ D _{9/2})	Fe ⁺ (⁶ D _{5/2})	
O(³ P ₂)	O(³ P _{1,0})	$1.74 \times 10^{-24} T^{1/2} [(1 - 7.6 T^{-0.5}) \exp(-228/T) + 0.38 (1 - 7.7 T^{-0.5}) \exp(-326/T)]$

Table 2.2: Cooling efficiency for the most important metal fine-structure lines due to electron collisions (Dalgarno & McCray, 1972).

From Eq.s 2.18 and 2.21 we note that while in the sub-critical regime $\Lambda_{ul}^i \propto n^2$ in the supra-critical $\Lambda_{ul}^i \propto n$.

Metal cooling: Having briefly outlined the basic physical principles of the radiative cooling, we now examine which of the many possible forms of line emission are the most important for the cooling of interstellar gas. In this section we focus our attention on the fine-structure transitions of metal species such as the carbon (C), the oxygen (O), the iron (Fe) and the silicon (Si), both neutral and ionized. These lines are excited by collisions with electrons and neutral hydrogen atoms and are effective coolants at moderate densities e.g. in the WNM and CNM. This is due to the fact that the critical densities associated with these fine structure transitions are relatively high: $n_{crit} \geq 10^2 - 10^6$ when we consider collisions with H, and up to two to three orders of magnitude smaller when collisions with electrons dominate (Hollenbach & McKee, 1989, see Tab. 8 in). The cooling function (see also Eq. 2.18) due to collisional excitation of metals (\mathcal{M}_i) depends directly on the fractional ionization (x_e) and on the temperature of the gas. It can be written as the sum of the contribute due to electron collisions (Λ_m^e) and to neutral hydrogen collisions (Λ_m^H):

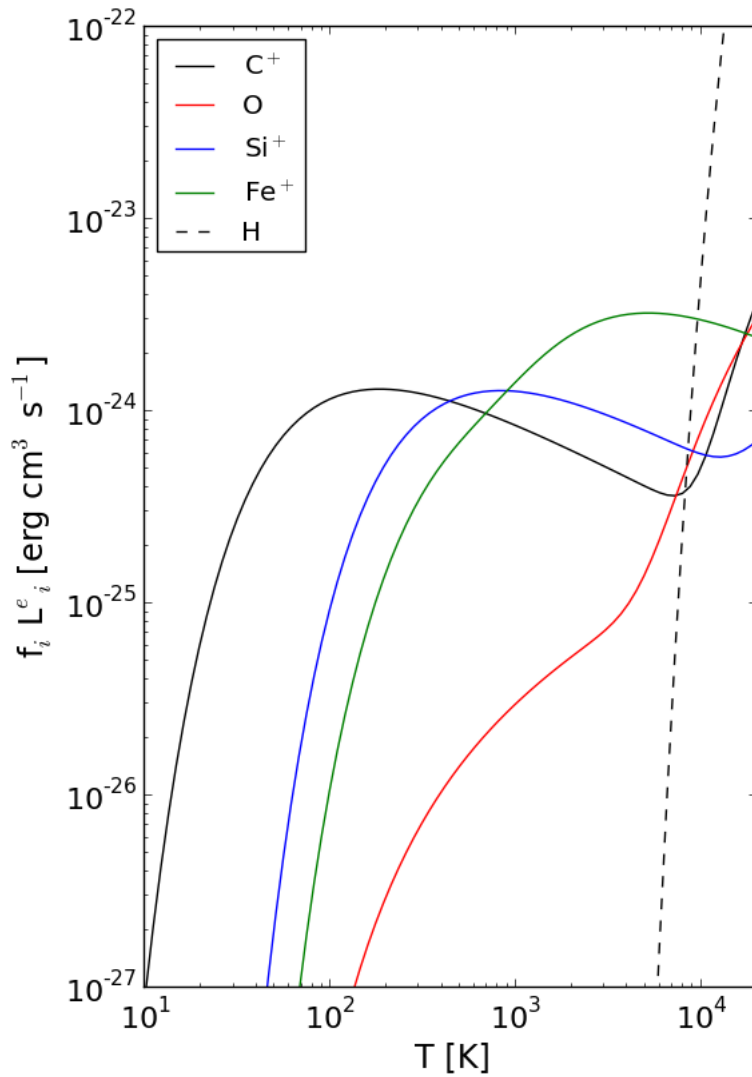
$$\Lambda(x_e, T)_{metals} = \sum_m (\Lambda_m^e + \Lambda_m^H) \quad (2.22)$$

The expressions of the cooling efficiency $L_m^H(T)$ and $L_m^e(T)$ for different metal lines can be found Tab 2.3 and Tab.2.2.

In Fig. 2.4 is shown the contribution to the cooling of the main metal lines as a function of temperature, for a given ionized fraction x_e . Fine structure transition $^2P_{3/2} \rightarrow ^2P_{3/2}$ of ionized carbon [C II] at $\lambda = 158 \mu\text{m}$ is the most important and

Element/Ion	L_H^m [erg cm ³ s ⁻¹]
C ⁺	tabulated in Dalgarno & McCray (1972)
Si ⁺	$7.4 \times 10^{-23} \exp(-413/T)$
Fe ⁺	$1.1 \times 10^{-22} [\exp(-554/T) + 1.4 \exp(-961/T)]$
O	tabulated in Dalgarno & McCray (1972)

Table 2.3: Cooling efficiency for the most important metal fine-structure lines due to H collisions.

Figure 2.4: The individual contributions to the interstellar cooling by electron impact excitation as a function of temperature T . In the plot $f_i = n_i/n_H$ where n_i is the number density of the i -th species.

can be excited by collisions with electrons, H, He and H₂ molecules. Much of the work of this thesis is devoted to the study of the luminosity of this line in the high- z galaxies.

H and He cooling: At high temperatures, in regions dominated by atomic or ionized gas, the cooling of the ISM takes place largely via the permitted (i.e. dipole-allowed) electronic transitions (ionization, excitation, and recombination) of various atoms and ions, mainly hydrogen and helium. Each recombination causes an energy loss equal to the mean kinetic energy of the couple ion-electron that recombines, while a collisional ionization remove from the gas an amount of energy equal to ionization potential of the ionized species. At temperatures close to 10⁴ K, excitation of the Lyman series lines of atomic hydrogen is the dominant process, giving rise to a cooling rate per unit volume (Black, 1981):

$$\Lambda_{H,ion}^e = 7.5 \times 10^{-19} \exp(-118348/T) n_e n_H \text{ erg cm}^{-3} \text{ s}^{-1} \quad (2.23)$$

The cooling due to the collisional ionization of H is parametrized as follows (Black, 1981):

$$\Lambda_{H,coll}^e = 1.27 \times 10^{-21} T^{1/2} \exp(-157809.1/T) n_e n_H \text{ erg cm}^{-3} \text{ s}^{-1} \quad (2.24)$$

and, finally, the cooling due to hydrogen recombination (Black, 1981):

$$\Lambda_{H,rec}^e = 2.85 \times 10^{-27} T^{1/2} (5.914 - 0.5 \ln T + 0.01184 T^{1/3}) n_e n_{\text{HII}} \text{ erg cm}^{-3} \text{ s}^{-1} \quad (2.25)$$

In Fig. 2.4 we show the contribution of metals and hydrogen to the interstellar cooling. At low temperatures the excitation of fine structure of ionized carbon dominates. When the temperature increases above ~ 600 K, Si⁺ and Fe⁺ channels become important up to $T \sim 10^4$ K, above which the contribution of H to the cooling begins to dominate.

2.6.2 Recombination on dust grains

Dust is not only responsible of the heating but it may act also as a sink for the gas energy. When the thermal energy of electrons that recombines on positively charged grains exceeds that of electron ejected from the grain surface there is a net cooling

Process	Notes
Photoelectric heating from small grains	$n_H \Gamma_{pe} = 1.3 \times 10^{-24} n_H \epsilon G_0$
Ionization and heating by cosmic rays	$n_H \Gamma_{CR} = n_H \zeta_{CR} E_h(E, x_e)$
Primary and secondary ionization	$n_H \Gamma_{XR} = 4\pi n_H \sum_i \int \frac{J_\nu}{h\nu} e^{(-\sigma_\nu N_W)} \sigma_\nu^i E_h(E^i, x_e) d\nu$
Ionization and heating by X-rays	
Cooling by fine-structure lines	
C II	impact with e^- and H
O I	impact with e^- and H
C I Si I Si II S I Fe I Fe II	minor coolant
Cooling by resonance lines	
Ly α	important at $T > 8000$ K
Cooling by metastable lines	
C I C II O I O II Si I Si II S I S II Fe I	O I most important coolant
Recombination onto small grains	$n_H^2 \Lambda_{gr} = 4.65 \times 10^{-30} T^{0.94} (G_0 T^{1/2} / n_e)^\beta n_e n_H$

Table 2.4: In this table we summarize the main heating and cooling mechanisms discussed in this Chapter.

in the gas. As for expression of the Γ_{pe} (see Eq. 2.8), the cooling rate due to the electron recombination on the dust grains (Λ_{gr}) is proportional to $x \equiv G_0 T^{1/2} / n_e$:

$$n_H^2 \Lambda_{gr} = 4.65 \times 10^{-30} T^{0.94} (G_0 T^{1/2} / n_e)^\beta n_e n_H \text{ erg cm}^{-3} \text{ s}^{-1} \quad (2.26)$$

where $\beta = 0.74 / T^{0.068}$ (Bakes & Tielens, 1994; Wolfire et al., 2003). The larger is x the higher is the cooling rate due to the increased positive charge of the grains, thus this cooling mechanism becomes important at high temperatures ($T > 10^4$ K) and FUV fluxes.

To provide the reader a summary of the discussion presented through this Chapter we list in Tab. 2.4 the cooling and heating mechanism in action in the diffuse gas in the ISM.

Molecular hydrogen in LAEs 3

IN THE PAST ten years we have witnessed a rapid increase in the amount of the available data on the high redshift galaxies. As discussed in Sec. 1.6, this has been made possible by a combination of state of the art instruments such as the HST, the Subaru and Keck telescopes, and sophisticated selection methods. Of the latter, one of the most successful approaches has been the use of the narrow-band technique (e.g. Malhotra et al., 2005; Shimasaku et al., 2006; Kashikawa et al., 2006; Hu et al., 2010) that is based on looking for the Ly α emission at 1216 Å in the galaxy rest frame. Hundreds of such LAEs have now been confirmed at $z \approx 2.25$ (Nilsson et al., 2009), $z \approx 3$ (Cowie & Hu, 1998; Steidel et al., 2000; Matsuda et al., 2005; Venemans et al., 2007; Ouchi et al., 2008), $z \approx 4.5$ (Finkelstein et al., 2007), $z \approx 5.7$ (Malhotra et al., 2005; Shimasaku et al., 2006) $z \approx 6.6$ (Taniguchi et al., 2005; Kashikawa et al., 2011) and $z \approx 7$ (Iye et al., 2006). Due to their large number statistics and unambiguous spectral signatures, LAEs are arguably the best probes of reionization and high-redshift galaxy evolution (Santos et al., 2004; Dijkstra et al., 2007; Kobayashi et al., 2007, 2010; Dayal et al., 2008, 2009, 2010; Dayal & Ferrara, 2011).

However, using LAEs as probes of high-redshift galaxy populations, understanding them to study reionization, and calculating their contribution to reionization, requires a correct estimate of their SFR. Translating the observed UV luminosity (1375 Å in the galaxy rest frame) into an intrinsic SFR is rendered hard by the fact that the UV continuum photons produced mainly by OB-stars are attenuated by the dust in the galactic interstellar medium. Inferring the intrinsic SFR using the observed Ly α luminosity is even more complicated since Ly α photons are absorbed/scattered either by the neutral hydrogen in the IGM along the line of sight

between the emitter and the observer, as well as by the dust in the ISM. A number of studies point to LAEs being dust enriched, even at redshifts $z \approx 6$: using theoretical models, [Dayal et al. \(2010\)](#) have shown that at $z \approx 5.7$, the color excess of LAEs, $E(B - V) \sim 0.15$ while observationally, the color excess values range between $E(B - V) \approx 0.025 - 0.32$ at $z \approx 4 - 5.7$ ([Lai et al., 2007](#); [Pirzkal et al., 2007](#); [Finkelstein et al., 2009](#)).

Further, the observed Ly α luminosity depends both on the reionization state of the IGM, as well as on the IGM peculiar velocities along the line of sight; inflows/outflows into/from a galaxy can blueshift/redshift the Ly α line, thereby decreasing/increasing the IGM Ly α transmission, T_α ([Verhamme et al., 2006](#); [Dayal et al., 2011](#); [Dijkstra et al., 2011](#)). However, the extent to which peculiar velocities influence T_α is debatable since these calculations have mostly been performed under idealized situations. For example, [Verhamme et al. \(2006\)](#) have used spherically symmetric outflows of H I to show an enhancement in T_α ; however, many studies, e.g. [Fangano et al. \(2007\)](#) and references therein, have shown that Kelvin-Helmholtz instabilities would result in breaking-up such symmetric outflows.

In this sense, H $_2$ is a far better indicator of the SFR since stars form in dense, cold MCs; theoretical and observational constraints on the molecular fraction are then of utmost importance to shed light on the abundance of the gas that fuels star formation, and therefore on the intrinsic SFR of these high redshift galaxies. The H $_2$ content of galaxies is generally studied through observations of CO rotational emission lines ([Solomon & Vanden Bout, 2005](#); [Omont, 2007](#)) that have been detected in more than a hundred high-redshift sources, even though searches for molecular gas at redshifts $z > 4$ have so far focused mainly on quasars and on the most massive, far-infrared-luminous and submillimeter galaxies (see [Riechers, 2011](#)). As of now, only scant effort has been devoted to observing the molecular content of high-redshift ($z \geq 6$) LAEs. In one of the few observational works present in literature, [Wagg et al. \(2009\)](#) have searched for low-J rotational CO emission lines in two LAEs at $z > 6.5$; the non-detection of any CO emission from these galaxies can then be used to put constraints on the amount of molecular gas in these sources.

Our aim in this Chapter is to present the self-consistent and physically motivated model built up during this Thesis to calculate the H $_2$ fraction and mass, in galaxies identified as LAEs at $z \approx 5.7, 6.6$. To do so, we start by using a previously

developed LAE sample (see Dayal et al., 2008, 2009, 2010; Dayal & Ferrara, 2011), where the authors combined state of the art cosmological SPH simulations with a Ly α production/ transmission model to successfully reproduce a large number of observational data sets. We couple the sample resulting from their analysis, with a semi-analytic model that describes the structure of the MCs. The approach, proposed by Krumholz et al. (2008, 2009) and McKee & Krumholz (2010) and already mentioned in Sec. 2.3, allows calculate the molecular hydrogen content taking into account its formation on dust grains, its destruction by UV photons, and the shielding by [H I] in the ISM starting from few inputs. Once the molecular fraction is estimated for all of the LAEs in our sample, we examine its correlations with the physical properties of the emitters, including the SFR, the dust mass, and the amount of cold [H I] gas in the ISM. Translating the total H₂ mass into a CO luminosity, we test the predictions provided by our theoretical approach with the observations carried out by Wagg et al. (2009). Finally, we estimate the expected observing time with ALMA that has band coverage and sensitivities suitable for CO line detection from high redshift (see Fig. 1.5).

3.1 The cosmological simulations

In this Section, we briefly describe the simulation used in the work, and interested readers are referred to Tornatore et al. (2010) for a complete description. The simulation has been obtained using the TreePM-SPH code GADGET-2 (Springel, 2005) with the implementation of chemodynamics as described in Tornatore et al. (2007). The adopted cosmological model corresponds to a Λ CDM Universe with $\Omega_m = 0.26$, $\Omega_\Lambda = 0.74$, $\Omega_b = 0.0413$, $n_s = 0.95$, $H_0 = 73 \text{ km s}^{-1} \text{ Mpc}^{-1}$ and $\sigma_8 = 0.8$, thus consistent with the 5-year analysis of the WMAP data (Komatsu et al., 2009). The simulation has a periodic box size of $75h^{-1}$ comoving Mpc (cMpc) and contains 512^3 dark matter particles, and initially the same number of baryonic particles. The run assumes a uniform redshift-dependent UV background produced by quasars and galaxies, as given by Haardt & Madau (1996) and includes metallicity-dependent radiative cooling (Sutherland & Dopita, 1993). The code has an effective model to describe star formation from a multi-phase ISM and a prescription for galactic winds triggered by supernova explosions (Springel & Hernquist, 2003); the initial mass function (IMF) is taken to be Salpeter between $1 - 100 M_\odot$. Metals and energy are released by stars of different masses by properly accounting for mass-

dependent lifetimes as proposed by Padovani & Matteucci (1993). The code uses the metallicity-dependent yields from Woosley & Weaver (1995); the yields for SNIa and asymptotic giant branch (AGB) stars have been taken from van den Hoek & Groenewegen (1997).

Galaxies are identified as gravitationally bound groups of star particles by running a friends-of-friends (FOF) algorithm. Each FOF group is then decomposed into a set of disjoint substructures, which are identified as locally overdense regions in the density field of the background main halo by the SUBFIND algorithm (Springel et al., 2001). After performing a gravitational unbinding procedure, only sub-halos with at least 20 bound particles are considered to be genuine structures (Saro et al., 2006). For each galaxy in each of the snapshots of interest ($z \approx 5.7, 6.6$), we obtain the total halo/gas/stellar mass ($M_h/M_g/M_*$), the SFR (\dot{M}_*), the mass weighted gas/stellar metallicity (Z_g/Z_*), the mass weighted age (t_*), the mass weighted gas temperature and the half mass radius of the dark matter halo.

3.1.1 Identifying LAEs

The simulated properties of each galaxy at $z \approx 5.7, 6.6$ are used to calculate the total intrinsic Ly α (L_α^{int}) and continuum luminosity (L_c^{int}) which include both the contribution from stellar sources and from the cooling of collisionally excited H in the ISM as shown in Dayal et al. (2010). To calculate the stellar contribution, we obtain the spectrum of each LAE using the population synthesis code STARBURST99 (Leitherer et al., 1999), using the simulated values of t_* , M_* , \dot{M}_* ; the cooling radiation depends on the temperature of the ISM gas. The intrinsic Ly α luminosity can be translated into the observed luminosity such that $L_\alpha = L_\alpha^{int} f_\alpha T_\alpha$, while the observed continuum luminosity, L_c is expressed as $L_c = L_c^{int} f_c$. Here, f_α (f_c) are the fractions of Ly α (continuum) photons escaping the galaxy, undamped by the ISM dust and T_α is the fraction of the Ly α luminosity that is transmitted through the IGM, undamped by neutral hydrogen.

The main features of the model used to calculate f_c , f_α and T_α are: (a) for each galaxy the dust enrichment is derived by using its intrinsic properties (\dot{M}_* , t_* , M_g) and assuming Type II supernovae (SNII) to be the primary dust factories. The dust mass, M_d , is calculated including dust production due to SNII, assuming an average dust mass produced per SNII of $0.5 M_\odot$ (Todini & Ferrara, 2001; Nozawa et al., 2003, 2007; Bianchi & Schneider, 2007), dust destruction with an efficiency of about

40% in the region shocked to speeds $\geq 100 \text{ km s}^{-1}$ by SNII shocks, assimilation of a homogeneous mixture of dust and gas into subsequent SF (astration), and ejection of a homogeneous mixture of gas and dust from the galaxy due to SNII, (b) the dust distribution radius, r_d , is taken to scale with the effective stellar distribution scale, r_e , such that $r_d \approx (0.6, 1.0)r_e$ at $z \approx (5.7, 6.6)$ respectively; the calculation of r_e is described later in Sec. 3.2.1, (c) f_c is calculated assuming a slab-like dust distribution and we use $f_\alpha = (1.5, 0.6)f_c$, as inferred for LAEs at $z \approx (5.7, 6.6)$, and (d) T_α is calculated using the mean photoionization rate predicted by the Early Reionization Model (ERM, reionization ends at $z \approx 7$) as proposed by [Gallerani et al. \(2008\)](#), according to which the neutral hydrogen fraction $\chi_{HI} = (6.0 \times 10^{-5}, 2.3 \times 10^{-4})$ at $z \approx (5.7, 6.6)$.

Once the above calculations have been carried out, following the current observational criterion, galaxies with $L_\alpha \geq 10^{42.2} \text{ erg s}^{-1}$ and an observed Ly α equivalent width $EW = L_\alpha/L_c \geq 20 \text{ \AA}$ are identified as LAEs. Complete details of these calculations can be found in [Dayal et al. \(2010\)](#) and [Dayal & Ferrara \(2011\)](#).

3.2 Molecular hydrogen physics

As pointed out in Sec. 2.2, H₂ can be formed in galaxies by two main channels: the first, and rather inefficient, method involves gas-phase reactions mainly through the coupled reactions $e^- + \text{H} \rightarrow \text{H}^- + h\nu$ and $\text{H}^- + \text{H} \rightarrow \text{H}_2 + e^-$ ([McDowell, 1961](#); [Palla et al., 1983](#)). The second, more efficient channel is through bond formation on dust grains: this process begins with the collision and absorption of at least two hydrogen atoms by the same dust grain. The hydrogen atoms are weakly bound to the grain surface through Van der Waals forces and can migrate on the grain either by tunnelling or thermal hopping. If the hydrogen atoms encounter each other, bond formation takes place, the excess energy is released to the grain, and the H₂ molecule is ejected into the gas phase ([Gould et al., 1963](#)). However, H₂ molecules so produced can be dissociated by the far ultraviolet (FUV) interstellar radiation field in the Lyman-Werner (LW) band between 11.2-13.6 eV; the twin processes of self shielding and dust absorption (e.g. [Hollenbach & Tielens 1999](#)) drive the shielding of H₂ to FUV photons, thereby preventing photodissociation.

We estimate the H₂ mass of each LAE at $z \approx (5.7, 6.6)$ using the analytic model presented in [Krumholz et al. \(2008, 2009\)](#) and [McKee & Krumholz \(2010\)](#), hereafter referred to as the KMT model. In brief, the KMT model considers an idealized

spherical cloud immersed in a uniform, isotropic LW radiation field. Then, the equations of radiative transfer coupled to the H_2 formation-dissociation balance are solved, assuming the cloud to be in the steady state.

The analytical solution to the H_2 mass fraction, $f_{\text{H}_2} = M_{\text{H}_2}/M_{\text{HI}}$, is then obtained by solving for the radial position at which the transition between the atomic envelope and the molecular interior occurs within the cloud; in this equation M_{H_2} and M_{HI} refer to the mass of molecular hydrogen and the mass of neutral hydrogen respectively. The KMT study shows that the fraction of the radius at which this transition occurs is solely a function of the dust optical depth in the LW band and the dimensionless parameter χ , which are discussed in what follows.

3.2.1 Modelling molecular hydrogen in LAEs

We now describe the model used to calculate the H_2 content of the LAEs identified in the simulation snapshots at $z \approx 5.7, 6.6$. We start by assuming that the MCs lie in a region that extends from the centre of the galaxy up to the effective stellar distribution radius, r_e , calculated in [Dayal et al. \(2010\)](#). This assumption has been motivated by the fact that star formation occurs in MCs; the physical distribution scale of MCs and the stars is therefore expected to be quite similar. Further, the value of r_e is based on estimates following the results of [Bolton et al. \(2008\)](#), who have derived fitting formulae relating the V-band luminosity and the stellar distribution scale from their observations of massive, early type galaxies between $z = 0.06 - 0.36$. Though not an entirely robust estimate, we extend this result to galaxies at $z \approx 5.7$ and 6.6 due to the paucity of observational data regarding the stellar distribution scales in high-redshift galaxies. However, such estimates are in surprisingly good agreement with recent observational results: [Malhotra et al. \(2011\)](#) find that the half-light radius of LAEs has a mean value ≈ 0.16 arcsec at $z \approx 5.7$ and this remains constant for all redshifts in the range $2 \leq z \leq 6.5$; these estimates lie within 1σ of the mean value of the theoretical r_e estimates used throughout this paper.

As mentioned above, using the KMT model, the H_2 mass fraction solely depends on the dust optical depth in the LW band, τ_c , and the dimensionless parameter χ , such that the analytical solution for the H_2 fraction can be written as ([McKee & Krumholz, 2010](#)):

$$f_{\text{H}_2} \simeq 1 - \left(\frac{3}{4}\right) \frac{s}{1 + 0.25s}, \quad (3.1)$$

where the dimensionless parameter s can be expressed as

$$s = \frac{\ln(1 + 0.6\chi + 0.01\chi^2)}{0.6\tau_c}. \quad (3.2)$$

Here,

$$\chi = \frac{f_{diss} E_0 \sigma_d c}{n_{\text{CNM}} \mathcal{R}}, \quad (3.3)$$

where, $f_{diss} \simeq 0.1$ (Draine & Bertoldi, 1996) is the fraction of absorbed LW band photons that lead to dissociation of the H_2 molecules, E_0 is the free space photon number density in the LW band, σ_d is the dust absorption cross-section per hydrogen nucleus to LW photons, c is the speed of light, n_{CNM} is the number density of gas in the cold atomic medium that surrounds the molecular part of the cloud, and \mathcal{R} is the coefficient for the rate of H_2 formation on the surface of dust grains.

It must be noted that these equations apply only for $s < 2$; for values of $s \geq 2$, the gas is predominantly atomic, such that $f_{\text{H}_2} = 0$. Also, we note that the calculations presented here concern only average quantities in a spherically symmetric framework; a full calculation of the radial dependence of the model parameters is the subject of ongoing work. We now explain the calculations of E_0 , σ_d , n_{CNM} , \mathcal{R} and τ_c in what follows.

LW photon number density

As mentioned in Sec. 3.1.1, we obtain the intrinsic spectrum of each LAE using the population synthesis code `STARBURST99`. Then, assuming all the stars to form at the centre of the galaxy, the number density of LW photons of a specific wavelength λ ($912 \text{ \AA} \leq \lambda \leq 1120 \text{ \AA}$), at a distance r from the centre can be expressed as

$$n_\lambda(r) = \frac{L_\lambda}{4\pi cr^2} \left(\frac{\lambda}{hc} \right). \quad (3.4)$$

Here, L_λ is the monochromatic luminosity at the wavelength λ obtained using `STARBURST99` and h is the Planck constant. The free space photon number density at radius r , in the entire LW band, n_{LW} , can then be calculated by integrating over all the wavelengths in the band such that

$$n_{\text{LW}}(r) = \frac{1}{4\pi r^2 c} \int_{912\text{\AA}}^{1120\text{\AA}} \frac{\lambda L_\lambda}{hc} d\lambda. \quad (3.5)$$

$M_h (M_\odot)$	f_4
$< 10^{10}$	0.58
$10^{10-10.4}$	0.40
$10^{10.4-10.8}$	0.35
$10^{10.8-11.2}$	0.35
$> 10^{11.2}$	0.35

Table 3.1: As a function of the halo mass range (col. 1), we show the fraction of ISM gas with temperature $T \leq 10^4$ K (col. 2).

The value of n_{LW} averaged over a sphere of radius r_e then gives the photon number density in the LW band such that

$$E_0 \equiv \langle n_{LW} \rangle = 3n_{LW}(r_e) \quad (3.6)$$

Cold neutral medium density

As extensively discussed in Sec. 2.1, much of the neutral gas in galaxies is observed to be cold, with temperatures of order of ~ 100 K, or warm, with temperatures of order of $\sim 10^4$ K, in approximate pressure balance (Wolfire et al., 2003) and MCs form in regions where the gas is primarily cold. To calculate the density of the cold neutral medium, we start by obtaining the fraction, f_4 , of ISM gas with temperature $T \leq 10^4$ K (see also Fig. 1, Dayal et al., 2010); the value of f_4 averaged over galaxies of different halo masses is shown in Tab. 3.1. However, the large volume simulated ($\approx 10^6$ cMpc³), naturally results in a low mass resolution, such that we are unable to resolve the cold and warm gas phases inside the ISM of individual galaxies. We therefore make the approximation that the ISM of each simulated galaxy has an equal amount of cold and warm neutral gas. The mass of the cold neutral gas, M_{CNM} , in any galaxy can then be calculated as

$$M_{\text{CNM}} = \frac{1}{2}f_4M_{\text{H}}, \quad (3.7)$$

where $M_{\text{H}} = 0.76 M_{\text{gas}}$ is the mass of hydrogen in the ISM. We assume the gas to be distributed in a disk with a radius r_g and scale height H such that (Ferrara et al., 2000)

$$r_g = 4.5\lambda r_{200}, \quad (3.8)$$

$$\frac{H}{r_g} = 15.3\lambda \left(\frac{c_s}{v_e}\right)^2 \quad (3.9)$$

Here, value of the spin parameter is taken to be $\lambda = 0.04$ (Ferrara et al., 2000) and the virial radius, r_{200} , is calculated assuming the collapsed region has an overdensity of 200 times the critical density (see Eq. 1.1) at the redshift considered. Assuming that the typical velocity that determines the scale height of the disk is that of WNM, the effective gas sound speed is taken to be $c_s = 10 \text{ km s}^{-1}$. Finally, the halo escape velocity, v_e , is related to the circular velocity of the halo, v_c , by the relation $v_e = 2pv_c$ with $p = 1.65$ (Mac Low & Ferrara, 1999). The average global number density of the CNM, n_{CNM} can then be expressed as

$$n_{\text{CNM}} = \frac{M_{\text{CNM}}}{\pi r_g^2 H m_H}, \quad (3.10)$$

where m_H is the hydrogen mass.

Molecular hydrogen formation rate

The rate of H_2 formation on dust grains, \mathcal{R} , can be expressed as (Hirashita & Ferrara, 2005)

$$\begin{aligned} \mathcal{R} &= 4.1 \times 10^{-17} S \left(\frac{r_d}{0.1 \mu\text{m}}\right)^{-1} \left(\frac{\mathcal{D}}{10^{-2}}\right) \\ &\times \left(\frac{T}{100 \text{ K}}\right)^{1/2} \left(\frac{\delta}{2 \text{ g cm}^{-3}}\right)^{-1} \text{ cm}^3 \text{ s}^{-1}, \end{aligned} \quad (3.11)$$

where $S = S(T, T_d)$ is the sticking coefficient for hydrogen atoms on dust grains, T is the gas temperature, δ is the density of the dust grains, \mathcal{D} is the dust-to-gas ratio, and r_d is the radius of the dust grain which is assumed to be a sphere. Following the assumptions of Dayal et al. (2010), we assume all the dust grains to be carbonaceous such that $\delta = 2 \text{ g cm}^{-3}$; using the size distribution of SNII-produced dust grains (Todini & Ferrara, 2001), we use an average grain size value of $r_d = 300 \text{ \AA}$. As mentioned before, dust predominantly forms in high-density, cold MCs which have a more effective self-shielding to LW photons compared to the

lower density WMN; following this argument, we use $T = 100$ K.

Further, the sticking coefficient $S(T, T_d)$ is given by [Hollenbach & McKee \(1979\)](#) and [Omukai \(2000\)](#) as

$$S(T, T_d) = [1 + 0.04(T + T_d)^{0.5} + 2 \times 10^{-3}T + 8 \times 10^{-6}T^2]^{-1} \times \{1 + \exp[7.5 \times 10^2(1/75 - 1/T_d)]\}^{-1}, \quad (3.12)$$

where T_d is the dust temperature. However, the sticking coefficient is not affected by the exact dust temperature as long as $T_d \leq 70$ K, which is true for all LAEs, which have dust temperatures $T_d \approx 30 - 45$ K.

Dust cross-section and optical depth

We now discuss the calculation of the dust cross-section per hydrogen atom to LW photons, which can be expressed as

$$\sigma_d = \frac{Q_{abs}(r_d)\pi r_d^2}{N_H}, \quad (3.13)$$

where $r_d = 300 \text{ \AA}$ is the average radius of SNII produced dust grains as mentioned above, $Q_{abs}(r_d)$ is the effective cross-section normalized to the geometric one for the average grain size and a wavelength of 1000 \AA corresponding to the centre of the LW band ([Draine & Lee, 1984](#)) and N_H is the number of hydrogen nuclei per dust grain. To calculate N_H , we use the dust to gas ratio, \mathcal{D} such that

$$\mathcal{D} = \frac{M_{dust}}{M_{gas}} \simeq \frac{\frac{4}{3}\pi r_d^3 \delta N_{dust}}{\mu m_p N_H} \quad (3.14)$$

where $\mu = 0.59$ is the mean molecular weight of a fully ionized gas of primordial composition. Substituting N_H from Eq. 3.13 into Eq. 3.14 yields

$$\sigma_d = \frac{3 \mu m_p \mathcal{D} Q_{abs}(r_d)}{4 \delta r_d}. \quad (3.15)$$

From Eqns. 3.11 and 3.15, we note that χ is independent of \mathcal{D} .

Finally, the dust optical depth in the LW band is calculated as:

$$\tau_c = \frac{\Sigma_d Q_{abs}(r_d)}{\frac{4}{3} r_d \delta}, \quad (3.16)$$

z	$\text{Log}(M_*)$ [M_\odot]	\dot{M}_* [$M_\odot \text{yr}^{-1}$]	$\text{Log}(M_{\text{CNM}})$ [M_\odot]	M_d [M_\odot]	$\langle f_{\text{H}_2} \rangle$	$\langle M_{\text{H}_2} \rangle$ [M_\odot]	$\langle L_{\text{CO}} \rangle$ [K km/s pc ²]	$\langle S_{\text{CO}} \rangle$ [mJy]
5.7	8.0-10.4	0.8-120	8.4-10.1	3.4-7.2	0.6	$10^{8.9}$	$10^{9.0}$	0.2
6.6	8.1-10.0	1.6-46.4	8.5-9.8	4.0-6.9	0.3	$10^{8.4}$	$10^{8.5}$	0.06

Table 3.2: For all the LAEs at the redshifts shown (col. 1), we show the range of stellar mass (col. 2), the range of SFR (col. 3), the range of cold neutral medium mass (col. 4), the range of dust mass (col. 5), the average molecular fraction (col. 6), the average mass of molecular hydrogen (col. 7), the average intrinsic CO(1–0) luminosity (col. 8), and the average value of CO(6–5) flux (col. 9).

where the dust surface density $\Sigma_d = M_d/(\pi R_d^2)$ and $R_d \approx (0.6, 1.0) \times r_e$ at $z \approx (5.7, 6.6)$ as required to best fit the LAE UV luminosity functions (Dayal et al., 2010).

Once these calculations have been carried out, the total molecular hydrogen mass, M_{H_2} in each LAE is estimated as

$$M_{\text{H}_2} = f_{\text{H}_2} M_{\text{HI}}, \quad (3.17)$$

where $M_{\text{HI}} = f_4 M_H$ is the neutral hydrogen mass in the gas disk within a radius r_e and scale height H , where star formation takes place.

3.3 Results

Once that the above calculations have been carried out, we can discuss the results regarding the molecular hydrogen fraction and the total H₂ mass, and relate these to the physical properties of LAEs at $z \approx 5.7, 6.6$. In what follows, we also calculate the visibility of such LAEs through their CO emission and end by making predictions for such detections in the ALMA Early Science.

3.3.1 Molecular hydrogen content of LAEs

As shown in Sec. 3.2.1, the H₂ fraction is decided by three important physical parameters: (a) the SFR which determines the intensity of the H₂-dissociating LW field, (b) the amount of cold gas available to shield the MC against the LW field, and (c) the dust mass on which the H₂ forms, and which additionally shields the molecular hydrogen by absorbing LW photons. We now quantify how the molecular hydrogen fraction depends on each of these parameters.

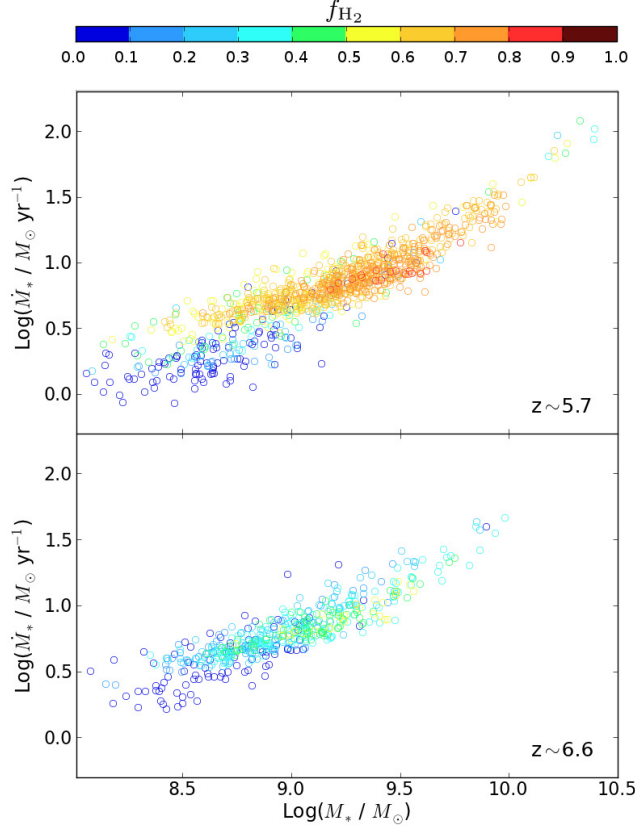


Figure 3.1: The molecular hydrogen fraction, f_{H_2} , of LAEs at $z \approx 5.7$ (6.6) as a function of the stellar mass (M_*) and SFR (\dot{M}_*) are shown in the upper (lower) panels respectively. Points are color-coded for different values of f_{H_2} .

We start our discussion by mentioning that the stellar mass of LAEs ranges between $M_* = 10^{8.0-10.4} M_\odot$ at $z \approx 5.7$. As expected in a hierarchical structure formation scenario where progressively larger objects form from the merger of smaller ones, such range narrows to $M_* \approx 10^{8.1-10} M_\odot$ at $z \approx 6.6$ (see also Tab. 3.2); galaxies with stellar masses above $10^{10} M_\odot$ have not had the time to assemble in large numbers by $z \approx 6.6$. Further, the SFR of LAEs falls in the interval $\dot{M}_* \approx 0.8 - 120 M_\odot \text{ yr}^{-1}$ at $z \approx 5.7$, with larger ($M_* \geq 10^{9.5} M_\odot$) galaxies being the most efficient in star formation. At stellar masses lower than this value, the SFR-stellar mass relation flattens at both the redshifts considered, as seen from Fig. 3.1 due to the stronger effects of mechanical feedback (ejection of gas in outflows) inhibiting star formation (see Dayal et al., 2009). As a result of the narrower stellar mass range, the SFR for $z \approx 6.6$ are concentrated in a narrower range between $1.6 - 46 M_\odot \text{ yr}^{-1}$ (see Tab. 3.2).

As for the molecular hydrogen fraction, starting with $z \approx 5.7$, we find $f_{\text{H}_2} \leq$

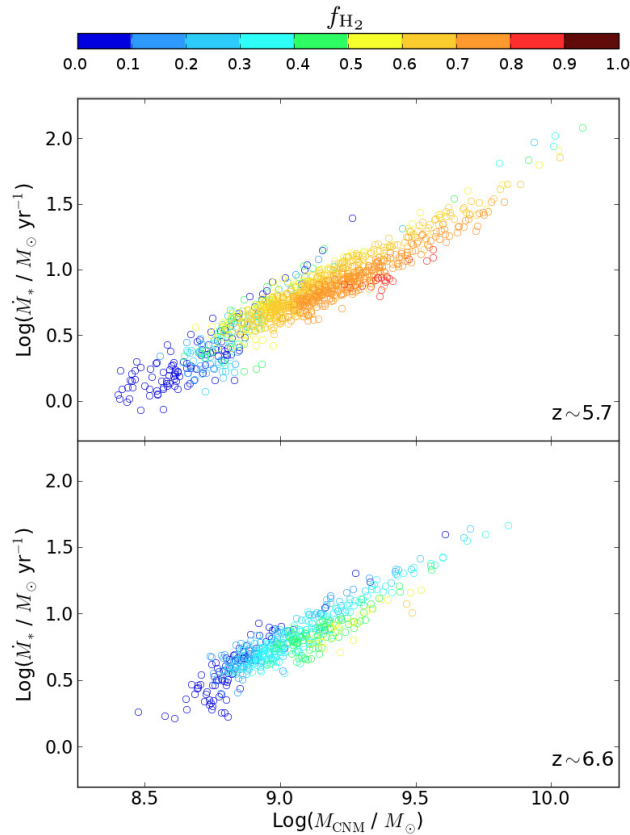


Figure 3.2: The molecular hydrogen fraction, f_{H_2} , of LAEs at $z \approx 5.7$ (6.6) as a function of the stellar mass (M_*) and mass of cold H IISM gas with temperature less than 100 K (M_{CNM}) are shown in the upper (lower) panels respectively. Points are color-coded for different values of f_{H_2} .

0.1 for galaxies with $M_* < 10^9 M_\odot$; it rises to $\approx 0.5 - 0.9$ for intermediate mass galaxies with $M_* = 10^{9-10} M_\odot$ and then decreases again to 0.2-0.6 for the few largest galaxies. Such behavior can be explained as follows: although the smallest galaxies ($M_* < 10^9 M_\odot$) have the smallest SFR (and hence weakest LW field), they also less dusty, resulting in a lower H_2 production rate and self-shielding ability against photodissociation. On the other hand, the larger SFR compared to the dust and cold gas mass in the largest galaxies leads to a decreased f_{H_2} . It is thus the intermediate mass galaxies that show the largest H_2 fraction by virtue of a well-tuned balance between the H_2 formation and dissociation rates. Such argument is supported by the fact that at a given value of the stellar mass, intermediate mass galaxies with the lowest SFR have the largest H_2 fraction as seen from Fig. 3.1. Qualitatively, the situation remains the same at $z \approx 6.6$, although quantitatively, the f_{H_2} value is lower for all LAEs; the reason for this is detailed in what follows.

To understand the f_{H_2} dependence on the cold gas mass (M_{CNM}), we start by

noting that M_{CNM} scales well with the SFR as shown in Fig. 3.2; more massive galaxies have a smaller cold mass fraction, possibly due to stellar sources heating a greater part of the ISM to higher temperatures (see also Tab. 3.1). From the same figure, we see that for a given value of M_{CNM} , galaxies with the lowest SFR have the largest value of f_{H_2} which is easy to understand considering that for a given M_{CNM} , at lower SFR, the H_2 LW dissociation becomes less efficient. Again, it is the intermediate mass galaxies that have the largest value of f_{H_2} , while the H_2 fraction is larger at $z \approx 5.7$ compared to $z \approx 6.6$ for all LAEs.

Dust also plays a key role in terms of the H_2 abundance since this molecule predominantly forms on dust grains which also shield the molecular hydrogen so formed, by absorbing LW photons. The dust mass for each LAE has been calculated as explained in Sec. 3.1.1; since we assume stellar sources (i.e. SNII) to be the main dust producers, the total dust mass scales well with the stellar mass, ranging between $10^{3.4-7.2}M_{\odot}$ at $z \approx 5.7$. As mentioned before, since H_2 forms on dust grains, naively it might be expected that the larger the dust content, the larger the value of f_{H_2} . However, this does not hold true; the LW intensity in the largest galaxies is enough to dissociate the H_2 formed as a result of which, the intermediate mass galaxies end up with the largest H_2 fraction. As expected, at a given value of M_* , galaxies with the largest dust mass have the largest f_{H_2} value (Fig. 3.3).

Finally, we discuss why the value of f_{H_2} is lower at $z \approx 6.6$ compared to $z \approx 5.7$, even though galaxies identified as LAEs are extremely similar at these redshifts, in terms of M_* , \dot{M}_* , M_d and M_{CNM} (see Tab. 3.2): as mentioned in Sec. 3.2.1, the value of the dust distribution radius, $r_d = (0.6, 1.0)r_e$ at $z \approx (5.7, 6.6)$, is fixed by matching the observed LAE UV luminosity functions. These values imply that the dust is more concentrated in the inner parts of LAEs than the stars themselves, perhaps hinting at the existence of dust/metallicity radial gradients. We note that r_e , the stellar distribution scale, is similar at both the redshifts considered. The larger value of r_d results in a dust optical depth that is about 1.6 times smaller at $z \approx 6.6$ as compared to that 5.7 (see Eq. 3.16); although comparable H_2 masses would be produced in LAEs with similar physical properties at both $z \approx 5.7$ and 6.6, a larger amount is dissociated at $z \approx 6.6$ due to a decreased dust absorption of H_2 -dissociating LW photons. Averaged over all LAEs, $f_{\text{H}_2} \approx 0.6$ at $z \approx 5.7$, and only $f_{\text{H}_2} \approx 0.3$ at $z \approx 6.6$, as seen from Fig. 3.4 and Tab. 3.2. From the same figure, we see that while f_{H_2} covers the broad range $0 - 0.85$ at $z \approx 5.7$, no LAEs have $f_{\text{H}_2} \geq 0.65$ at $z \approx 6.6$, as a result of the smaller dust optical depth. Finally,

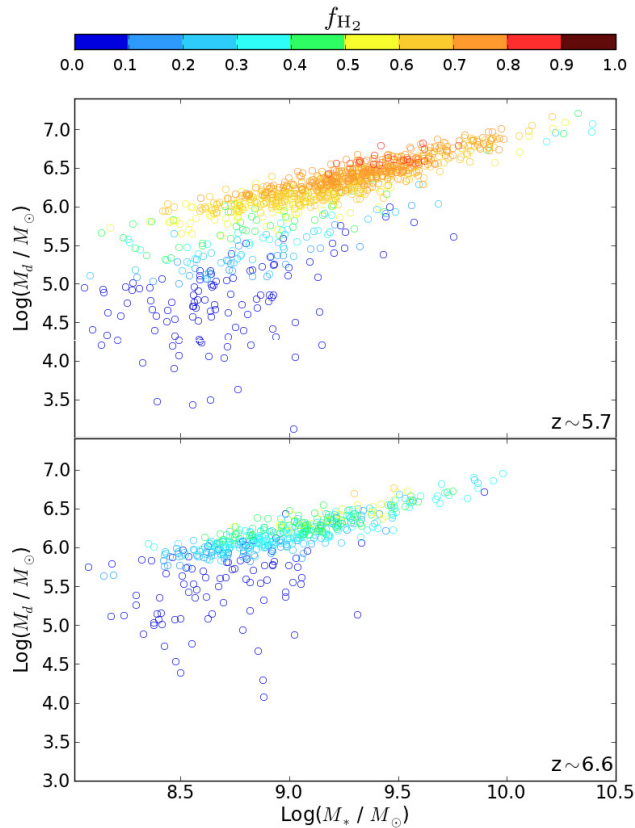


Figure 3.3: The molecular hydrogen fraction, f_{H_2} , of LAEs at $z \approx 5.7$ (6.6) as a function of the stellar mass (M_*) and dust mass (M_d) are shown in the upper (lower) panels respectively. Points are color-coded for different values of f_{H_2} .

translating the value of f_{H_2} into a total M_{H_2} (Eq. 3.17), we find the average value of $M_{\text{H}_2} \approx 10^{8.9}, 10^{8.4}$ at $z \approx 5.7$ and 6.6 respectively, as shown in Tab. 3.2.

To summarize, we find that intermediate mass LAEs ($M_* \approx 10^{9-10} M_\odot$) have the largest molecular hydrogen fraction; a delicate balance between \dot{M}_* , M_{CNM} and M_d leads to H_2 formation (and self-shielding) dominating over H_2 photo-dissociation. Finally, due to a smaller dust optical depth (by a factor ≈ 1.6) at $z \approx 6.6$, the H_2 fraction is about twice as large at $z \approx 5.7$ for LAEs with comparable physical properties.

3.3.2 CO detectability in LAEs

Now that the dependence of f_{H_2} on the physical properties of LAEs has been understood, we are in a position to make predictions for the H_2 detectability in these galaxies. H_2 has strongly forbidden rotational transitions; the rotational-vibrational

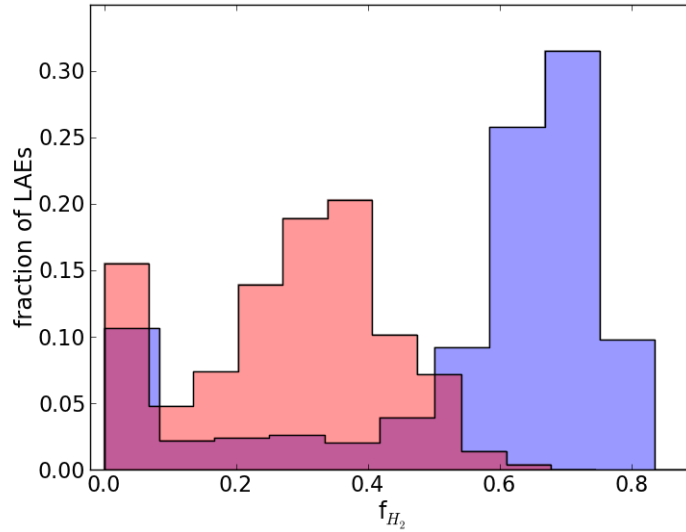


Figure 3.4: Normalized distribution of the number of LAEs as a function of the molecular hydrogen fraction f_{H_2} at $z \approx 5.7$ (dark/blue) and $z \approx 6.6$ (light/red).

lines have very high excitation temperatures, that are attainable only under somewhat extreme conditions involving intense irradiation or shock waves (see [Solomon & Vanden Bout, 2005](#)) in the absence of which the H_2 is invisible. On the other hand, CO has a weak dipole moment: its rotational levels are then easily excited and thermalized by collisions with H_2 . In addition, CO is a very stable molecule and the most abundant after H_2 (e.g. [Solomon & Vanden Bout, 2005](#); [Omont, 2007](#)). Because of such considerations, it is popularly used as a tracer of H_2 .

The luminosity of the CO(1–0) transition can be related to M_{H_2} mass as

$$L_{CO} = M_{H_2}/\alpha. \quad (3.18)$$

The parameter α used in the equation above depends on the distribution of star forming clouds: in the Milky Way, where star formation takes place in molecular clouds with dense cores, confined by self gravity, $\alpha = 4.6 M_{\odot} K km s^{-1} pc^2$ ([Solomon et al., 1987](#)). On the other hand, in high-redshift Ultra Luminous Infrared Galaxies (ULIRGs), where star formation is expected to occur in a dense intercloud medium bound by the potential of the galaxy, α has a much lower value of $0.8 M_{\odot} K km s^{-1} pc^2$ ([Downes & Solomon, 1998](#)). It is worth noting that the value of α is also related to the metallicity of the interstellar gas (e.g. [Leroy et al., 2009](#); [Narayanan et al., 2011](#); [Genzel et al., 2011](#)). Using the Green Bank telescope, [Wagg](#)

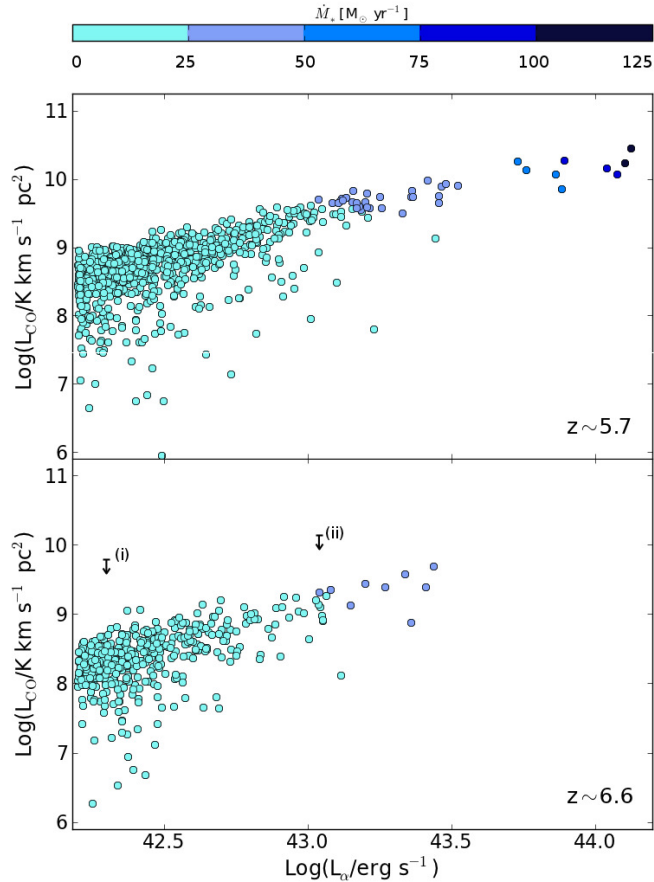


Figure 3.5: As a function of the observed L_{α} luminosity (L_{α}), we show the estimated CO luminosity at $z \approx 5.7$ and 6.6 in the upper and lower panels respectively; the points shown are color-coded according to the SFR. In the lower panel, the arrows indicate the upper limit on the L_{CO} obtained by Wagg et al. (2009): (i) corresponds to the nondetection of the CO (1-0) line of HCM 6A, a LAE at $z \approx 6.6$, with $SFR \approx 2 M_{\odot} \text{yr}^{-1}$ (Hu et al., 2002). (ii) corresponds to the nondetection of the CO (1-0) line of IOK-1, a $z \approx 7$ LAE with $SFR \approx 10 M_{\odot} \text{yr}^{-1}$ (Iye et al., 2006).

et al. (2009) undertook a search for CO emission in two LAEs at $z > 6$, and they adopted the ULIRG value of the conversion factor to estimate M_{H_2} . For a reasonable comparison with such LAE data, we use the same value of $\alpha = 0.8 M_{\odot} \text{K km s}^{-1} \text{pc}^2$ to compute the CO(1–0) luminosity values for simulated LAEs at $z \approx (5.7, 6.6)$. We find that the value of L_{CO} scales with L_{α} for both the redshifts considered as shown in Fig. 3.5; quantitatively we find, $L_{CO} \propto L_{\alpha}^{(1.04, 1.07)}$ at $z \approx (5.7, 6.6)$ respectively. Although such a relation has a huge scatter, this implies that the brightest LAEs are the best candidates for molecular emission searches.

Interestingly, such a trend also implies that although the value of f_{H_2} is the largest for the intermediate mass/luminosity LAEs (see Sec. 3.3.1), the increasingly

large neutral hydrogen mass, M_{HI} , in the star forming disk (see Eq. 3.17) of massive galaxies wipes out such a subtle signature, whose imprint remains as a flattening of the $L_{\text{CO}} - L_{\alpha}$ relation towards the most luminous objects. As expected, as a result of their lower dust optical depth, and hence, a lower molecular hydrogen fraction, the CO luminosity for LAEs is smaller at $z \approx 6.6$ than at $z \approx 5.7$; averaged over all LAEs, the CO luminosity at $z \approx 6.6$ is about a factor 3 lower than that at $z \approx 5.7$, as shown in Tab. 3.2. As a validation of our model, our theoretical L_{CO} estimates are in accord with the upper limits found by Wagg et al. (2009) for their observed LAEs, as seen from lower panel of Fig. 3.5, which represents an encouraging sanity check of our model. Finally, we note that α is expected to be larger than the Galactic value in low metallicity environments (Leroy et al., 2009; Narayanan et al., 2011; Genzel et al., 2011), which is likely the case for LAEs, while we have used a value derived using ULIRGs. As expected, an increase in the value of α would lead to a decrease in the CO luminosity, thereby negatively affecting the CO detectability of LAEs.

3.3.3 Predictions for ALMA early science

Now that the CO(1–0) luminosity has been calculated for all LAEs in our simulation, we make predictions for the detectability of such CO lines using ALMA. As of now, these observations have been limited to the most luminous high- z sources such as QSOs (e.g. Cox et al., 2002; Bertoldi et al., 2003; Walter et al., 2004; Weiß et al., 2007; Wang et al., 2010; Riechers et al., 2011) and sub-millimeter galaxies (SMG) (e.g. Greve et al., 2005; Tacconi et al., 2006); normal galaxies such as Lyman break galaxies (LBGs) have only been detected at a much lower redshifts, $z \approx 3$. We start by noting that ALMA Early Science (Cycle 0) consists of the use of 16 antennas and a limited number of Bands. In this configuration, the lowest CO rotational transition observable at $z \approx 5.7$ is CO(5–4) ($\nu_{\text{rest}} = 576.267$ GHz), which falls within ALMA Band 3 (84 – 116 GHz). However, as is shown in what follows, the rotational transition strength of the CO(5–4) line is quite comparable to that of CO (6–5). The latter is the lowest line observable with ALMA Cycle 0 for both ($z \approx 5.7, 6.6$) samples, for which reason we show results for the CO(6–5) transition in what follows; in the future, using the the full capabilities of ALMA, lower frequency bands (31.3–45, GHz and 67–90 GHz) will also allow for the study of lower-J CO line transitions at high redshift.

We now describe how we translate the CO(1–0) luminosities calculated above in Sec. 3.3.2 in to CO(6–5) luminosities. Theoretical fits to observational CO spectral energy distributions have been carried out by several authors using Local Thermal Equilibrium (LTE; Obreschkow et al., 2009) or Large Velocity Gradient (LVG) models (Bayet et al., 2009) to describe the molecular gas. We use the model proposed by Obreschkow et al. (2009) which assumes a single gas component in LTE. In this framework, the frequency integrated luminosity from the transition ($J \rightarrow J-1$) can be expressed as (Obreschkow et al., 2009):

$$L(J \rightarrow J-1) \propto 1 - \exp(-\tau_J) \cdot \frac{J^4}{\exp\left(\frac{h\nu_{\text{CO}}J}{k_b T_e}\right) - 1}, \quad (3.19)$$

where $T_e = 100$ K is the gas excitation temperature, $\nu_{\text{CO}} = 115.271$ GHz is the rest-frame frequency of the CO(1–0) transition, τ_J is the optical depth and k_b is the Boltzmann constant. Further, τ_J can be expressed as

$$\tau_J = 7.2\bar{\tau}\exp\left(-\frac{h\nu_{\text{CO}}J^2}{2k_b T_e}\right)\sinh\left(\frac{h\nu_{\text{CO}}J}{2k_b T_e}\right), \quad (3.20)$$

where $\bar{\tau}$ is an experimental determined normalization constant, which we take to be $\bar{\tau} = 2$, following the results of Obreschkow et al. (2009).

Considering that the frequency of the ($J \rightarrow J-1$) transition is related to that of (1-0) by $\nu_J = J\nu_{\text{CO}}$, and using the relation between frequency-integrated luminosity L , and the brightness temperature luminosity L_{CO} (cfr. App. A, Obreschkow et al., 2009):

$$L_{\text{CO}} = (8\pi k_b)^{-1}\lambda_e^3 L = (8\pi k_b)^{-1}\left(\frac{c}{\nu_e}\right)^3 L, \quad (3.21)$$

we obtain the $L_{\text{CO}}(6-5)$ luminosity in units of $[\text{K km s}^{-1} \text{ pc}^2]$ and find that $L_{\text{CO}}(6-5) = 1.58 L_{\text{CO}}(1-0)$, while $L_{\text{CO}}(5-4) = 1.75 L_{\text{CO}}(1-0)$; all the results presented for the CO(6–5) transition also remain largely valid for the CO(5–4) transition.

This line luminosity can be converted into the line integrated flux, S_{CO} such that

$$L_{\text{CO}} = 3.25 \times 10^7 S_{\text{CO}} \Delta V \nu_{\text{obs}}^{-2} (1+z)^{-3} D_L^2 \quad (3.22)$$

where $S_{\text{CO}} \Delta V \equiv S^V$ is the velocity integrated flux $[\text{Jy km s}^{-1}]$, ν_{obs} is the observed frequency in GHz, and D_L is the luminosity distance. We then assume that the CO(6–5) line has a gaussian profile with a width given by the rotational velocity of

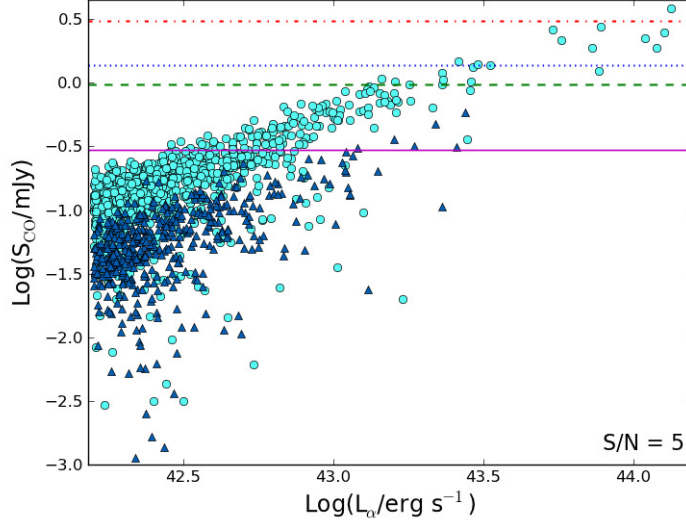


Figure 3.6: The line integrated CO(6–5) flux, S_{CO} , as a function of the L_{α} observed for LAEs at $z \approx 5.7$ (circles) and $z \approx 6.6$ (triangles). Horizontal lines represent the ALMA Cycle 0 sensitivity for a signal-to-noise ratio of 5, for an integration time of 1 hour (dot-dashed line), 5 hours (dotted line) and 10 hours (dashed line), assuming a spectral resolution of 50 km/s. Solid line represents the sensitivity ($S/N = 5$) achieved with 10 hours of integration time with 50 antennas.

the galaxy, v_r , which we take to be equal to 1.5 times the halo rotation velocity (see Dayal et al., 2009). The average value of v_r for LAEs at both the redshifts considered is of order of 200 km/s. The observable CO flux S_{CO} can then be expressed as $S_{\text{CO}} \simeq S^V/v_r$.

As noted in Sec. 3.3.2, the CO(1–0) luminosity value scales with the observed Ly α luminosity; the line integrated flux is therefore also expected to behave in a similar way. This is indeed the case, as seen from Fig. 4.1. Albeit with a large scatter, galaxies with the largest Ly α luminosity show the largest value of $S_{\text{CO}}(6-5)$ at both $z \approx 5.7, 6.6$; as expected from a comparison of the CO(1–0) luminosities, the average value of S_{CO} is about 3 times lower at $z \approx 6.6$, compared to $z \approx 5.7$ (Tab. 3.2). We find that at $z \approx 6.6$ none of the LAEs would be detectable in CO, even with an ALMA Cycle 0 integration time for about 10 hours. On the other hand, at $z \sim 5.7$, about 1-2% of LAEs, i.e., those with $L_{\alpha} \geq 10^{43.2} \text{erg s}^{-1}$ could be detectable with an ALMA integration time of 5-10 hours (i.e. a detection limit of $\sim 1-1.4$ mJy respectively), assuming a signal-to-noise ratio $S/N = 5$. However, using 50 antennas of ALMA with an integration time of 10 hours increases the sensitivity to about 0.3 mJy making a significant change such that about 13%, 1.4% of LAEs

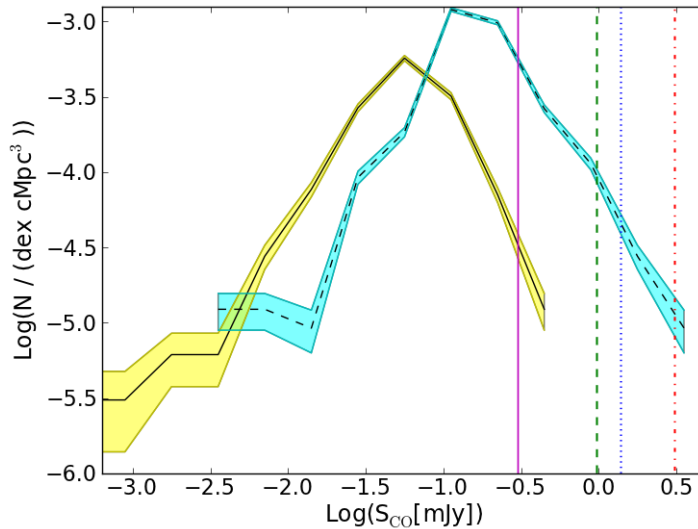


Figure 3.7: The number density of LAEs at $z \approx 5.7$ and 6.6 are shown as a function of the line integrated CO(6–5) flux using dashed and solid lines respectively; shaded regions show the poissonian errors. Vertical dot-dashed, dotted and dashed lines represent the ALMA sensitivity limits for 16 antennas assuming a signal to noise ratio, $S/N = 5$, for an integration time of 1, 5 and 10 hours respectively. Vertical solid line represents the sensitivity ($S/N = 5$) achieved with 10 hours of integration time with 50 antennas.

become detectable at $z \approx 5.7$ and 6.6 respectively.

To clarify such results, we present the CO ‘flux function’, i.e. the number density of LAEs as a function of the line integrated CO flux, $S_{\text{CO}}(6-5)$. As is clearly seen again, none of the $z \approx 6.6$ LAEs are detectable with the Cycle 0 of ALMA, even for a 10 hour detection limit of about 1 mJy. On the other hand, the $z \approx 5.7$ flux function, extends into the 1-10 ALMA detection bands as mentioned above. However, the peak of the function lies at $S_{\text{CO}} \approx 0.1$ mJy at $z \approx 5.7$; due to the lower H_2 mass at $z \approx 6.6$, the flux function peaks at a lower value of about 0.06 mJy. As mentioned above, using 50 ALMA antennas for an integration time of 10 hours increases the number of LAEs detectable in CO; as expected, this leads to a larger part of the ‘flux function’ being observed at both the redshifts considered.

3.4 Summary

We now summarize the main results achieved with the model presented in this Chapter:

- We find that at $z \approx 5.7$, the value of the molecular fraction peaks and ranges between 0.5 – 0.9 for intermediate mass LAEs with $M_* \approx 10^{9-10} M_\odot$, decreasing for both smaller and larger galaxies; this trend also holds at $z \approx 6.6$. Such behaviour can be explained as follows: compared to intermediate mass galaxies, smaller galaxies have smaller SFR (and hence a lower value of the dissociating LW field), lower dust masses for forming H_2 , and a lower cold gas (and dust) mass for self-shielding the H_2 so formed against the dissociating LW field; on the other hand, the larger SFR compared to the dust and cold gas mass in the largest galaxies leads to a lower f_{H_2} . Such an argument is validated by the fact that at a given stellar mass, galaxies with the lowest SFR, largest cold gas mass, and largest dust mass have the largest value of f_{H_2} .
- Further, we find that for LAEs with comparable SFR/gas mass/dust masses, f_{H_2} is about twice as large at $z \approx 5.7$ than at 6.6; to reproduce the LAE UV luminosity function data, the dust distribution radius at $z \approx 6.6$ is about 1.6 times larger than that at 5.7, for similar LAE properties. As a result, the dust optical depth to LW photons is lower at $z \approx 6.6$ which leads to a larger amount of H_2 being dissociated.
- We then translate the H_2 mass we obtain into a CO luminosity. Recently, [Wagg et al. \(2009\)](#) used the green bank telescope to look for CO emission in two LAEs at $z > 6$ both of which resulted in non-detections. To compare our model predictions to their observations, we used a value of $\alpha = 0.8 M_\odot \text{ K km s}^{-1} \text{ pc}^2$ to translate the H_2 mass into a CO(1–0) luminosity, L_{CO} . We find that the value of L_{CO} scales with L_α , for both the redshifts considered; although the value of f_{H_2} is the largest for the intermediate mass/luminosity LAEs (see Sec. 3.3.1), the increasingly large neutral hydrogen mass, M_{HI} , in the star forming disk of increasingly massive galaxies wipes out such a subtle signature. This result also implies that the brightest LAEs are the best candidates for molecular emission searches. As a reasonable validation of our model, our theoretical L_{CO} estimates are in accord with the upper limits found by [Wagg et al. \(2009\)](#) in their experimental work.
- At $z \approx 5.7, 6.6$, the lowest CO rotational transition observable with ALMA is the CO(6-5). We find that at $z \approx 5.7$, about 1-2% of the LAEs, i.e. those with

$L_\alpha \geq 10^{43.2} \text{erg s}^{-1}$, could be detectable with an integration time of 5-10 hours respectively, assuming a signal-to-noise ratio $S/N = 5$. Our results at $z \approx 6.6$ are more pessimistic; none of the LAEs would be detectable in CO, even with an ALMA integration time of about 10 hours. We also present the CO flux function, the number density of LAEs as a function of S_{CO} where we show that the number density of objects peaks at a value of about 0.1 mJy, which is much beyond the sensitivity of ALMA; this peak shifts to progressively lower values with increasing redshift.

We finally conclude this Chapter by discussing the caveats of our model. First, the calculations presented here concern only average quantities in a spherically symmetric framework and a full calculation of the radial dependence of f_{H_2} is necessary to shed light on internal distribution of molecular gas. Secondly, the dust masses used in this work have been calculated assuming SNII to be the primary sources of dust production which is a reasonable assumption given that a number of authors (Todini & Ferrara, 2001; Dwek et al., 2007) have shown that the contribution of AGB stars becomes progressively less important and at some point negligible towards higher redshifts ($z \gtrsim 5.7$) when the Universe is less than 1 Gyr old. However, it must be noted that under certain conditions thought to hold in quasars, in which extremely massive starbursts occur, the contribution of AGB can become important somewhat earlier (see Valiante et al., 2009). Thirdly, the stellar distribution scale (and radial extent of the MC) is based on estimates following the results of Bolton et al. (2008), who have derived fitting formulae relating the V-band luminosity and the stellar distribution scale from their observations of massive, early type galaxies between $z = 0.06 - 0.36$; however, we note that such estimates are in surprisingly good agreement (to within $1-\sigma$) with recent observational results of $z \approx 5.7$ LAEs (Malhotra et al., 2011).

Fourthly, the large cosmological volume simulated naturally results in a low mass resolution, such that we are unable to resolve density and temperature of the gas in the interior of individual galaxies. We have therefore estimated the ISM gas temperature distribution over broad halo mass bins.

Further, in our calculations, we have assumed that half of the gas mass with temperatures of $T < 10^4$ K is cold, with $T < 100$ K. Finally, we have used a ULIRG value for the factor α , used to translate the H_2 mass into a CO luminosity. However, this parameter depends on a number of poorly known properties of high- z galaxies,

such as the spatial/mass distribution of their MCs and the gas metallicity (Leroy et al., 2009; Narayanan et al., 2011; Genzel et al., 2011).

FIR line emission from the diffuse gas 4

THE SEMI-ANALYTICAL model outlined in the previous Chapter has been developed with the aim of providing a global estimate of the molecular content in large samples of simulated galaxies. The upward of this approach is that with very few inputs we are able to achieve a physically motivated prediction of the f_{H_2} within each galaxy. The drawback, due to the lack of resolution, is the impossibility of catching the internal structure of the ISM that, as clarified in Chapter 2, is a complex environment constituted by various gas phases with completely different physical properties. The molecular gas is actually organized in molecular clouds that are embedded in the diffuse gas, hence a proper description of the relative abundance of molecular, neutral, and ionized gas requires simulations that reach sub-kpc resolutions.

In this Chapter we present the step forward achieved in this direction during the Thesis. We model the physical conditions of the diffuse neutral gas in the ISM of a galaxy extracted from a cosmological simulation at $z = 6.6$. With this simulation, fully implemented with the UV radiative transfer, we reach a sufficiently high resolution to properly describe the ISM small-scale density structure and to achieve one of the first detailed predictions so far available, for the intensity of several FIR emission lines ($[\text{C II}]$ 158 μm , $[\text{O I}]$ 63 μm , and $[\text{N II}]$ 122 μm). These lines (see Chapter 2 for the complete discussion) are the main coolants of the diffuse gas and, from $z > 4$, fall within the ALMA bands (see Fig. 1.5).

The $[\text{C II}]$ line is the dominant coolant of the neutral ISM (e.g. Dalgarno & McCray, 1972; Stacey et al., 1991; Wolfire et al., 1995; Lehner et al., 2004), and

by far the most luminous FIR line. It has been observed at high- z in numerous galaxies with high star formation rates ($>100 M_{\odot}y^{-1}$) (e.g. Cox et al., 2011; De Breuck et al., 2011, 2014) and in those hosting Active Galactic Nuclei (AGN) (e.g. Maiolino et al., 2005; Venemans et al., 2012; Gallerani et al., 2012; Wang et al., 2013; Willott et al., 2013).

The same happens for other FIR lines such as the [O I] and [N II]. [O I] detections at high- z have been reported in two lensed Ultra-Luminous Infrared Galaxies at $z = 1.3$ and $z = 2.3$ (Sturm et al., 2010) and in submillimetre galaxies at $z \sim 1$ (Coppin et al., 2012); [N II] lines at $z > 4$ have been detected in quasars and submillimeter galaxies (Ferkinhoff et al., 2011; Nagao et al., 2012; Decarli et al., 2012; Combes et al., 2012; Decarli et al., 2014). As pointed out in Sec. 1.6.2, the unprecedented sensitivity of ALMA is expected to allow the detection of FIR lines from the normal star forming galaxies at high- z (e.g. Carilli & Walter, 2013, and references therein) as, for instance, in the case of [C II] detections in two $z = 4.7$ LAEs presented by Carilli et al. (2013). Hence, developing models to predict FIR line luminosities, and relate them to galaxy physical properties such as the metallicity Z and the SFR is fundamental to design and interpret future experiments.

Moreover, high redshift sources discovered by means of their Lyman- α emission line (e. g. Malhotra et al., 2005; Shimasaku et al., 2006; Hu et al., 2010; Ouchi et al., 2010) or through drop-out techniques (e.g. Steidel et al., 1996; Castellano et al., 2010; Bouwens et al., 2011; McLure et al., 2011) are plagued with intrinsic limitations: the Ly α detection is hampered by the increasingly neutral intergalactic medium, while the source redshift cannot be precisely determined with drop-out techniques; in addition the restframe optical/UV radiation is strongly extinguished by the presence of the dust. It is then important to assess whether other probes, as the FIR metal cooling lines, can be used to detect *new* sources at the end of the reionization epoch, or better determine the properties of those already discovered. These lines, not affected by [H I] or dust attenuation, can deliver the precise redshift of the emitter, and open a window to investigate the structure of the galactic ISM.

The work that we are going to present in this Chapter is similar in spirit to that of Nagamine et al. (2006), who computed the [C II] galaxy luminosity function based on a SPH simulation coupled with a sub-grid multi-phase model of the ISM. However we improve upon Nagamine et al. (2006) work in at least two ways: (a)

by incrementing the spatial resolution of the simulation and (b) by performing the UV radiative transfer within the galaxy.

4.1 Numerical Simulations

We run cosmological SPH hydrodynamic simulations using GADGET-2 (Springel, 2005). We use the recent WMAP7+BAO+ H_0 cosmological parameters: $\Omega_m = 0.272$, $\Omega_\Lambda = 0.728$, $\Omega_b = 0.0455$, $h = 0.704$, $\sigma_8 = 0.807$ (Komatsu et al., 2011). We simulate a $(10h^{-1}\text{Mpc})^3$ comoving volume with 2×512^3 baryonic+dark matter particles, giving a mass resolution of $1.32 (6.68) \times 10^5 M_\odot$ for baryons (dark matter) and gravitational softening $\epsilon = 2h^{-1}\text{kpc}$. We select a snapshot at redshift $z = 6.6$, and we identify the most massive halo (total mass $M_h = 1.17 \times 10^{11} M_\odot$, $r_{\text{vir}} \approx 20$ kpc) by using a Friend-of-Friend algorithm. We select a $(0.625 h^{-1}\text{Mpc})^3$ comoving volume around the center of the halo, and post-processed UV radiative transfer (RT) using LICORICE (Baek et al., 2009). LICORICE uses a Monte Carlo ray-tracing scheme on an adaptive grid. We set the adaptive grid parameter to have a minimum RT size of $0.61 h^{-1}\text{kpc}$. Starting from the density field provided by GADGET, we recompute gas temperature including atomic cooling from the initial temperature $T_0 = 10^4$ K. The initial ionization fraction is set to $x_{\text{HII}} = 0$.

To define the position of the ionizing sources we assume that stars form in those cells characterized by a gas density $\rho \geq \rho_{\text{th}}$. We choose $\rho_{\text{th}} = 1 \text{ cm}^{-3}$ in order to reproduce the typical size ($\sim 1 - 2$ kpc) of star forming regions at $z \approx 6$ (Bouwens et al., 2004; Ouchi et al., 2009), as inferred by UV continuum emitting images. The projected position of stellar sources is shown in white in the upper left panel of Fig. 4.1. A central large stellar cluster is clearly visible, along with other 3 minor stellar clumps displaced from the center. We use the population synthesis code STARBURST99 (Leitherer et al., 1999) to obtain the ionizing spectrum of the galaxy. Theoretical works suggest that high- z galaxies might be relatively enriched ($Z \gtrsim 0.1 Z_\odot$) galaxies (Dayal et al., 2009; Salvaterra et al., 2011). We adopt $Z = Z_\odot$ as a fiducial value for our study but we also consider a lower metallicity case, i.e. $Z = 0.02 Z_\odot$. We assume a Salpeter initial mass function with a slope of $\alpha = 2.35$ in the mass range $1-100 M_\odot$, a continuous star formation rate of $10 M_\odot \text{ yr}^{-1}$, obtained from the SFR- M_h relation at $z = 6.6$ (Baek et al., 2009, 2012). Ionizing UV luminosity is about $L_{\text{UV}} \approx 7 \times 10^{43} \text{ erg s}^{-1}$. RT calculations are performed until equilibrium between photoionizations and recombinations is

achieved; this occurs within ≈ 10 Myr. The public version of GADGET-2 used in this work does not include the star formation process, neither the radiative cooling, nor supernova feedback. The inclusion of radiative cooling may affect the baryon density profile, enhancing the density towards the center of the galaxy, whereas supernova feedback tends to smooth out density inhomogeneities. We have checked that the baryon density profile resulting from the simulations used in this work fits well with our previous low resolution simulations which include all these processes (Baek et al., 2009). Finally, we note that the large gravitational potential of massive galaxies reduces the effects of SN feedback on star formation, as exemplified by Fig. 1 of Vallini et al. (2012) and related discussion. We interpolate all gas physical properties around the halo center on a fixed 512^3 grid using the SPH kernel and smoothing length, within a $(0.156 h^{-1} \text{Mpc})^3$ comoving volume. We achieve a higher resolution by interpolating on a finer grid as shown in Fig. 6 of (Baek et al., 2012). This method also allows us to have continuous density PDF at low and high dense region thus increases the maximum density about 50% from 64^3 grid to 512^3 grid. The resulting hydrogen column density map is shown in the upper right panel of Fig. 4.1.

4.2 Multiphase ISM model

With current computational resources, it is not possible to self-consistently include sub-kpc scale physics in the above RT simulations. To this aim we adopt a sub-grid scheme based on the model by Wolfire et al. (1995, 2003, hereafter W95, W03), in which ISM thermal equilibrium is set by the balance between heating (cosmic rays, X-rays, and photoelectric effect on dust grains) and cooling (H, He, collisional excitation of metal lines, recombination on dust grains) processes (see Tab. 2.4):

$$\mathcal{L}(n, x_e, T) = n^2 \Lambda - n \Gamma = 0, \quad (4.1)$$

where $n\Gamma$ ($n^2\Lambda$) is the heating (cooling) rate per unit volume [$\text{erg s}^{-1} \text{cm}^{-3}$], and n is the total gas density. The ISM can be described as a two-phase gas¹ in which the cold and the warm neutral medium are in pressure equilibrium. Each cell of the

¹Our multi-phase model does not include molecular clouds and therefore emission from dense photodissociation regions (PDRs) which we plan to address in future work.

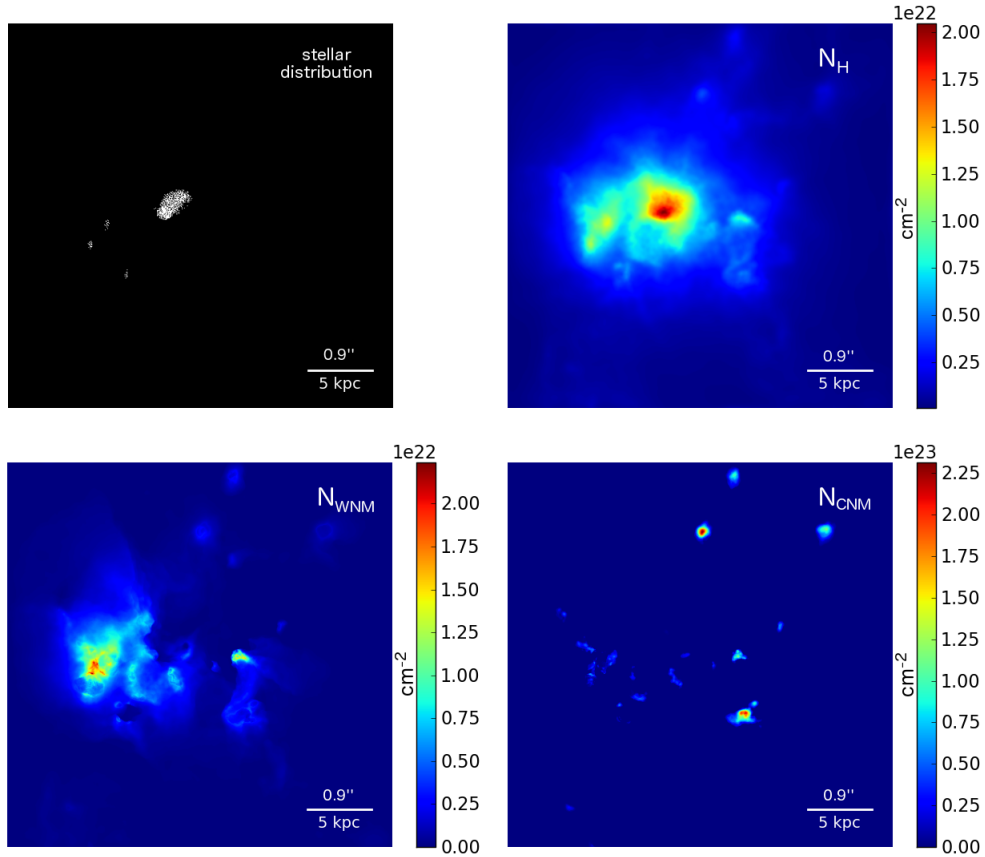


Figure 4.1: *Upper panels:* Projected stellar distribution (left) and hydrogen column density (right). *Lower panels:* warm (left), and cold (right) neutral medium column density. The distribution of WNM is more diffuse compared to that of CNM which is predominantly found in small ($D \leq 2$ kpc) clumps far from star forming regions.

simulated volume is characterized by a pressure $p = (1 + x_e)nk_bT$, where x_e is the ionized fraction, taken from the RT simulation output. We determine the density and the temperature of the CNM and WNM by solving Eq. 4.1, coupled with the ionization equilibrium equation. As metal cooling is not implemented neither in GADGET-2, nor in LICORICE the gas cannot cool below $T_{\min} \approx 7700$ K. We apply the sub-grid ISM multi-phase model only to cells with $T_{\min} \leq T \leq 10^4$ K where the upper limit is determined by the fact that metals dominate the cooling for temperatures below 10^4 K. The rates of photoelectric effect and recombination on dust grains strongly depend on the FUV incident radiation. The incident radiation field (G) in the Habing band (6 – 13.6 eV) is computed at each pixel position $\vec{r} = (x, y, z)$, summing contributions from all sources as following,

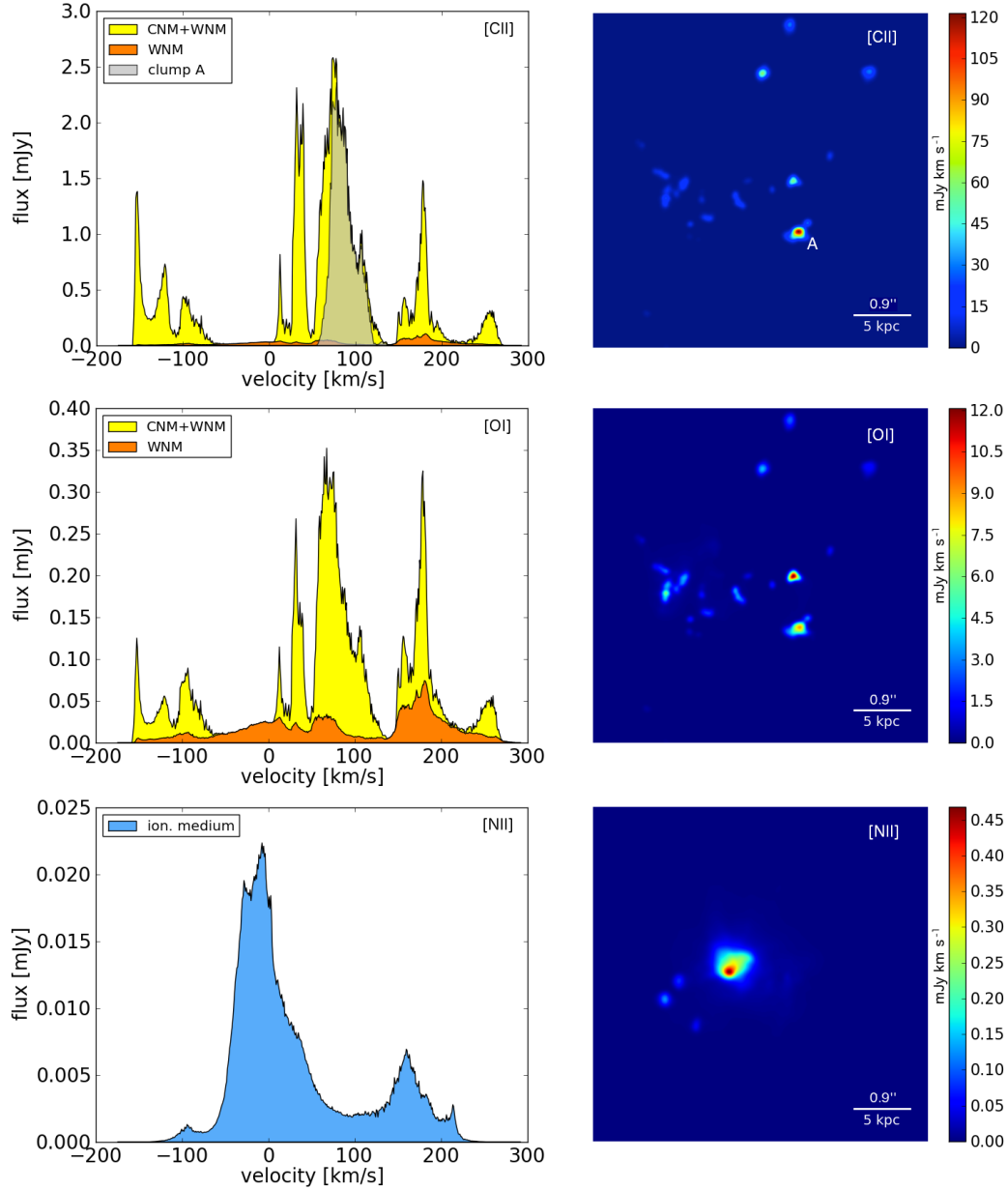


Figure 4.2: *Left column:* Total (CNM+WNM) and WNM only (orange) spectrum of [C II], [O I] and [N II] binned in 1.0 km s^{-1} channels. *Right column:* [C II], [O I] and [N II] maps in mJy km s^{-1} with resolution of 0.1 arcsec and integrated over the entire spectral velocity range. The contribution of clump A to the [C II] spectrum is plotted in gray.

$$G(\vec{r}) = \sum_{i=1}^{n_*} \frac{\int_{6\text{eV}}^{13.6\text{eV}} L_{\nu,i} d\nu}{4\pi|\vec{r} - \vec{r}_i|^2}, \quad (4.2)$$

where $L_{\nu,i}$ is the monochromatic luminosity per source, n_* is the number of sources, and \vec{r}_i represents their positions. By scaling the flux with the Habing value ($1.6 \times 10^{-3} \text{ erg cm}^{-2} \text{ s}^{-1}$) (Habing, 1968) we obtain the standard flux G_0 . Within our simulated galaxy we obtain $0.5 < \log G_0 < 5$. We find that the mean CNM (density, temperature) is ($\langle n_{\text{CNM}} \rangle = 50 \text{ cm}^{-3}$, $\langle T_{\text{CNM}} \rangle = 250 \text{ K}$), while for the WNM we obtain instead ($\langle n_{\text{WNM}} \rangle = 1.0 \text{ cm}^{-3}$, $\langle T_{\text{WNM}} \rangle = 5000 \text{ K}$).

In the lower panels of Fig. 4.1 we show the WNM and CNM column densities. The WNM distribution closely traces regions of high ($N_H \approx 10^{22} \text{ cm}^{-2}$) total hydrogen column density that are sufficiently far from the central star forming region in order not to become ionized; cold gas lies instead only in small ($D \leq 2 \text{ kpc}$) overdense clumps at the periphery of the galaxy. The maps show that cold gas clumps are surrounded by diffuse halos of warm neutral medium.

4.2.1 FIR emission lines

For each simulated cell we estimate the line luminosities $L_i = \varepsilon_i V_{\text{cell}}$, where the emissivity (ε_i) defined in Sec. 2.6.1, is given by:

$$\varepsilon_i(n_H, T) = \Lambda_i^H \chi_i n_H^2 + \Lambda_i^{e^-} \chi_i x_e n_H^2, \quad (4.3)$$

where n_H and T are the density and temperature of the WNM/CNM, Λ_i^H ($\Lambda_i^{e^-}$) is the specific cooling rate due to collision with H atoms (free electrons) taken from Dalgarno & McCray (1972), and χ_i is the abundance of the i -th species (see Tab. 2.3 and 2.2 for the values adopted through this work). The [N II] line traces the ionized medium since its ionization potential (14.5 eV) exceeds 1 Ryd. Therefore, it provides a complementary view of the ISM with respect to the [C II] and [O I] lines. The [N II] cooling rate due to collisions with free electrons is:

$$\varepsilon_{\text{NII}}(n, T) = \frac{Ah\nu}{n_c} \frac{g_u/g_l}{1 + [(g_u/g_l) + 1] (n_e/n_c)} \chi_{\text{NII}} x_e n^2, \quad (4.4)$$

where $A = 7.5 \times 10^{-6} \text{ s}^{-1}$ is the Einstein coefficient, ν is the frequency for the $^3P_2 \rightarrow ^3P_1$ transition, h is the Planck constant, g_u/g_l is the ratio of the statistical weights

in the upper and lower levels, and $n_c = 300 \text{ cm}^{-3}$ is the [N II] critical density for $T = 10^4 \text{ K}$. We finally compute the observed flux by integrating along the line-of-sight also accounting for the gas peculiar velocity field obtained from the simulation.

4.3 Results

In Fig. 4.2 we show the predicted [C II] $158 \mu\text{m}$, [O I] $63 \mu\text{m}$ and [N II] $122 \mu\text{m}$ emission for the spectral resolution of our simulations (1.0 km s^{-1}), a beam resolution of 0.1 arcsec and $Z = Z_\odot$, along with the maps obtained by integrating the spectra over the full velocity range $-200 < v < 300 \text{ km s}^{-1}$.

The [C II] spectrum contains considerable structure due to the presence of several emitting CNM clumps distributed over the entire galaxy's body ($\sim 20 \text{ kpc}$). The individual sizes of the clumps are however much smaller ($\lesssim 3 \text{ kpc}$). The peak of the spectrum reaches $\sim 2.5 \text{ mJy}$ and it is displaced from the center of the galaxy by about 100 km s^{-1} . This is due to the fact that the gas within the central kpc of our galaxy is highly ionized by the massive stars that form there. We find that 95% of the total [C II] flux originates from the CNM, and only 5% from the WNM. For the [C II] emission line we obtain a flux of $185 \text{ mJy km s}^{-1}$, integrating over $\sim 500 \text{ km s}^{-1}$.

In Fig. 4.2 we plot in grey the spectrum extracted by integrating over a circular area of $\sim 2 \text{ kpc}$ radius, centered on the component labeled A in the map. It dominates the peak of the [C II] spectrum (30% contribution to the total emission), with the remaining $\sim 70\%$ coming from less luminous substructures. This is an important point as with high spatial resolution observations a substantial fraction of the [C II] emission may remain undetected. The FWHM of the main peak is $\sim 50 \text{ km s}^{-1}$, consistent with the marginal detection of [C II] in high- z LAEs (Carilli et al., 2013). We have computed FIR line intensities also for a metallicity $Z = 0.02 Z_\odot$. In this case, the [C II] and [O I] intensities drop by a factor of ~ 1000 and ~ 300 , respectively, whereas the [N II] flux is reduced by a factor of 50. While the WNM emission is $\propto Z$, at very low Z CNM is practically absent, since the lower metal content makes the CNM phase thermodynamically unfavorable. A thorough analysis of the relative fraction of the emission arising from CNM and WNM as a function of Z will be addressed in Chapter 6.

The [O I] spectrum has a shape similar to that of [C II] since for both emission lines we are taking into account the emission arising from the neutral phase of the

ISM. In the case of [O I], 75% of the total flux arises from the CNM and 25% from the WNM. The maximum value of the [O I] flux is ~ 0.35 mJy. The [N II] emission line reaches a maximum flux of 0.022 mJy at $v = 0$. This line traces the ionized phase of the ISM, and the bulk of its emission arises from the center of the galaxy where the ionizing field intensity is higher. In conclusion, the [O I] and [N II] fluxes are ~ 6 and ~ 90 times lower than the [C II] one.

4.4 Comparison with observations

4.4.1 LAE observations

As pointed out in the introduction, FIR line observations in high- z sources have been carried out mainly in quasars and sub-millimeter galaxies. Recently, [Walter et al. \(2012b\)](#) have tried to detect the [C II] emission in *Himiko*, one of the the most luminous LAEs at $z = 6.6$ ([Ouchi et al., 2009](#)). However, they end up only with a 1σ upper limit of 0.7 mJy km s $^{-1}$.

The large size of the *Himiko* Ly α emitting nebula (≥ 17 kpc) makes this object one the most massive galaxies discovered at such high redshifts ([Ouchi et al., 2009](#); [Wagg & Kanekar, 2012](#)). From this point of view, *Himiko*'s properties closely resemble those of the prototypical galaxy selected from our simulation. Moreover, the radius of the region within which we distributed the stars ($\sim 1 - 2$ kpc) is consistent with the *Himiko* half-light radius (1.6 kpc) observed by [Ouchi et al. \(2009\)](#). Other properties of *Himiko* are poorly constrained. The SFR is highly uncertain and its value strongly depends on the diagnostics used to infer it: SED fitting gives $\gtrsim 34$ M $_{\odot}$ yr $^{-1}$, UV luminosities yields $= 25_{-12}^{+24}$ M $_{\odot}$ yr $^{-1}$; the Ly α line implies 36 ± 2 M $_{\odot}$ yr $^{-1}$. As for the metallicity, [Ouchi et al. \(2009\)](#) suggest $Z = [1 - 0.02] Z_{\odot}$ as a plausible range, i.e. consistent with the one we have chosen for our analysis. For a fair comparison with the Plateau de Bure Interferometer data by [Walter et al. \(2012b\)](#), we smooth our [C II] simulations to a beam resolution of $2.27'' \times 1.73''$, and we produce channel maps of 200 km s $^{-1}$ width. In [Fig. 4.3](#) we show the map with the largest signal achieved. We find that, for $Z = Z_{\odot}$ the maximum intensity is ~ 0.72 mJy km s $^{-1}$, slightly exceeding the observed upper limit by [Walter et al. \(2012b\)](#); thus, we can put a solid upper limit on *Himiko*'s metallicity $Z < Z_{\odot}$. This shows the potential of FIR lines in obtaining reliable metallicity measures in high- z galaxies.

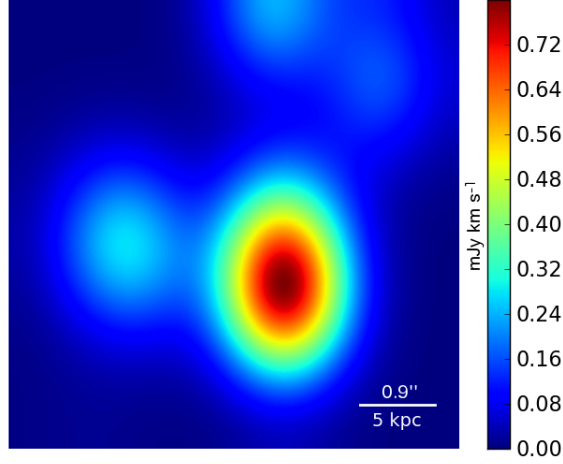


Figure 4.3: Synthetic map of [C II] emission in mJy km s^{-1} integrated over a velocity channel of width = 200 km s^{-1} , and smoothed to an angular resolution of $2.27'' \times 1.73''$ to allow comparison with [Walter et al. \(2012b\)](#) observations.

4.4.2 Low redshift observations

Haro 11 (H11), a nearby ($z \sim 0.02$) dwarf galaxy ([Cormier et al., 2012](#)), is considered a suitable local high- z galaxy analog (see Fig. 1.4 in the first Chapter). Through Herschel-PACS observations of the [C II], [O I] and [N II] lines, [Cormier et al. \(2012\)](#) measured a size of $\sim 3.9 \text{ kpc}$ for the H11 star forming region, a value which is comparable to the size of the clump A shown in the upper-most right panel in Fig. 4.2. These authors also estimate the relative contribution to the observed FIR lines from the diffuse (neutral/ionized) medium and PDRs. They found that $\sim 80\%$ of the [C II] and [N II] emissions come from the diffuse medium, while the [O I] mostly originates from PDRs. We scale the luminosities of the predicted FIR emission lines to the H11 luminosity distance ($D_L \sim 88$) and metal abundances ([Cormier et al., 2012](#)). For a fair comparison with the data, taken from Tab. 2 of ([Cormier et al., 2012](#)), we compute [C II], [O I], and [N II] spectra by integrating over a region of $\sim 12 \text{ kpc}$ in diameter, which corresponds to an angular size of $30''$ at the H11 redshift. For [C II] and [N II] lines our model predicts a flux corresponding to 20% of the observed one. For what concerns [O I], we recover only 3% of the observed flux. However, we recall that the contribution of PDRs, not included in our model, might be non-negligible.

	Integrated flux [mJy km s ⁻¹]	
	$Z = Z_{\odot}$	$Z = 0.02 Z_{\odot}$
[C II]	185	0.2
[O I]	30	0.1
[N II]	2	0.04

Table 4.1: Integrated flux over 500 km s⁻¹ channel, arising from our simulated source for $Z = Z_{\odot}$ and $Z = 0.02 Z_{\odot}$.

4.5 ALMA predictions

In Table 4.1, we plot the expected total fluxes for the FIR emission lines considered, varying the metallicity between Z_{\odot} and $0.02 Z_{\odot}$. In the solar metallicity case a [C II] $\sim 5\sigma$ detection over four 25 km s⁻¹ channels requires a sensitivity of 0.2 mJy, which translates into an observing time of $t_{\text{ON}} = 1.9$ h with the ALMA full array. We note that the predicted fluxes are sensitive to the actual value of Z , implying that a [C II] line detection can strongly constrain LAE metallicities. On the other hand, this implies that LAEs characterized by metallicities $Z < 0.5 Z_{\odot}$ would require a long observing time ($t_{\text{ON}} > 7.7$ h) to be detected even with the ALMA full array.

4.6 Summary

In this Chapter we outlined the second part of the work developed as a part of this Thesis. The research concerns the prediction of the intensity of several FIR emission lines ([C II] 158 μm , [O I] 63 μm , and [N II] 122 μm) arising from the ISM of high- z star forming galaxies. We combined RT simulations of a $z = 6.6$ galaxy with a sub-grid multi-phase model to predict the density and temperature of the cold and warm neutral phase of the diffuse ISM. Hereby we summarize the main results and caveats of the model:

- We find that warm neutral medium lies in overdense regions located sufficiently far from the central star forming clump where the strong ionizing UV field does not allow the presence of neutral gas. Cold gas resides instead in more dense clumps. The physical properties of the cold and warm neutral medium deduced here are in agreement with previous studies (e.g. [Wolfire et al., 1995, 2003](#)): the mean density (temperature) of the CNM (WNM) gas

are $\langle n_{\text{CNM}} \rangle = 50 \text{ cm}^{-3}$, $\langle T_{\text{CNM}} \rangle = 250 \text{ K}$, and $\langle n_{\text{WNM}} \rangle = 1.0 \text{ cm}^{-3}$, $\langle T_{\text{WNM}} \rangle = 5000 \text{ K}$, respectively.

- Assuming $Z = Z_{\odot}$, our model predicts for the [C II] line a flux of $185 \text{ mJy km s}^{-1}$, integrating over $\sim 500 \text{ km s}^{-1}$. The [O I] and [N II] fluxes are ~ 6 and ~ 90 times lower than the [C II] one, respectively. We have investigated also the case of $Z = 0.02 Z_{\odot}$. At this metallicity, the [C II] and [O I] intensities drop by a factor of ~ 1000 and ~ 300 , respectively, while the [N II] flux is reduced by a factor of 50.
- In the case of $Z = Z_{\odot}$, we have found that 95% (75%) of the [C II] ([O I]) emission arises from the cold neutral medium of the ISM, and the remaining 5% (25%) from the warm neutral phase. In the lower metallicity case, the fluxes of the [C II] and [O I] emission lines drop abruptly since the lower metal content does not allow the presence of CNM phase. As a caveat we note that the [O I] $63 \text{ m}\mu$ line could be optically thick (e.g. [Vasta et al., 2010](#)). The intensity of the [N II] line, instead, scales linearly with the metallicity, since it arises from the ionized medium.
- According to our findings, the [C II] emission line is detectable with the ALMA full array in $1.9 < t_{\text{ON}} < 7.7 \text{ hr}$ in star forming, high- z galaxies with $Z_{\odot} > Z > 0.5 Z_{\odot}$. We emphasize again that our predictions provide a solid lower limit to the expected FIR emission lines flux.
- The results achieved with this model might be very useful to FIR line intensity mapping studies. In fact, our model represents a valid tool to calibrate the intensity of these lines depending on the different properties of the first galaxies, such as the metallicity and the SFR. Since the mass of the CNM increases in weaker FUV radiation field environments, it is likely that the specific emission from FIR emission lines as the [C II] and [O I] could increase towards fainter galaxies.
- We have compared our predictions with observations of FIR emission lines in high- z and local star forming galaxies. At $Z = Z_{\odot}$, our model slightly exceeds the $1\sigma = 0.7 \text{ mJy km s}^{-1}$ upper limit on the [C II] intensity found in *Himiko* through PdBI observations ([Walter et al., 2012b](#)). This result suggests that the gas metallicity in this source must be sub-solar. Our results are also

marginally consistent with [C II], [O I], and [N II] observations of Haro 11 (Cormier et al., 2012), a suitable high- z galaxy analog in the Local Universe. In this case, our model predicts a flux which is $\sim 20\%$ ($\sim 3\%$) of the observed one in the case of [C II] and [N II] ([O I]) emissions.

- We underestimate the observed line luminosity in Haro11 as a non-negligible fraction of their flux may be provided by dense PDRs not included yet in our study. In particular the [O I] line is expected to originate primarily from PDRs (Cormier et al., 2012).

We now discuss in some details the main caveats of the work presented in this Chapter. As clearly stated before, an interesting result of our model is that the [C II] and [O I] lines are shifted with respect to the [N II] line. This is the consequence of the fact that they originate from different regions: while the ionized medium, which is traced by the [N II] line, is located close to the center of the galaxy, the neutral gas, in which the [C II] and [O I] lines are excited, is predominantly located at large galactocentric radii. This result can explain the marginal shift between the [C II] and [N II] lines observed by Nagao et al. (2012) in some high- z galaxies. However, as mentioned in the previous Sections, our sub-grid model does not include the contribution from the photodissociation regions (see Sec. 2.3 for the discussion about the physics of PDRs). This might change the final outcomes of the model because the PDRs are expected to be located near the regions in which stars form, i.e. at the center of the galaxy as clearly shown in the upper left panel of Fig. 4.1.

FIR line emission from PDRs 5

IN WHAT follows we present the further developments implemented into the model described in Chapter 4. We will explain the physically motivated prescriptions adopted to locate the molecular clouds within our simulated galaxy. This allows to compute the contribution of the photodissociation regions to FIR emission lines. We focus our attention on the observability of molecular tracers (such as CO rotational transitions) that were not provided by the model outlined in Chapter 4. While we refer the reader to that Chapter for an overview of the high- z observations of FIR metal cooling lines before the ALMA advent, we clarify that similar results are obtained in the case of molecular tracers as the CO rotational transitions. As for atomic lines, CO detections at $z > 6$ are limited to quasars/AGNs hosts and sub-millimeter galaxies (e.g. Bertoldi et al., 2003; Combes et al., 2012; Walter et al., 2012a; Wang et al., 2013; Riechers et al., 2013).

As pointed out before, first attempts to predict FIR line emission from high- z galaxies was performed by Nagamine et al. (2006), who computed the [C II] luminosity function based on a SPH simulation coupled with a sub-grid multi-phase model of the ISM. Other studies that model the CO signal arising from high- z galaxies have been carried out by Greve & Sommer-Larsen (2008) that simulate Lyman Break Galaxies (LBGs) at $z = 3$ and, more recently, by Muñoz & Furlanetto (2013) that explore the molecular cloud properties and the physics of CO transitions in $z > 6$ LBGs. Both studies conclude that even with ALMA the detection of these transitions would require very long observing times.

The Chapter is organized as follows: in Sec. 5.1 we recap the main features of diffuse neutral medium model and we describe how we implement its sub-grid

physics on top of the cosmological simulation. In Sec. 5.2 we discuss how we locate the MCs inside the galaxies and we compute the FIR line emission arising from them. The last Section is focused on the CO observability while we defer to the next chapter the global discussion about the relative contribution of PDRs and diffuse neutral gas to the [C II] luminosity.

5.1 The diffuse neutral medium

The interstellar medium is a very complex environment constituted by a different gas phases (neutral/ionized diffuse medium and clumpy molecular) whose properties are controlled by the continuous interplay between radiative and dynamical processes. Several works have been devoted to study the ISM physics, to investigate the equilibrium states reached by balancing the heating and cooling processes, and to follow the growth of instabilities in the molecular component of the ISM (e.g. McKee & Ostriker, 1977; Wolfire et al., 1995; Padoan, 1995; Wolfire et al., 2003). The properties of the ISM can also be investigated through numerical simulations. In this kind of studies, the major difficulty concerns the large dynamical range required to catch both the cosmological evolution of galaxies on \sim kpc scales and the ISM physics on \sim pc scales.

We run cosmological SPH hydrodynamic simulations using GADGET-2 (Springel, 2005). We simulate a $(10h^{-1}\text{Mpc})^3$ comoving volume with 2×512^3 baryonic+dark matter particles, giving a mass resolution of $1.32 (6.68) \times 10^5 M_\odot$ for baryons (dark matter). We select a snapshot at redshift $z = 6.6$, and we identify the most massive halo (total mass $M_h = 1.17 \times 10^{11} M_\odot$, $r_{vir} \approx 20$ kpc) by using a Friend-of-Friend algorithm. We select a $(0.625 h^{-1}\text{Mpc})^3$ comoving volume around the center of the halo, and post-processed UV radiative transfer (RT) using LICORICE (Baek et al., 2009). LICORICE uses a Monte Carlo ray-tracing scheme on an adaptive grid. RT calculations are performed until equilibrium between photoionizations and recombinations is achieved; this occurs within ≈ 10 Myr. We interpolate all gas physical properties around the halo center on a fixed 512^3 grid using the SPH kernel and smoothing length, within a $(0.156 h^{-1}\text{Mpc})^3$ comoving volume. We achieve a higher resolution (~ 60 pc) by interpolating on a finer grid as shown in Fig. 6 of (Baek et al., 2012). We then compute the FUV flux in the Habing (6 – 13.6 eV) band (G_0) as in Eq. 4.2. For an extended description of the simulation we defer the interested

reader to Sec. 4.1.

With current computational resources it is not possible to self-consistently include sub-kpc scale physics in the RT simulations described above. We implement on top of the simulation a sub-grid model which takes into account the cooling and heating processes that take place in the neutral ISM.

As extensively discussed in [Wolfire et al. \(1995, 2003\)](#), the balance between cooling and heating processes results into a two-phase gas in which a cold neutral medium is in pressure equilibrium with a warm neutral one. The relative abundance of the CNM and WNM both depends on the gas metallicity, that determines the amount of metals and dust, and on G_0 , that controls the rates of photoelectric effect and recombination on dust grains.

While we refer to the the previous Chapter for a thorough description of the sub-grid model for the diffuse ISM, for sake of completeness, we recall below the most relevant results obtained.

The WNM distribution closely traces regions of high column density ($N_H \approx 10^{22} \text{ cm}^{-2}$) that are far enough from the central star forming region not to get ionized. The CNM lies instead only in small ($D \leq 2 \text{ kpc}$) overdense clumps at the periphery of the galaxy. We find that the mean CNM density (temperature) is $\langle n_{\text{CNM}} \rangle = 50 \text{ cm}^{-3}$ ($\langle T_{\text{CNM}} \rangle = 250 \text{ K}$), while for the WNM we obtain $\langle n_{\text{WNM}} \rangle = 1.0 \text{ cm}^{-3}$ ($\langle T_{\text{WNM}} \rangle = 5000 \text{ K}$).

5.1.1 Metallicity

The model outlined in Chapter 4 assumes that metals are uniformly distributed within the galaxy. Hereafter, we refer to models with a uniform metallicity distribution as¹ “C-models”. In this work, we also consider the possibility that the distribution of metals follows the density distribution, by relating Z to the baryonic overdensity of each cell $\Delta \equiv \rho_{gas}/\rho_c(z)$, where ρ_{gas} is the gas density in the cell and $\rho_c(z)$ is the critical density at redshift z (Eq. 1.1). This is in agreement with the parametrization adopted by [Keating et al. \(2014\)](#) to describe the circumgalactic medium of high- z galaxies, and with the results presented by [Pallottini et al. \(2014\)](#). By using state-of-the-art cosmological simulations to investigate the metal enrich-

¹We call C01 a model in which a uniform $Z = 0.1 Z_\odot$ is imposed.

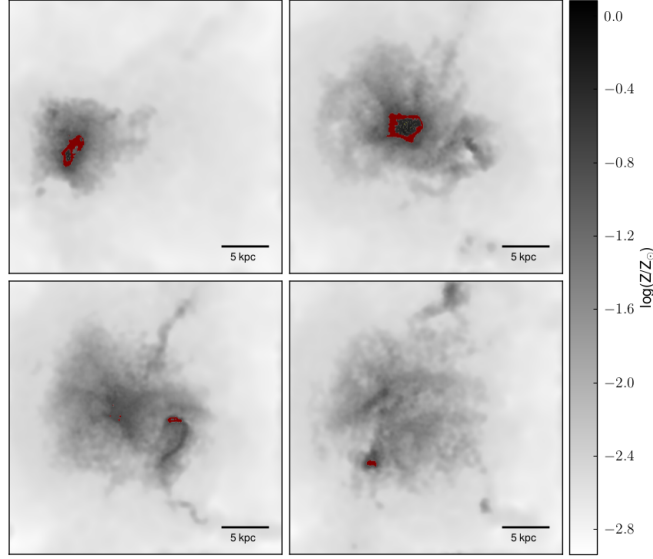


Figure 5.1: Slices of thickness 57 pc cut through the simulated galaxy for the P005 model showing the metallicity distribution (gray scale) and molecular clouds (red regions). Note that the metallicity of the overdense regions in which MCs reside is larger than the mean value $\langle Z \rangle = 0.05 Z_{\odot}$.

ment of high- z galaxies, Pallottini et al. (2014) found a tight correlation between Z and Δ for $\log \Delta \gtrsim 2$, namely for overdensities typical of galaxy outskirts/ISM. While in the IGM ($\log \Delta \leq 2.3$) the metallicity is only weakly correlated with Δ , in the ISM ($2.3 < \log \Delta < 4.5$) the $Z - \Delta$ relation is tight. This is due to the fact that the most overdense regions denote the location in which stars form, and that are therefore more efficiently polluted with metals. We fit the $Z - \Delta$ relation provided in their paper and we normalize the relation to the mean metallicity $\langle Z \rangle$ over the galaxy, i.e. over those cells which overdensity is $\Delta > 200$. Hereafter, we refer to models that take into account this $Z - \Delta$ relation as² “P-models”. In Fig. 5.1, we show four 57 pc-thick slices of the simulated box showing the metallicity distribution (gray scale) and molecular clouds (red regions) for the P005 model. We point out that molecular cells reside in highly overdense regions where metallicity largely exceeds the mean, i.e. $Z_{\text{MCs}} > \langle Z \rangle \approx 0.05 Z_{\odot}$. This implies that any line arising predominantly from the PDRs would provide an upper limit on the mean metallicity of the galaxy.

²We call P005 a density-dependent metallicity case with $\langle Z \rangle = 0.05 Z_{\odot}$.

5.2 Including the molecular clouds

Beside the emission produced in the neutral diffuse medium treated in the previous Chapter, FIR lines can be excited in the photodissociation regions (Tielens & Hollenbach, 1985; Hollenbach & Tielens, 1999) around molecular clouds. PDRs consist of neutral and molecular gas whose chemical and physical properties are controlled by the FUV photons that heat the gas through photoelectric emission from grain surfaces and polycyclic aromatic hydrocarbons (PAHs), and by collisional de-excitation of vibrationally excited H_2 molecules (see Sec. 2.3 for a complete discussion). As extensively discussed in Sec. 2.2, H_2 is either necessary to cool the gas and as it is a fundamental component of MCs that are the environments in which stars form via the growth of instabilities (e.g. McKee & Ostriker, 2007; Kennicutt & Evans, 2012; Padoan et al., 2013, and references therein), that provide the FUV photons, form.

To establish whether the gas in a cell becomes gravitationally bound, we apply the Jeans instability criterium. We define *molecular cells* those satisfying the following condition: $M_{cell} > M_J(T_{\text{CMB}}, n_{cell})$, where M_{cell} is the mass of the gas in the cell, M_J is the Jeans mass at the CMB temperature (T_{CMB}) at $z = 6.6$, and at the density of the gas in the simulation cell (n_{cell}). By applying this prescription, we find that the total mass of molecular hydrogen in the simulated galaxy is $M_{\text{H}_2} = 3.9 \times 10^8 M_\odot$, consistently with previous theoretical estimates ($M_{\text{H}_2} = 2.5 \times 10^8 M_\odot$, Vallini et al., 2012) and observational constraints ($M_{\text{H}_2} < 4.9 \times 10^9 M_\odot$, Wagg et al., 2009) on $z \approx 7$ LAEs.

Since we find that on average the simulation cells contain a molecular hydrogen mass $\langle M_{\text{H}_2}^{cell} \rangle \sim 3 \times 10^3 M_\odot$, we consider each molecular cell as a Giant Molecular Cloud (GMC; $M_{\text{GMC}} = 10^3 - 10^6 M_\odot$, Murray, 2011). The properties of GMCs are controlled by a turbulent and highly supersonic velocity field that causes isothermal shock waves (Padoan, 1995; Ostriker et al., 2001; Padoan et al., 2013). The problem of turbulent fragmentation of molecular clouds can be treated analytically (e.g. Krumholz & McKee, 2005; Padoan & Nordlund, 2011; Hennebelle & Chabrier, 2011, 2013) or numerically (e.g. Vazquez-Semadeni, 1994; Kim & Ostriker, 2002; Kim et al., 2003; Wada, 2008; Tasker & Tan, 2009). Analytical models as well as numerical simulations show that the distribution of the gas density (n_{cl}) in an isothermal, non self-gravitating, turbulent medium follows a log-normal distribution

(Padoan, 1995; Padoan & Nordlund, 2011):

$$p(\ln x)d \ln x = \frac{1}{(2\pi\sigma^2)^{1/2}} \exp \left[-\frac{1}{2} \left(\frac{\ln x - \overline{\ln x}}{\sigma} \right)^2 \right], \quad (5.1)$$

where $x = n_{cl}/\overline{n_{cl}}$, $\overline{n_{cl}} \simeq n_0 \mathcal{M}^2$, n_0 is the average number density of the CNM ($n_0 = 50 \text{ cm}^{-3}$, see Chapter 4), $\mathcal{M} = 10$ is the Mach number value suggested by Kainulainen & Tan (2013), the turbulent velocity dispersion is given by $\sigma = \sqrt{\ln[1 + (\mathcal{M}\beta^2)]}$ with $\beta = 0.5$ and $\overline{\ln x} = -0.5\sigma^2$. If we assume that each GMC in our simulation is composed by a set of clumps, we can compute the densities n_{cl} of each clump by adopting an iterative approach that consists of the following steps:

1. Select n_{cl} by sampling the density distribution (Eq. 5.1).
2. Set the clump radius equal to the Jeans length $r_{cl} = \lambda_J(T_{CMB}, n_{cl})$.
3. Calculate the clump mass $M_{cl} = (8\pi/3)m_H n_{cl} r_{cl}^3$.
4. If $M_{cl} < M_{cell}$ calculate the residual mass in the cell $M_{cel}^{new} = M_{cell} - M_{cl}$; go to step 1.
5. If $M_{cl} > M_{cell}$ reject the density sampled and assume $M_{cl} = M_{cell}$. Calculate r_{cl} as in step 2. and use it to derive the resulting clump density.

Through this procedure, we find that the MCs in the simulations are characterized by the following properties: $\langle \log n_{cl} \rangle = 2.9 \pm 0.4 \text{ cm}^{-3}$, $\langle M_{cl} \rangle = 50 \pm 20 M_\odot$ and radius $\langle r_{cl} \rangle = 0.7 \pm 0.3 \text{ pc}$. In Fig. 5.2 we present the Probability Distribution Function (PDF) and Cumulative Distribution Function (CDF) for the densities, masses and radii of the resulting clumps.

5.3 Far infrared line emission

In this Section, we describe how we compute the FIR lines emissivity from PDRs. The emission is related to the temperature and the density of the gas, to the flux of the FUV dissociating field and to the metallicity Z .

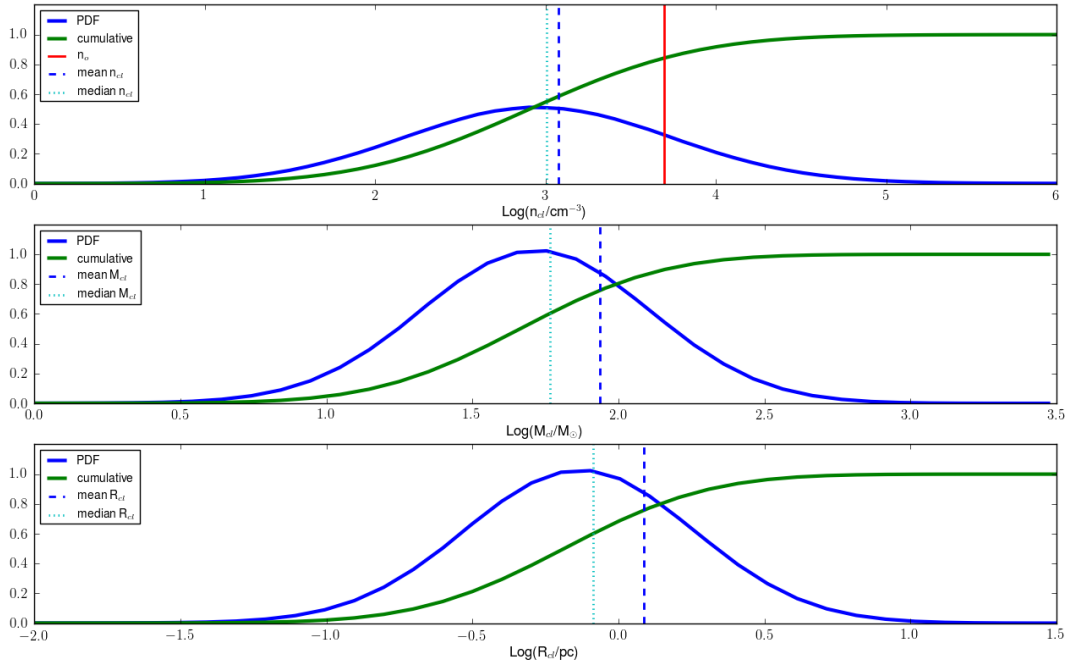


Figure 5.2: *Upper panel:* Probability Distribution function (blue solid line) and Cumulative Distribution Function (green solid line) of the clump number density n_{cl} . The red solid line indicates the typical clump density \bar{n}_{cl} . We show also the mean density (dashed line) weighted over the mass of the clumps, and the median of the density (dotted line). *Middle panel:* PDF, CFD, mean and median of the mass distribution of the clumps M_{cl} . *Lower panels:* PDF, CFD, mean and median of the radius of the clumps radius.

5.3.1 Coupling the simulation with UCL_PDR

Several theoretical models have been developed to calculate the emissivity of FIR lines and interpret the observations at sub-millimeter and millimeter wavelengths. These studies have evolved into numerical codes that account for a growing number of physical effects with increasing accuracy (e.g. Röllig et al., 2007, for a comparison among them). In this work we couple our simulation with UCL_PDR (Bell et al., 2005, 2007; Bayet et al., 2009) a PDR code that allows to achieve the emissivity of various lines, given the density of the gas in the photodissociation region (n), the intensity of the FUV radiation field (G_0), and the metallicity (Z).

More precisely, UCL_PDR is a time-dependent model which treats the MCs as one-dimensional, semi-infinite slabs illuminated from one side by FUV photons. The physical processes included in the code are: (i) H₂ formation on dust grain surfaces, (ii) H₂ photodissociation by FUV radiation (iii) H₂ UV fluorescence, (iv) the photoelectric effect from silicate grains and polycyclic aromatic hydrocarbons (PAHs),

(v) [C II] recombination and (vi) interaction of low-energy cosmic-rays (CRs) with the gas, which boosts the temperature of the gas. As input parameters we consider the density of the clumps that results from the procedure described in Sec. 5.2, G_0 computed as in Eq. 4.2, and the metallicity achieved according to the Z - Δ relation discussed in Sec. 5.1.1.

The outputs of UCL_PDR provides the surface brightness of various metal and molecular cooling lines at different radii inside the cloud. In Fig. 5.3 we show the [C II] surface brightness (S_{CII}) in $\text{erg cm}^{-2} \text{s}^{-1} \text{sr}^{-1}$, for different gas number densities $\text{Log}(n) = [5.5, 4.5, 3.5, 2.5]$ at 1 pc from the cloud surface, i.e. the mean value of the clump radii resulting from the sampling of the lognormal distribution (see Fig. 5.2). Our aim is to study the correlation between S_{CII} and the gas properties (Z , G_0 , and n) that control this quantity. For $n = 10^{5.5} \text{cm}^{-3}$ (upper left panel), S_{CII} ranges from $\sim [10^{-5.5} - 10^{-3.5}]$ for $G_0 = [10^{1.5} - 10^{3.5}]$ respectively and it is almost completely independent on the metallicity. On the other hand, for $n = 10^{2.5} \text{cm}^{-3}$ (lower right panel), $S_{\text{CII}} \sim [10^{-7.0} - 10^{-4.0}]$ for $Z = [10^{-2.5}, 10^{0.5}]$ and it is uncorrelated with the intensity of the dissociating field. In the intermediate density regime the [C II] surface brightness correlates both with G_0 and Z .

We explain this behavior considering that at high density the number of photons that penetrate and ionize the carbon is highly affected by the density of the gas. Therefore the higher is G_0 , the higher is the [C II] abundance and therefore the emission is shaped almost only by this parameter. On the contrary, for low gas densities the carbon is completely ionized for every value of G_0 and therefore the parameter that predominantly affects the brightness is the metallicity. Indeed, the higher is Z (namely the [C II] abundance), the higher is the brightness of the line. In Fig. 5.4 we show the ratio between [O I] and the [C II] brightnesses at 1 pc from the cloud surface as a function of Z , G_0 and for different values of the gas metallicity.

For $n = 10^{[5.5, 4.5, 3.5]}$ the ratio is almost completely independent on the metallicity and it is positively correlated with G_0 . The [O I] emission arising from PDRs always exceeds the [C II] one, except than in low dense regions ($n < 10^{3.5}$), irradiated by a feeble radiation field ($G_0 < 10^2$). Finally, in Fig. 5.5 we plot the ratios (R_{CO}) between the CO(6-5) and the [C II] brightness as a function of the gas metallicity Z and of the intensity of the FUV dissociating field G_0 . Except in the case of very dense MCs ($n = 10^{5.5}$), the [C II] emission from PDRs largely always exceeds the CO(6-5) one.

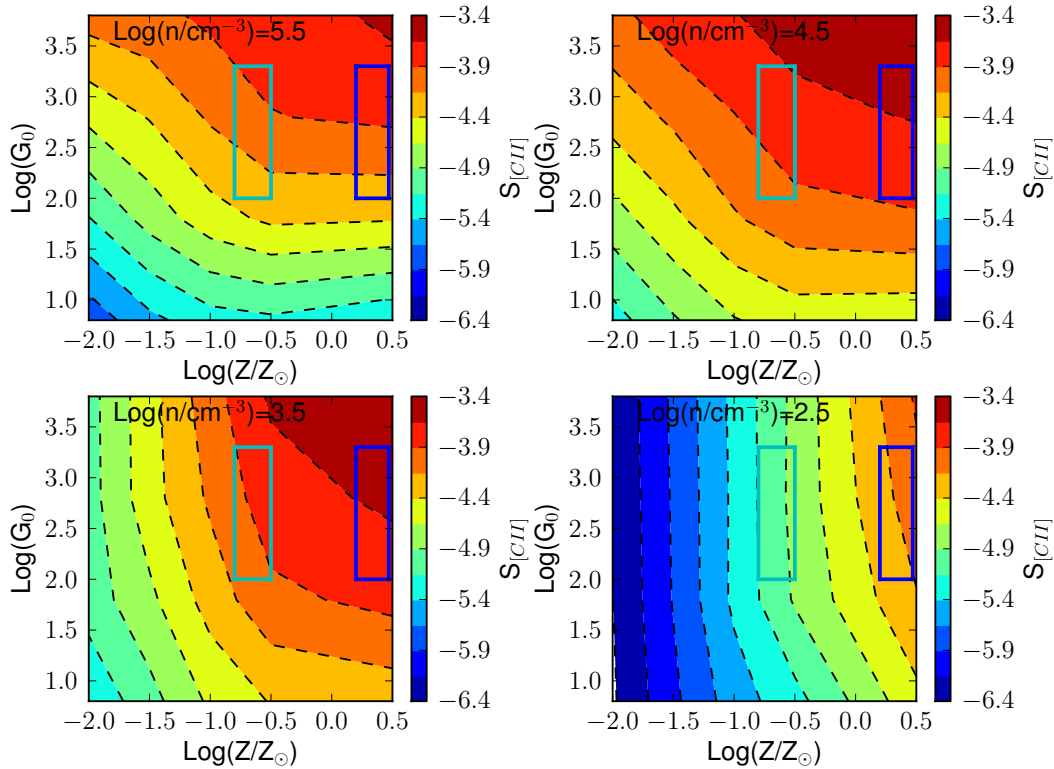


Figure 5.3: [C II] brightness S_{CII} in $\text{erg cm}^{-2} \text{s}^{-1} \text{sr}^{-1}$, as a function of the gas metallicity Z and of the intensity of the FUV dissociating field G_0 . The brightness is calculated at $r = 1$ pc inside the cloud at a fixed volume density for the gas: $\text{Log}(n) = [5.5, 4.5, 3.5, 2.5]$. The rectangles over plotted on the contours indicate the ranges of Z and G_0 inside which we find the bulk of MCs for $\langle Z \rangle = 0.5 Z_\odot$ (blue line) and $\langle Z \rangle = 0.05 Z_\odot$ (cyan).

5.4 The CO(6–5) emission

In this Section, we discuss our results concerning the luminosity of the CO(6–5) rotational transition of carbon monoxide. CO molecules are present where the gas is sufficiently shielded from the FUV dissociating field. Therefore, the emission arises only from the central part of the galaxy corresponding to the location of molecular clouds. Actually, the higher is the rotational quantum number J associated to the CO transition, the denser and the warmer has to be the gas to allow the excitation of the line. Therefore high- J CO lines, tracing dense clumps inside MCs, are more closely connected with the stars in formation (Bayet et al., 2009). The choice of the $J = 6 \rightarrow 5$ rotational transition is due to the fact that at $z \sim 6.6$ it is the lower J transition observable with ALMA. Indeed, CO(6–5) has a rest frequency $\nu_{rest} = 691.627$ GHz and, therefore, is redshifted at $\nu_{obs} = 91.003$ GHz

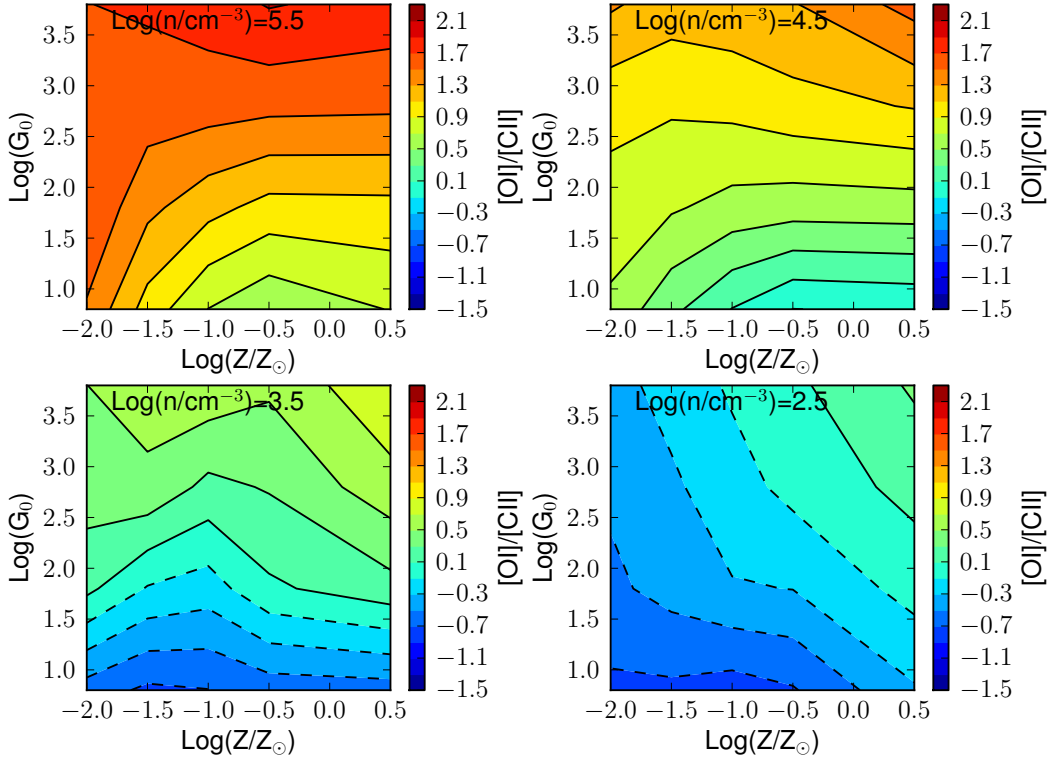


Figure 5.4: Ratio between [O I] and [C II] brightness, in logarithmic scale, as a function of the gas metallicity Z and of the intensity of the FUV dissociating field G_0 . The brightnesses are calculated at $r = 1$ pc inside the cloud at a fixed volume density for the gas: $\text{Log}(n) = [5.5, 4.5, 3.5, 2.5]$.

into the ALMA BAND 3. The CO(6–5) spectrum for $\langle Z \rangle = [0.5, 0.2, 0.05] Z_\odot$ is shown in yellow, orange, and pink respectively, in the left panel in Fig. 5.6. It peaks at $F_{peak} \sim [37, 5, 1] \mu\text{Jy}$ and the FWHM $\sim 50 \text{ km s}^{-1}$ remains constant. The integrated flux for $Z = 0.5 Z_\odot$ is $F_{\text{CO}} \simeq 2.1 \text{ mJy km s}^{-1}$. This value is in good agreement with what found by Muñoz & Furlanetto (2013) for a galaxy with an halo mass of $M_h = 10^{11} M_\odot$ and assuming $Z = 0.3 Z_\odot$ for which they predict $F_{\text{CO}} \lesssim 6 \text{ mJy km s}^{-1}$. In the right panel of Fig. 5.6 is shown the map of the CO(6–5) emission from PDRs in mJy km s^{-1} for $\langle Z \rangle = 0.5 Z_\odot$. The emission is integrated over the entire cube.

In Fig. 5.7 we present the CO Spectral Line Energy Distribution (SLED) achieved assuming $\langle Z \rangle = 0.5 Z_\odot$. We fit our results by considering the LTE model proposed by Obreschkow et al. (2009). The LTE model is given as a function of two parameters: the excitation temperature T_e and the optical depth of each line τ_J . Best fit

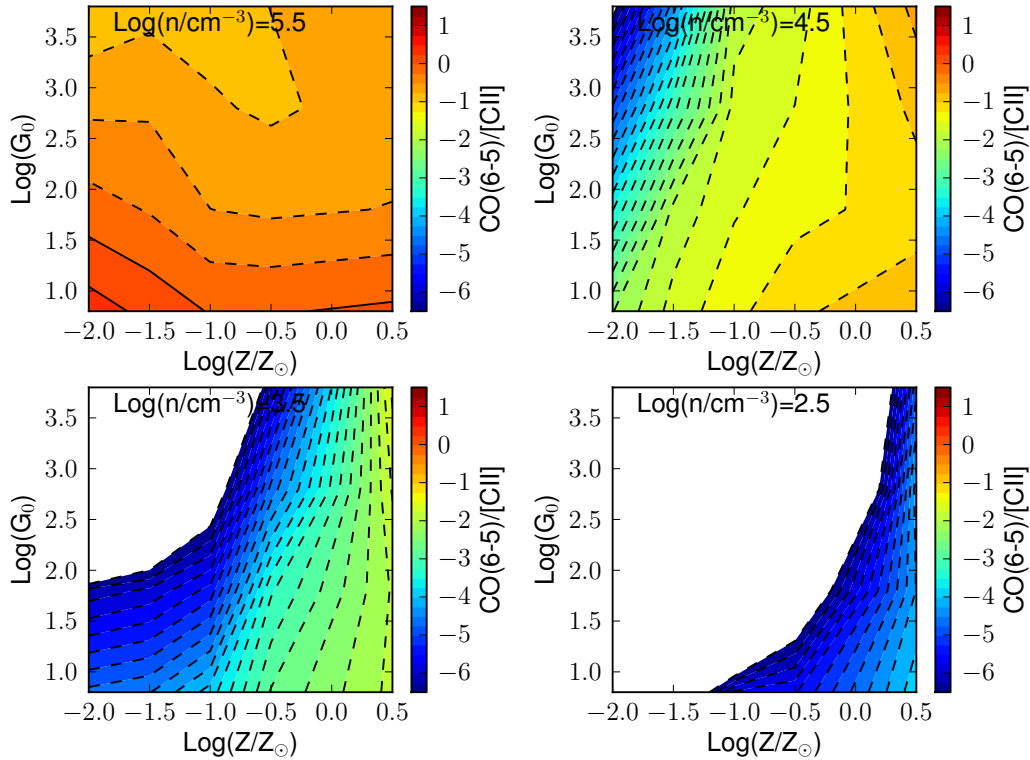


Figure 5.5: Ratio between CO(6-5) and [C II] brightness, in logarithmic scale, as a function of the gas metallicity Z and of the intensity of the FUV dissociating field G_0 . The brightnesses are calculated at $r = 1$ pc inside the cloud at a fixed volume density for the gas: $\text{Log}(n) = [5.5, 4.5, 3.5, 2.5]$. Ratios below 10^{-6} are not shown in the plots.

parameters are $T_e = 38$ K and $\tau_J = 10^{-4}$. Yellow and blue regions represent the $\pm 10\%$ uncertainties on the simulated values and on the fit respectively. We point out that the LTE model is able to reproduce the low- J lines while for $J > 6$ the LTE slightly fails.

The CO(1-0) luminosity along with the mass of molecular hydrogen (see Sec. 5.2) allows to calculate the expected conversion factor:

$$\alpha_{\text{CO}} = \frac{M_{\text{H}_2}}{L_{\text{CO}(1-0)}} = 2 \text{ M}_{\odot} / [\text{K km s}^{-1} \text{ pc}^2] \quad (5.2)$$

Our result is consistent with the picture that has emerged in recent years according to which massive merger-driven starbursts such as SMGs are characterized by $\alpha_{\text{CO}} < 1$ similar to that of local ULIRGs, while NSFGs have higher α_{CO} , similar to that of our own Galaxy (Narayanan et al., 2012; Bolatto et al., 2013).

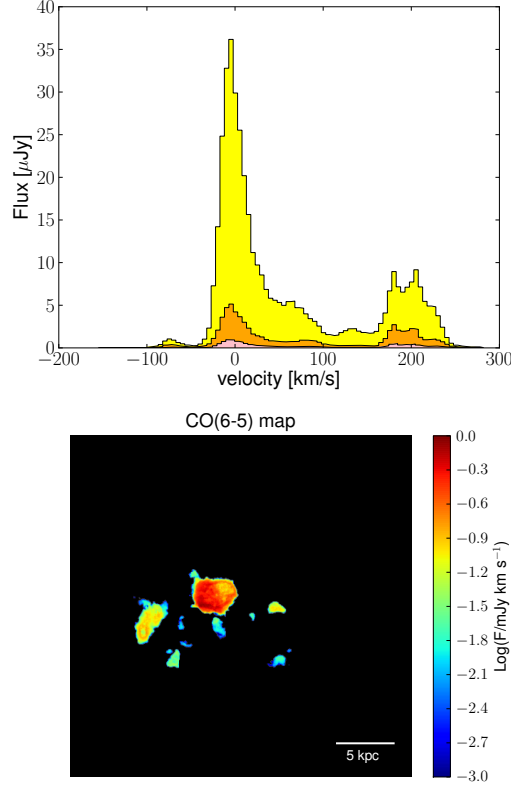


Figure 5.6: *Left panel:* CO(6–5) spectrum rebinned in 5 km s^{-1} for different metallicities: $\langle Z \rangle = 0.5 Z_{\odot}$ yellow, $\langle Z \rangle = 0.2 Z_{\odot}$ orange, and $\langle Z \rangle = 0.05 Z_{\odot}$ pink. *Right panel:* Map of the CO(6–5) emission from PDRs in mJy km s^{-1} for $\langle Z \rangle = 0.5 Z_{\odot}$. The emission is integrated over the entire cube.

5.5 Summary and conclusions

Through this Chapter we have outlined the method developed during the Thesis to calculate the emission of several far-infrared lines ([C II], [O I] and CO(6–5)) arising either from the diffuse gas and from PDRs of a $z \sim 6.6$ galaxy. We have first combined state-of-the-art radiative transfer simulations with a sub-grid model that allows us to estimate the emission from the diffuse neutral medium. Moreover, to take into account the emission from the photodissociation regions in the vicinity of the molecular clouds, we have adopted the Jeans instability criterium to search for the sites in which the MCs form. Hereby we summarize the main achievements:

- We find that the mass of molecular hydrogen that fuels the star formation in our simulated galaxy is $M_{\text{H}_2} = 3.9 \times 10^8 M_{\odot}$. The molecular clouds are

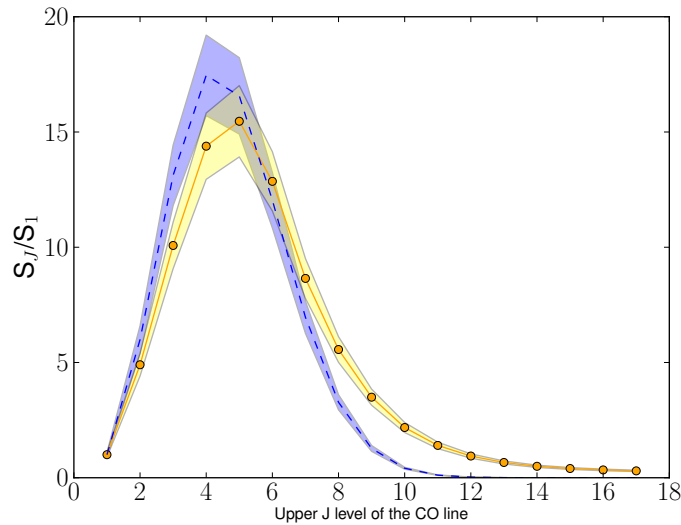


Figure 5.7: CO spectral line energy distribution. The integrated flux density of each line (S_J) in mJy km s^{-1} is scaled to the value of the CO(1–0) transition. In yellow the resulting values from our simulation. In blue the best fit achieved by applying the LTE model by [Obreschkow et al. \(2009\)](#). Yellow and blue regions represent the 10% uncertainties on the simulated values and on the fit respectively.

predominantly located in the center of the galaxy, in the most over dense regions.

- We describe their highly non-linear density structure according to the log-normal distribution resulting from the turbulence in the ISM. Our model predicts that MCs are constituted by dense ($n_{\text{MC}} \sim 10^2 - 10^4 \text{ cm}^{-3}$) and small ($r_{\text{MC}} \sim \text{pc}$) clumps, whose masses are on average $\langle M_{cl} \rangle = 90 M_{\odot}$.
- To distribute metals in the simulated galaxy we exploit the correlation between Z and the overdensity Δ found by [Pallottini et al. \(2014\)](#). The natural consequence of the Z - Δ relation is that regions where MCs are located (i.e. the most over dense in the simulation) are more metal enriched than the rest of the galaxy.
- The important implication of this result is that, since $Z_{\text{MCs}} > \langle Z \rangle$, metallicity measurements through FIR lines that trace PDRs deliver upper limits on the average metallicity of the galaxy. The emission from PDRs is achieved by coupling our simulation with UCL_PDR, a numerical code that provide self consistently the emissivity of various FIR lines as a function of the gas density,

the FUV flux (G_0), and the metallicity (Z).

- The predicted intensity of the CO(6–5) line is consistent with a CO-to-H₂ conversion factor $\alpha \simeq 2 M_{\odot}/[\text{K km s}^{-1} \text{ pc}^2]$ and the integrated flux ($\sim 2.5 \text{ mJy km s}^{-1}$) is in agreement with the predictions provided by [Muñoz & Furlanetto \(2013\)](#). CO lines from normal star forming galaxies at the Epoch of Reionization.
- The detection of CO lines from these galaxies is expected to be barely impossible even with ALMA.

We conclude this discussion by noticing that our study highlights the importance of the synergy between simulations and observations to interpret available data and to guide future observational campaigns. The next step, having now a complete model of FIR line emission from the ISM, is to explore the relation between the line luminosities and other parameters such as the SFR and the metallicity of the galaxies.

Having implemented either the emission from the diffuse gas and from the PDRs, we can now disentangle the relative contribution of various gas phases to the [C II] line luminosity that is expected to be the most promising (because the most luminous) FIR tracer of the high- z galaxies. We address these issues in the next Chapter.

The [C II]-SFR relation at high redshift 6

ALTHOUGH SEVERAL authors have searched for the [C II] line in normal star-forming galaxies (NSFGs; $\text{SFR} \approx 10 \text{ M}_{\odot} \text{ yr}^{-1}$) at $z > 6$ either with the PdBI (Walter et al., 2012b; Kanekar et al., 2013; González-López et al., 2014) and ALMA (Ouchi et al., 2013; Ota et al., 2014), no firm detection has been obtained so far. The current deepest upper limit on the [C II] luminosity ($L_{[\text{C II}]} < 2.8 \times 10^7 L_{\odot}$) has been claimed by Schaerer et al. (2015) in a $z = 6.8$ lensed Lyman Break Galaxy and it seems to be in contrast with the correlation between the intensity of the [C II] line and the SFR (hereafter [C II]-SFR relation) found in local galaxies. Such relation holds for a wide range of galaxy types, ranging from metal poor dwarf galaxies, to starbursts, ultra-luminous infrared galaxies, and AGN hosting galaxies (Boselli et al., 2002; de Looze et al., 2011; Sargsyan et al., 2012; De Looze et al., 2014; Pineda et al., 2014; Herrera-Camus et al., 2014). At a first approximation, in thermal equilibrium the intensity of the [C II] line should be proportional to the heating rate due to star formation activity (e.g. Kennicutt, 1998; Kennicutt & Evans, 2012; de Looze et al., 2011; Herrera-Camus et al., 2014).

However, the [C II] line can be collisionally excited in many different components of the ISM (cold diffuse neutral medium, high density photodissociation regions, ionized medium). The multiphase origin of the [C II] line implies that a correct interpretation of the [C II]-SFR relation must account for the relative contribution of the different ISM components to the total [C II] emission. Observational studies have found that, in the plane of the Galaxy, the [C II] emission is mostly associated with dense PDRs (Pineda et al., 2013). On the contrary, in low metallicity local dwarf galaxies (e.g. Haro 11, Cormier et al., 2012), nearby galaxies (e.g. M51 and

M31, Kramer et al., 2013; Parkin et al., 2013; Kapala et al., 2015) and the outskirts of the Milky Way (Langer et al., 2014) the PDR contribution can be as small as $\approx 10\%$. The [C II]-SFR relation in these cases is shallower than that of starburst galaxies (De Looze et al., 2014).

In order to better clarify the origin of these difficulties we make use of the model described in the previous Chapters with the aim to finally assess whether the [C II]-SFR relation holds at high- z , and what we can learn from deviations from this relation.

We remind the reader that the numerical simulation adopted in this work has been extensively presented in Sec. 4.1, while the sub-grid model describing the thermal equilibrium of the neutral diffuse gas in the ISM is fully explained in Sec. 4.2. The inclusion of the MCs and the coupling of the simulation with the PDR code are discussed in Sec. 5.2. Through this analysis we also assume either constant metallicity profiles within the simulated galaxy (referred as C models), and the $Z - \Delta$ relation by Pallottini et al. (2014) outlined in Sec. 5.1.1 (referred as P models). More precisely, we consider C models with $Z = [1, 0.2, 0.05] Z_{\odot}$ (C1, C02, C005 respectively), and a P model with a $\langle Z \rangle = 0.05 Z_{\odot}$ (P005).

6.1 Physics of the [C II] emission

Before going ahead with the calculation of the [C II] luminosity as a function of the SFR and of the metallicity profile, we clarify whether the CMB radiation may have some effect on the visibility of the line. While we refer the reader to Sect. 2.6.1 for the general treatment of the physics of radiative processes, in what follows we will focus our attention only on the $158 \mu\text{m}$ transition of the ionized carbon.

Let simplify the [C II] $158 \mu\text{m}$ transition as a 2-level process. From now on, the upper level ($^2P_{3/2}$) will be labeled with u while the lower one ($^2P_{1/2}$) with l . The ratio of the level population can be found by solving the statistical balance equation:

$$\frac{n_u}{n_l} = \frac{B_{lu}I_{\nu} + n_e C_{lu}^e + n_H C_{lu}^H}{B_{ul}I_{\nu} + A_{ul} + n_e C_{ul}^e + n_H C_{ul}^H} \quad (6.1)$$

where the transition $l \rightarrow u$ is excited by collisions with electrons or protons and

by radiative excitation due to an external radiation field with intensity I_ν . The downwards transition $u \rightarrow l$ is instead produced by stimulate and spontaneous emission, and by collisional de-excitations. In Eq. 6.1 C^e (C^H) are the collisional excitation and de-excitation rates in $\text{cm}^3 \text{s}^{-1}$, with electrons (protons), A_{ul} is the coefficient of spontaneous emission, n_e (n_H) are the number density of e^- (protons). From requiring that the level population follows the Boltzmann distribution, the following relations must hold:

$$\begin{aligned} C_{lu} &= \frac{g_u}{g_l} e^{-T_*/T_k} C_{ul}, \\ g_l &= g_u \frac{B_{ul}}{B_{lu}}, \\ A_{ul} &= \frac{2h\nu^3}{c^2} B_{ul}. \end{aligned} \tag{6.2}$$

Let neglect the external field I_ν and focus our attention on the collisions with e^- , nevertheless the same argument that follows applies also to the collisions with protons. For the specific case of the [C II] 158 μm transition, the expression of C_{ul}^e is:

$$C_{\text{CII}}^e(T_k) = \frac{8.63^{-6}}{g_l \sqrt{T}} \gamma_{lu}(T_k) e^{-T_*/T_k} \tag{6.3}$$

with $\gamma_{lu}(T) \approx 1.6$ if $100 < T_k < 10^3$ (Gong et al., 2012). The numerical expression of $C_{ul}^H(T)$ can be found Dalgarno & McCray (1972).

The gas emissivity for the transition is given by $\varepsilon_\nu = n_u A_{ul}$; if the density n_e is much lower than the critical density $n_{\text{crit}} \equiv A_{ul}/C_{ul}$ we have:

$$n_u \simeq n_e C_{lu} A_{ul} n_l \tag{6.4}$$

and therefore the [C II] emissivity becomes:

$$\varepsilon_\nu \simeq n_e n_l C_{lu} \simeq n_e n C_{lu} \tag{6.5}$$

where $n = n_l + n_u \equiv n_{\text{CII}}$ is the total density of the ionized carbon. Using equation 6.3, and substituting $A_{ul} = 2.36 \times 10^{-6} \text{s}^{-1}$, we obtain $n_{\text{crit}}^e = 8 \text{cm}^{-3}$. A similar calculation for H atom collisions yields $n_{\text{crit}}^H \approx 3000 \text{cm}^{-3}$.

We verified that in our simulation either n_e and n_H are below the respective critical density, therefore the [C II] emissivity *from the diffuse medium*, neglecting the external radiation field I_ν is calculated according to the equation (6.5) by summing

the contribution of electrons and protons collisions:

$$\varepsilon_{\text{C II}} = C_{\text{C II}}^H f_{\text{C II}} n^2 + C_{\text{C II}}^{e-} f_{\text{C II}} x_e n^2, \quad (6.6)$$

In the previous equation n and T are the density and temperature of the WNM/CNM achieved with the sub-grid model discussed in Chapter 4, $n_{\text{C II}} = f_{\text{C II}} n$ is the abundance of the [C II] that scales linearly with the metallicity $f_{\text{C II}} = (f_C)_\odot \frac{Z}{Z_\odot}$, and $x_e = n_e/n$ is the ionized fraction in the neutral medium. In our simulation $x_e \approx 10^{-4}$ in the CNM and $x_e \approx 10^{-3}$ in the WNM.

To calculate the [C II] emissivity *from PDRs*, we follow the procedure outlined in Sec. 5.3.1. We set as input of UCL_PDR the density of the clumps calculated as in Sec. 5.2, the metallicity accordingly to the chosen profile, and G_0 computed as in Eq. 4.2:

$$G(\vec{r}) = \left(\frac{\text{SFR}}{\text{M}_\odot \text{ yr}^{-1}} \right) \sum_{i=1}^{n_*} \frac{\int_{6 \text{ eV}}^{13.6 \text{ eV}} L_{\nu,i}^{\text{SFR}=1.0} d\nu}{4\pi |\vec{r} - \vec{r}_i|^2}, \quad (6.7)$$

with SFR in the range $[0.1 - 100] \text{ M}_\odot \text{ yr}^{-1}$.

As discussed for the first time by Gong et al. (2012), the soft UV background at 1330 \AA generated by the stars can in principle pump the [C II] ions from the energy level $^2P_{1/2}$ to $^2D_{3/2}$. This pumping effect, can lead to the [C II] fine structure transition $^2D_{3/2} \rightarrow ^2P_{3/2} \rightarrow ^2P_{1/2}$, which would mix the levels of the [C II] 158 \mu m line. Hence, Eq. (6.1) becomes:

$$\frac{n_u}{n_l} = \frac{B_{lu} I_\nu + n_e C_{lu}^e + n_H C_{lu}^H + P_{lu}^{UV}}{B_{ul} I_\nu + A_{ul} + n_e C_{ul}^e + n_H C_{ul}^H + P_{ul}^{UV}} \quad (6.8)$$

where P_{lu}^{UV} (P_{ul}^{UV}) are the UV de-excitation (excitation) rates (Gong et al., 2012). These coefficients depends on the intensity I_{UV} (in $\text{erg s}^{-1} \text{ cm}^{-2} \text{ Hz}^{-1} \text{ sr}^{-1}$). We calculate I_{UV} relating it to the intensity in the Habing band G_0 :

$$I_{\text{UV}} \approx \frac{G_0}{4\pi} \left(\frac{\Delta\nu_{\text{Habing}}}{\text{Hz}} \right) \simeq 6 \times 10^{-20} G_0 \quad (6.9)$$

where G_0 (in $\text{erg s}^{-1} \text{ cm}^{-2}$).

The Eq. 6.8 formally defines the excitation (or spin) temperature T_s of the

transition:

$$\frac{n_u}{n_l} \equiv \frac{g_u}{g_l} e^{-T_*/T_s} \quad (6.10)$$

where $T_* = \Delta E_{ul}/k_B$. For the [C II] 158 μm transition the statistical weights of the upper and lower level are respectively: $g_u = 4$ and $g_l = 2$, and $T_* \approx 91$ K. We can directly invert Eq. 6.8 and, using the relations 6.2 we obtain (Gong et al., 2012):

$$\frac{T_*}{T_s} = \ln \frac{A_{ul}(1 + \frac{c^2 I_\nu}{2h\nu^3}) + n_e C_{ul}^e + n_H C_{ul}^H + P_{ul}^{\text{UV}}}{A_{ul}(\frac{c^2 I_\nu}{2h\nu^3}) + n_e C_{ul}^e e^{-\frac{T_*}{T_k}} + n_H C_{ul}^H e^{-\frac{T_*}{T_k}} + P_{lu}^{\text{UV}}} \quad (6.11)$$

6.1.1 CMB effects on [C II] emission

So far we have considered the emitting gas as isolated and computed the emissivity due to collisional excitations. However the gas is immersed in the cosmic microwave background that, at high- z , can have a substantial effect on the visibility of the lines. The CMB sets the minimum temperature of the ISM to $T_{\text{CMB}} = T_{\text{CMB}}^0(1 + z)$ and, more importantly, it becomes an increasingly stronger background against which the line fluxes are detected (e.g. Lidz et al., 2011; Gong et al., 2012; Muñoz & Furlanetto, 2013; da Cunha et al., 2013).

The radiative transfer equation for the background intensity is:

$$\frac{dI_\nu}{ds} = -k_\nu I_\nu + \varepsilon_\nu \quad (6.12)$$

where k_ν is the absorption coefficient and ε_ν is the emissivity, in this case given by Eq. 6.6. Recalling that the optical depth is $d\tau_\nu = -k_\nu ds$ and defining $S_\nu(T) = \varepsilon_\nu/k_\nu$, the previous equation can be written as:

$$\frac{dI_\nu}{d\tau} = I_\nu - S_\nu(T). \quad (6.13)$$

Integration of Eq. 6.13, yields:

$$I_\nu(s) = I_\nu(0)e^{-\tau_\nu} + S_\nu(T)(1 - e^{-\tau_\nu}) \quad (6.14)$$

Note that in LTE, $S_\nu(T) = B_\nu(T_s)$ and, if we assume that the only background is the CMB, $I_\nu(0) = B_\nu(T_{\text{CMB}})$. Given that, the contrast of the cloud emission against the CMB radiation becomes:

$$\Delta I_\nu = [B_\nu(T_s) - B_\nu(T_{\text{CMB}})] (1 - e^{-\tau_\nu}) \quad (6.15)$$

If we assume that the [C II] line is optically thin in the sub-millimeter, i.e. $e^{-\tau_\nu} \approx 1 - \tau_\nu$, the fraction of observed flux ($(1+z)F_\nu \sim I_\nu/d_L^2$) against the CMB over the flux that would have been observed without the background results (see also [da Cunha et al., 2013](#)):

$$\zeta \equiv \frac{F_\nu^{\text{against}}}{F_\nu^{\text{int}}} = \frac{[B_\nu(T_s) - B_\nu(T_{\text{CMB}})] \tau_\nu}{B_\nu(T_s) \tau_\nu} = 1 - \frac{B_\nu(T_{\text{CMB}})}{B_\nu(T_s)} \quad (6.16)$$

This equation clearly shows that if the T_{CMB} approaches to the T_s the observed flux against the background approaches to zero.

We calculated T_s for the PDRs and the CNM. We find that $T_s^{\text{PDR}} \sim 30 - 120 \text{ K}$ for $\text{SFR} = 0.1 - 100 M_\odot \text{ yr}^{-1}$, while $T_s^{\text{CNM}} \sim 22 - 23 \text{ K}$ is approximately constant in the range of SFR considered. This implies that, at $z \approx 6.6$ ($T_{\text{CMB}} \approx 20.7 \text{ K}$), the [CII] emission arising from PDRs is only slightly affected by the CMB ($\zeta \approx 0.8 - 1.0$). Viceversa, the CNM is strongly attenuated at this redshift ($\zeta \approx 0.1 - 0.2$); in this case the CMB effect becomes negligible only for galaxies at $z \leq 4.5$.

We finally note that UV pumping effects are negligible in our calculations. As a matter of fact, the UV intensity inside the galaxy for all the SFR values considered is $\ll 10^{-15} \text{ erg s}^{-1} \text{ cm}^{-2} \text{ Hz}^{-1} \text{ sr}^{-1}$, the critical value for this effect to become important ([Gong et al., 2012](#)).

6.2 Results

In Fig. 6.1, we show the [C II] spectrum obtained from the P005 model, assuming $\text{SFR} = 1 M_\odot \text{ yr}^{-1}$ (top panel) and $\text{SFR} = 10 M_\odot \text{ yr}^{-1}$ (bottom panel). In this Figure, the contribution to the [C II] emission arising from PDRs and the CNM is shown in green and blue, respectively.

The emission from PDRs arises predominantly from the center of the galaxy, covering the velocity channels around $\sim 0 \text{ km s}^{-1}$. The second peak in the PDR

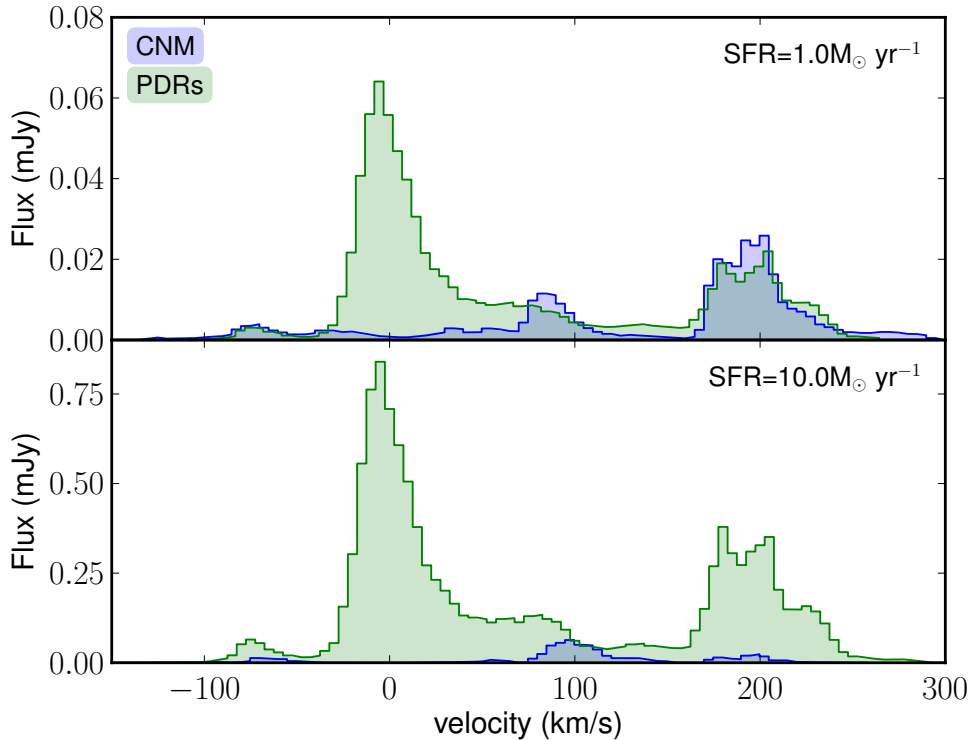


Figure 6.1: $[\text{C II}]$ spectrum for the P005 model assuming $\text{SFR}=1\text{M}_{\odot}\text{yr}^{-1}$ (upper panel) and $\text{SFR}=10\text{M}_{\odot}\text{yr}^{-1}$ (lower panel) and rebinned over 5km/s velocity channels. The emission from PDRs (diffuse neutral medium) is plotted in green (blue).

emission at $v \sim 200\text{km s}^{-1}$ is produced by MCs located in the CNM clumps at the periphery of the galaxy (see Fig. 5.1). $[\text{C II}]$ emission from the diffuse medium, visible as the two peaks around $\sim 100\text{km s}^{-1}$ and $\sim 200\text{km s}^{-1}$ is instead always displaced from the center of the galaxy. The $[\text{C II}]$ line is relatively narrow, with a $\text{FWHM} \sim 50\text{km s}^{-1}$, as in Chapter 4.

In Fig. 6.2 we plot the relative contribution of the diffuse medium to the total $[\text{C II}]$ emission, $F_{\text{diff}}/F_{\text{tot}}$, as a function of the SFR, for different C- and P-models, taking into account the CMB attenuation (dark blue). We find that the $[\text{C II}]$ emission in $z \approx 6$ galaxies is dominated by PDRs, since the CNM contribution is always $\leq 10\%$, regardless of the metallicity profile and SFR considered. When the CMB attenuation of the CNM luminosity is negligible (i.e. typically for sources located at $z \leq 4.5$ see Sec. 6.1.1), we find $F_{\text{diff}}/F_{\text{tot}} = 0.05 - 0.45$, consistently with several observations of $[\text{C II}]$ emission in nearby galaxies (Cormier et al., 2012; Kramer et al., 2013; Parkin et al., 2013; Langer et al., 2014).

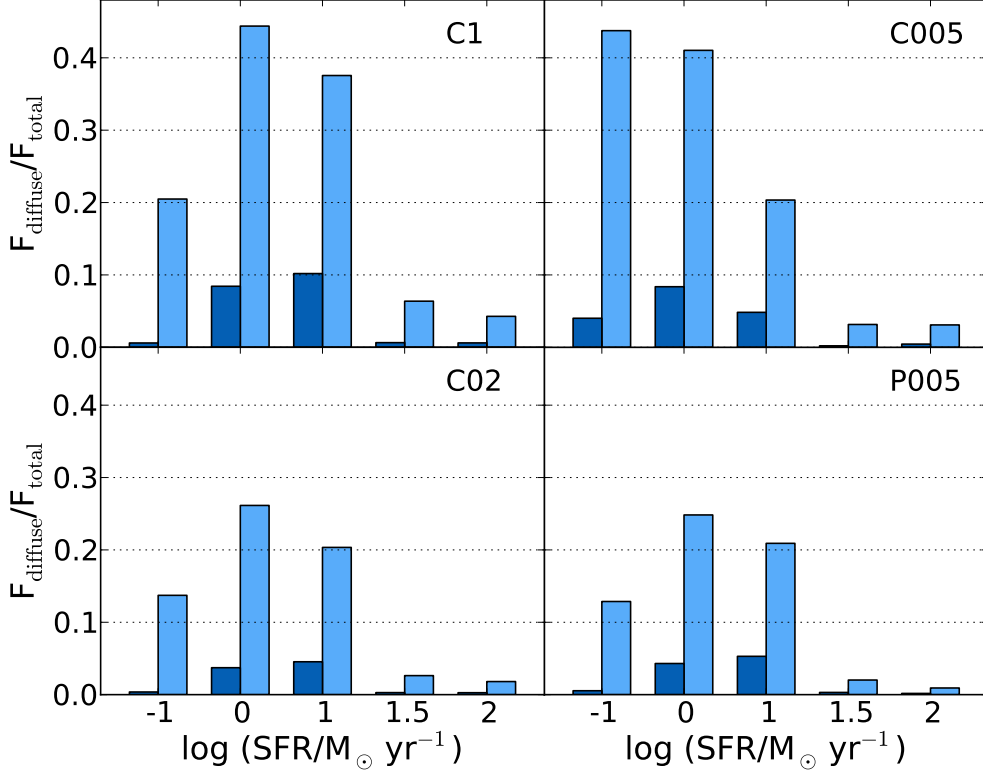


Figure 6.2: Fraction of the [C II] flux arising from the diffuse medium (F_{diff}) over the total flux (F_{tot}), for four different models, as a function of the SFR, with (dark blue) and without (light blue) taking into account CMB effects on the [C II] emission.

6.3 [C II]-SFR relation

In the previous Section, we have found that the [C II] emission is dominated by PDRs, implying $L_{\text{CII}} \propto M_{\text{H}_2}$. To rescale the [C II] luminosity of our “fiducial” model ($\text{SFR} = 10 M_{\odot} \text{ yr}^{-1}$, $M_{\text{H}_2} = 4 \times 10^8 M_{\odot}$), to an arbitrary molecular content, we assume the most updated version of the Kennicutt-Schmidt relation (Kennicutt, 1998), namely $\Sigma_{\text{SFR}} \sim \Sigma_{\text{H}_2}^{1.0 \pm 0.2}$ (Bigiel et al., 2008), where Σ_{SFR} and Σ_{H_2} are the SFR and molecular hydrogen surface density, respectively. In Fig. 6.3, we show the result of this procedure for different metallicity profiles. Solid lines represent our results for models with uniform metallicity $Z = Z_{\odot}$ (C1, black line), $Z = 0.2 Z_{\odot}$ (C02, orange line), and $Z = 0.05 Z_{\odot}$ (C005, blue line). The results from our C-models are well described by the following best-fitting formula:

$$\begin{aligned} \log L_{\text{CII}} = & 7.0 + 1.2 \log(\text{SFR}) + 0.021 \log(Z) + \\ & 0.012 \log(\text{SFR}) \log(Z) - 0.74 \log^2(Z). \end{aligned} \quad (6.17)$$

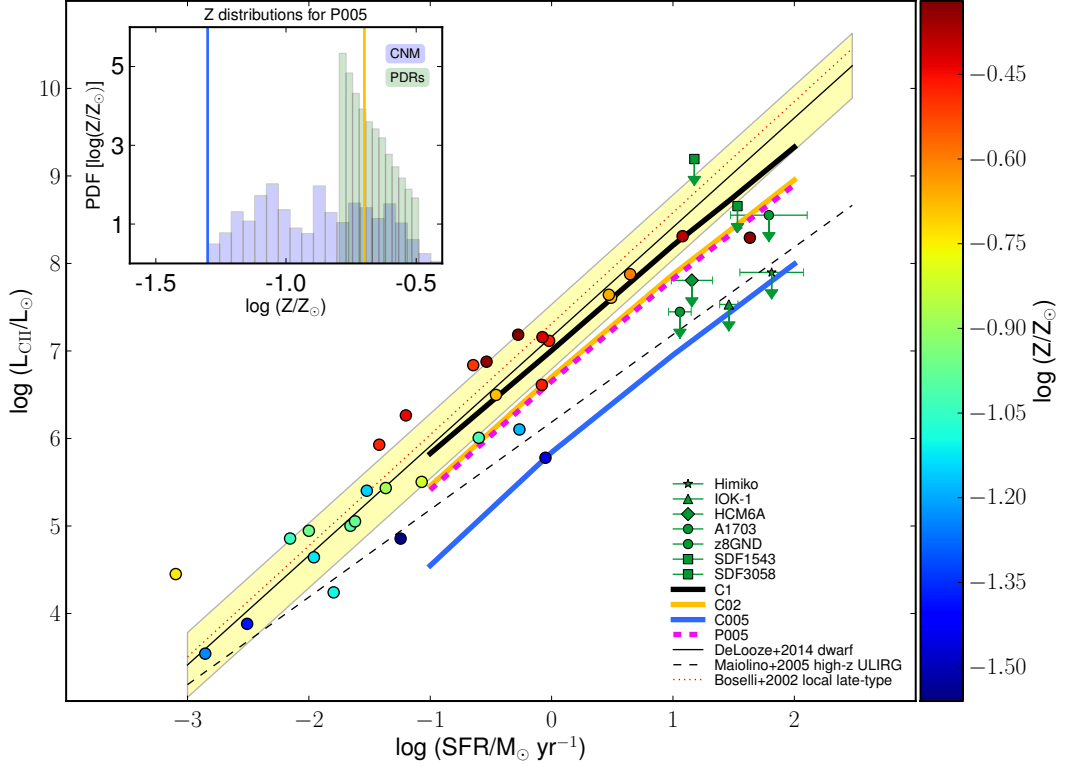


Figure 6.3: Predicted $[C\ II]$ -SFR relation. Solid lines correspond to uniform gas metallicity cases, with $Z = Z_{\odot}$ (C1, black), $Z = 0.20 Z_{\odot}$ (C02, yellow) and $Z = 0.05 Z_{\odot}$ (C005, blue). The magenta dashed line corresponds to a density-dependent metallicity (see Sec. 2.2) with $\langle Z \rangle = 0.05 Z_{\odot}$ (P005). In the inset, the metallicity distribution of CNM and PDRs are shown for the P005 model. Note that in this case the molecular clouds metallicity is similar to the C02 model $\approx 0.2 Z_{\odot} > \langle Z \rangle$. Model predictions are compared with data from local late-type galaxies (dotted line), high- z ULIRGs (dashed line), local dwarf galaxies (solid line and dashed region), individually denoted by dots color-coded according to their Z (De Looze et al., 2014). Green arrows represent upper limits on the $[C\ II]$ luminosity for LAEs and LBGs at $z \approx 6 - 7$: Himiko (Ouchi et al., 2013; Ota et al., 2014), IOK-1 (Ota et al., 2014), A1703-zD1 and z8-GND-5296 (Schaerer et al., 2015), SDF1543 and SDF3058 (González-López et al., 2014).

with $L_{\text{C II}}$ in solar units, and the SFR in $M_{\odot} \text{ yr}^{-1}$. The dashed line indicates the predictions for the Z - Δ relation with $\langle Z \rangle = 0.05 Z_{\odot}$ (P005). The results shown in Fig. 6.3 are also summarized in Tab. 6.1. The slope of the [C II]-SFR relation does not depend neither on $\langle Z \rangle$ nor on the metallicity distribution. Moreover, the [C II] luminosity predicted by the P005 model is almost coincident with that obtained from the C02 model, in the entire range of SFR considered. This can be understood by inspecting the upper left inset in the Fig. 6.3, where we plot the probability distribution function (PDF) of the CNM and PDR metallicities for the P005 model. It is evident that the metallicity of the photodissociation regions, dominating the emission, is $Z_{\text{PDR}} > \langle Z \rangle$ and, more precisely, $Z_{\text{PDR}} \approx 0.2 Z_{\odot}$, namely the metallicity value of the C02 model (vertical orange line).

We compare our predictions with local late-type galaxies (dotted line), high- z ULIRGs (dashed line), local dwarf galaxies (solid line and dashed region), individually denoted by dots color-coded according to their Z (De Looze et al., 2014). We also indicate through green arrows upper limits obtained for LAEs and LBGs at $z \approx 6-7$ (Ouchi et al., 2013; Ota et al., 2014; González-López et al., 2014; Schaerer et al., 2015). The [C II]-SFR relation predicted by our model fairly reproduces the slope of the relation found in local dwarfs, as well as its trend with metallicity, although the scatter in the data is large. Considering the deepest upper limit currently available on the [C II] luminosity ($L_{[\text{C II}]} < 2.8 \times 10^7 L_{\odot}$, Schaerer et al., 2015) for a LBG at $z \sim 6.8$, characterized by $\text{SFR} \approx 10 M_{\odot} \text{ yr}^{-1}$, our study suggests $Z < 0.1 Z_{\odot}$.

6.4 Summary and Discussion

By coupling radiative transfer cosmological simulations of a $z = 6.6$ galaxy with a sub-grid ISM model and a PDR code (UCL_PDR), we have computed the [C II] emission arising from the diffuse cold neutral medium and molecular clouds in early galaxies, characterized by SFRs ranging from 0.1 to $100 M_{\odot} \text{ yr}^{-1}$. We have distributed metals in the ISM, both uniformly and according to the $Z - \Delta$ relation found by Pallottini et al. (2014), to simulate gas metallicities in the range $0.05-1 Z_{\odot}$.

We find that the [C II] line from high- z galaxies is dominated by emission from PDRs, while the CNM accounts for $\leq 10\%$ of the total flux. This is due to the fact that at these early epochs the CMB temperature approaches the spin temperature

of the [C II] transition in the CNM ($T_{\text{CMB}} \sim T_s^{\text{CNM}} \sim 20$ K) suppressing the flux contrast. The [C II] spectrum predicted by our model is complex. It shows a pronounced peak (FWHM ~ 50 km s $^{-1}$) due to centrally located ($v = 0$) PDRs, and weaker [C II] displaced ($v \sim 200$ km s $^{-1}$) peaks from MCs in the galaxy outskirts.

The predicted [C II]-SFR relation reproduces the corresponding relation found in local dwarfs remarkably well. Current upper limits from observations of $z \sim 6-7$ NSFGs seem to indicate that these galaxies are characterized by a [C II] luminosity fainter than expected from the local relation. Although this conclusion is still not definitive, it must be noted that the SFRs quoted for high- z galaxies are inferred from observations of the Ly α emission line, and therefore must be considered as lower limits to the actual value. This implies that green arrows in Fig. 6.3 should be moved towards higher SFR values, hence exacerbating the inconsistency with the local relation.

Our results contain a caveat: we have so far neglected the possible effect of stellar feedback (i.e. photo-evaporation, radiation pressure, H II thermal pressure) on molecular clouds. Broadly speaking, these effects should act to reduce the mass of the molecular gas (Tasker & Tan, 2009; Tasker, 2011; Tasker et al., 2015). On the other hand, the expansion of [H II] regions might have either a positive effect, by triggering new star formation (e.g. Mellema et al., 2006; Bisbas et al., 2011; Haworth & Harries, 2012), or disperse the surrounding cloud (Dale et al., 2005). Typical timescales for the negative feedback range from 1 to 10 Myr (Krumholz et al., 2006; Walch et al., 2012), namely the age of the stars taken into account in our radiative transfer calculations. We defer to future work a thorough implementation of stellar feedback effect on MC properties. Here, we argue that *a [C II] deficit in $z \sim 6-7$ galaxies, if confirmed by deeper observations, would favor a scenario in which star formation in early galaxies blows the molecular gas apart*, reducing the amount of material from which most of the [C II] emission arises, i.e. PDRs. The deviation from the local [C II]-SFR would then imply a modified Kennicutt-Schmidt relation in $z > 6$ galaxies (e.g. Gnedin & Kravtsov, 2010). Stellar feedback effects are likely to be stronger in regions of very active star formation, more often located in the galactic center. If so, negative feedback should preferentially suppress the peak in the [C II] spectrum at the systemic redshift of the galaxy. *Alternatively/in addition, the deficit might be explained by low gas metallicities.* For instance, the deepest upper limit at high- z ($L_{\text{CII}} < 2.8 \times 10^7 L_{\odot}$) is consistent with a $Z < 0.1 Z_{\odot}$ population of early galaxies.

SFR ($M_{\odot} \text{ yr}^{-1}$)	$F_{\text{diff}}/F_{\text{tot}}$ (%)				L_{CII} (L_{\odot})			
	P005	C005	C02	C1	P005	C005	C02	C1
0.1	0.5	0.04	0.4	0.6	2.6×10^5	3.5×10^4	2.9×10^5	6.7×10^5
1.0	4.3	8.4	3.7	8.4	4.5×10^6	6.9×10^5	5.0×10^6	1.0×10^7
10.0	5.3	4.8	4.5	10.2	6.6×10^7	8.9×10^6	7.5×10^7	1.6×10^8
30.0	3.0	0.2	0.3	0.6	2.2×10^8	2.8×10^7	2.4×10^8	5.4×10^8
100.0	0.2	0.4	0.3	0.6	7.9×10^8	9.9×10^7	8.9×10^8	8.9×10^8

Table 6.1: In this table we show the fraction of the [C II] emission arising from the CNM ($F_{\text{diff}}/F_{\text{tot}}$) for the various model (P005, C005, C02, and C1), after correcting for the effect of the CMB temperature. We present also the predicted [C II] luminosity, in solar units.

Finally, we note that the MC density distribution may play a role. Our simulated galaxy is characterized by a mean molecular hydrogen number density $n_{\text{cl}} \sim 10^{2.9} \text{ cm}^{-3}$; this quantity depends on the square of the assumed Mach number $\mathcal{M} = 10$. Calculations performed with UCL_PDR show that molecular clouds characterized by densities 10 times higher (lower), for a fixed gas metallicity (e.g. $\log(Z/Z_{\odot}) = -1.5$), would result into a [C II] emissivity 5 times higher (20 times lower) than found here (see Fig. 5.3 in the previous Chapter). Although we consider such large variations of the Mach number unlikely, at present we cannot exclude that the corresponding shift in the mean MC density plays some role in the interpretation of the results.

Interpreting the observations 7

AS OUTLINED in the Introduction, the final aim of this work is to build a physically motivated model capable to shed light on the nature of the interstellar medium of high- z galaxies. The model, as discussed for instance in Sec. 4.4, provides predictions that are in fair agreement with experiments and hence it represents an helpful tool constrain the ISM properties from the detection (or the non detection) of FIR lines.

We devote this Chapter to a detailed discussion on the search of [C II] emission from LAEs and LBGs at $z > 6.5$ (González-López et al., 2014, hereafter GL14), and on the conclusions that we can draw from these experiments by considering our model. The final part of the Chapter will focus on an ongoing work (Maiolino et al. 2015, in prep. Hereafter MA15) in which ALMA data on the [C II] emission from a $z \approx 7.1$ LBG has been interpreted by adopting the findings of this Thesis.

7.1 Searching [CII] line in $z > 6.5$ galaxies

The three Lyman- α emitters targeted by González-López et al. (2014) were discovered in the Subaru Deep Field (SDF). Two of the LAEs observed belong to the sample of LAEs at $z \sim 6.6$ discovered by Taniguchi et al. (2005). The targets are the brightest LAEs (sources 3 and 4 in their catalog) and have a narrow and bright Lyman- α emission line. The third LAE (IOK-1) was discovered at $z \sim 7$ by Iye et al. (2006). It is one of the brightest and most distant LAEs known to date (see also Fig. 1.4). The fourth target, MACS0647-JD, is a lensed LBG discovered behind the galaxy cluster MACSJ0647.7+7015 at $z = 0.591$ (Coe et al., 2013). The galaxy was discovered as a J-Dropout galaxy lensed into 3 magnified images as part

of The Cluster Lensing And Supernova survey with Hubble (CLASH) (Postman et al., 2012). The three images of the galaxy MACS0647-JD1, MACS0647-JD2 and MACS0647-JD3, have a magnification of $\sim 8, \sim 7$ and ~ 2 respectively. The photometric redshift of the galaxy is $10.7_{-0.4}^{+0.6}$ (95% confidence limits). This is one of the highest redshift galaxy candidates known to date.

CARMA Observations

Observations of the three $z \sim 6.5 - 7$ LAEs were carried out using the Combined Array for Research in Millimeter-wave Astronomy (CARMA) between 2008 July and 2010 July. The array configurations used were D and E to minimize phase decoherence and maximize point source sensitivity. The [C II] line has a rest frequency of 1900.54 GHz (157.74 μm). For the redshifts of the targets, the line is shifted to the 1 mm band. The receivers were tuned to a frequency ~ 150 km/s bluer than the expected frequency from the redshift determined by the peak of the Lyman- α line. This is for taking into account the possible absorption by the IGM in the Lyman- α line. The setups provide an instantaneous bandwidth of ~ 1.5 GHz with a spectral resolution of 31.25 MHz ($\sim 37 - 39$ km/s). The time on source for IOK-1 was 58.5 hours, for SDF J132415.7+273058 was 15.9 hours and for SDF J132408.3+271543 4.6 hours. The final cubes were made using natural weighting to maximize point source sensitivity. The observations resulted in the following beam-sizes: IOK-1: $1.86'' \times 1.33''$, PA = -0.34° , SDF J132415.7+273058: $1.92'' \times 1.56''$, PA = 83.45° , SDF J132408.3+271543: $2.54'' \times 2.01''$, PA = 88.02° (all targets: D and E configurations). For D configuration the minimum baseline is 11 meters and the maximum is 150 meters. For E configuration the minimum baseline is 8 meters and the maximum is 66 meters. Table 7.1 summarizes the sensitivities reached for the observations of the LAEs.

PdBI Observations

All MACS0647-JD observations were carried out in 2012 November as part of a DDT (Director's Discretionary Time) program with the Plateau de Bure Interferometer (PdBI). The target was observed with 4 WideX frequency setups (3.6 GHz bandwidth each), covering 80% of the photometric redshift range ($\nu_{\text{obs}} = 156.7 - 171.1$ GHz). Two of the three lensed images (JD1 and JD2) are within $18''$ each other and they were covered in a common 2 mm pointing. The absolute flux

calibrators used are MWC349, 2200+420, 3C279 and 0716+714. As gain calibrator the QSO 0716+714 was used. The total on source time for all tunings was 7.4 hours (6-antennas equivalent). The observations were processed using GILDAS. The beamsize of the observations is the following: MACS0647-JD : $2.10'' \times 1.76''$, PA= 102.0° (C configuration). For C configuration the minimum baseline is 22 meters and the maximum is 184 meters. Table 7.2 summarizes the sensitivity reached for the observations of MACS0647-JD .

7.1.1 Results

The spectra of the three $z \sim 6.5 - 7$ LAEs are presented in Fig. 7.1 and the spectrum of MACS0647-JD is shown in Fig. 7.2. No significant emission is detected at the redshifted line frequencies or close to them. The observations were sampled to a channel resolution of 50 km/s similar to the expected FWHM of the [C II] emission line (see Sect. 7.1.2). The non-detections are used to put constraints on the luminosities of the [C II] lines for all targets. The results for the LAEs can be seen in the Table 7.1 and for the MACS0647-JD in Table 7.2. The [C II] luminosities were estimated assuming that the velocity integrated flux of the line is $I_{\text{line}} = S_{\text{line}} \Delta v$, with S_{line} being 3 times the r.m.s. of the 50 km s⁻¹ channel and $\Delta v = 50$ km s⁻¹ the range in velocity (details on Tab. 7.1 notes). Using 3σ over a 50 km s⁻¹ channel to estimate the upper limit in the luminosities can result in an underestimation. For a more conservative estimation the luminosities should be multiplied by a factor 2. (i.e. 3σ over 200 km/s channel). Assuming a channel width of 200 km s⁻¹, the IOK-1 [C II] limit is $\sim 10\%$ deeper than the previous PdBI limit (Walter et al., 2012b).

The GL14 included tentative searches for the continuum emission of the three LAEs and the $z \sim 11$ LBG. The interested reader can find the complete discussion about this topic in González-López et al. (2014); in what follows we focus our attention only on the [C II] line results.

7.1.2 Width of the [C II] emission line

Previous studies have presented the non-detection of [C II] (Walter et al., 2012b; Ouchi et al., 2013) with a channel resolution of 200 km s⁻¹, a choice motivated by the width of the Ly α emission line. However recent observations and the models presented in this Thesis suggest that the [C II] line could be narrower than the pre-

source	z	ν_{obs} GHz	σ_c mJy b ⁻¹	σ_l mJy b ⁻¹	L_{CII} 10 ⁸ L _⊙	$L_{IR,CMB}^{N6946}$ 10 ¹¹ L _⊙	SFR _d M _⊙ yr ⁻¹	SFR _{UV} M _⊙ yr ⁻¹
IOK-1	6.9	238.9	0.19	1.17	< 2.05	< 6.34	< 109	24
J132415	6.5	252.2	0.37	2.82	< 4.52	< 10.3	< 177	34
J132408	6.6	251.6	0.75	5.67	< 10.56	< 21.0	< 361	15

Table 7.1: Note: All luminosities upper limits are 3σ . (col. 2) Redshift, references: IOK-1: [Iye et al. \(2006\)](#); [Ono et al. \(2012\)](#). SDF J132415.7+273058 and SDF J132408.3+271543: [Taniguchi et al. \(2005\)](#). (col. 3) Observing Frequencies; tuned ~ 125 MHz blueward of the Ly α redshifts for all targets. (col. 4) 1σ continuum sensitivity at $158\mu\text{m}$ rest wavelength. (col. 5) 1σ [C II] line sensitivity over a channel width of 50 km s^{-1} . (col. 6) 3σ [C II] luminosity limit over a channel width of 50 km s^{-1} . (col. 7) 3σ limit based on the SED of NGC 6946 and including the effect of the CMB. (col. 8) 3σ limit based on L_{IR}^{N6946} including the effect of the CMB. (col. 8) UV-based SFR from [Jiang et al. \(2013\)](#).

Parameter	MACS0647-JD1, JD2
Coordinates (J2000) JD1	0.6 : 47 : 55.731, +70 : 14 : 35.76
Coordinates (J2000) JD2	0.6 : 47 : 55.112, +70 : 14 : 22.94
μ (JD1 + JD2)	~ 15
Redshift	10.7
UV SFR	~ 1 [M _⊙ yr ⁻¹]
ν	156.7 – 171.1 [GHz]
σ_{cont} ^a	0.13 mJy
σ_{line} (Setup A) ^b	2.57 mJy
σ_{line} (Setup B) ^b	3.20 mJy
σ_{line} (Setup C) ^b	2.48 mJy
σ_{line} (Setup D) ^b	4.98 mJy
$L_{[C II]}$ (Setup C) ^c	$< 5.27 \times 10^7 \times (\mu/15)^{-1} [L_{\odot}]$
$L_{[C II]}$ (Setup D) ^c	$< 1.05 \times 10^8 \times (\mu/15)^{-1} [L_{\odot}]$
L_{IR}^{N6946} (Corrected CMB) ^d	$< 1.28 \times 10^{11} \times (\mu/15)^{-1} [L_{\odot}]$
SFR (L_{FIR}) (Corrected CMB) ^e	$< 22 \times (\mu/15)^{-1} [M_{\odot}\text{yr}^{-1}]$
SFR ($L_{[C II]}$) (Setup C) ^f	$< 4 \times (\mu/15)^{-1} [M_{\odot}\text{yr}^{-1}]$
SFR ($L_{[C II]}$) (Setup D) ^f	$< 7 \times (\mu/15)^{-1} [M_{\odot}\text{yr}^{-1}]$

Table 7.2: Note: All luminosities upper limits are 3σ . Coordinates, magnification, redshift and UV-SFR from [Coe et al. \(2013\)](#). All the luminosities and SFR are corrected by magnification. (a) 1σ continuum sensitivity at $158\mu\text{m}$ rest wavelength. (b) 1σ [C II] line sensitivity over a channel width of 50 km s^{-1} . (c) 3σ [C II] luminosity limit over a channel width of 50 km s^{-1} as in Tab. 7.1. The two results correspond to the most sensitive and the least sensitive setups. (d) 3σ limit based on the SED of NGC 6946 and including the effect of the CMB. (e) 3σ limit based on L_{IR}^{N6946} including the effect of the CMB. (f) Based on the [de Looze et al. \(2011\)](#) $L_{[C II]} - SFR$ relation. The two results correspond to the most sensitive and the least sensitive setups.

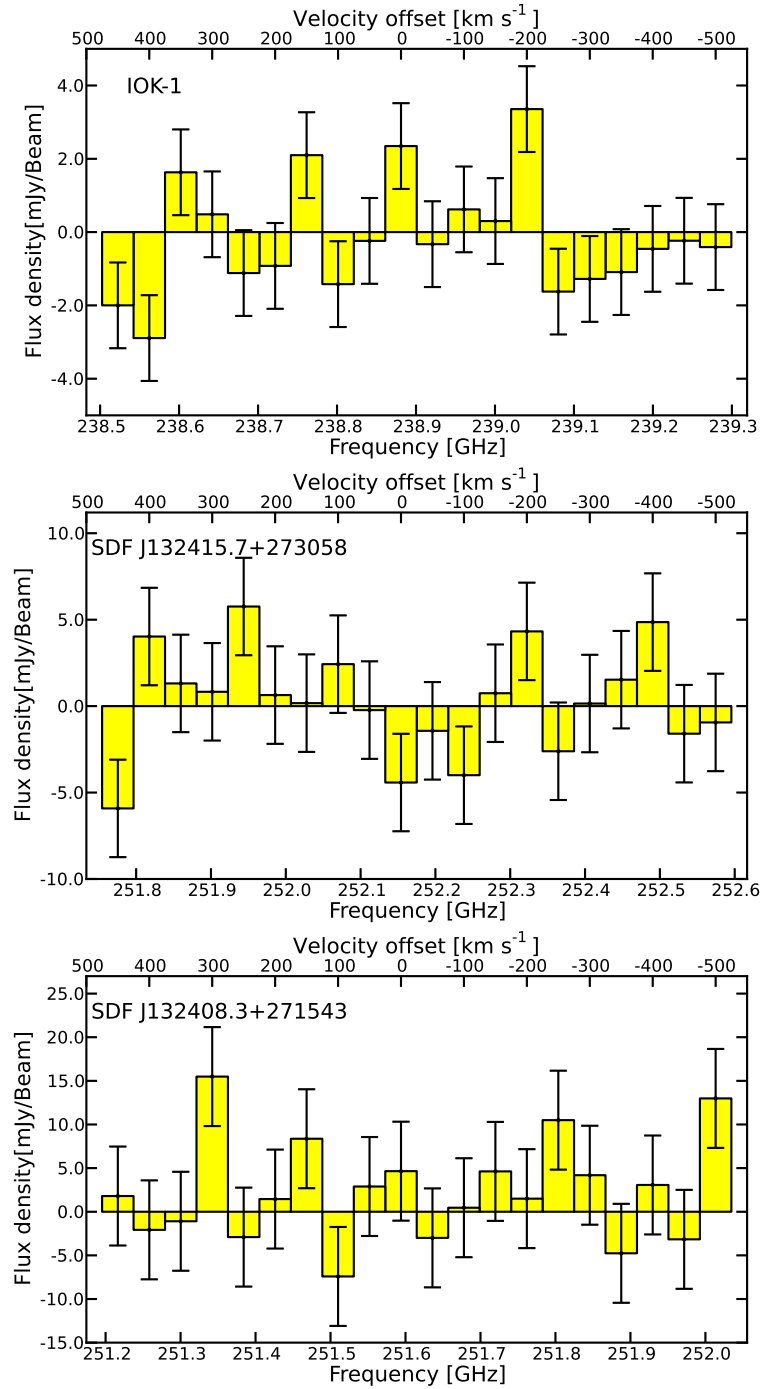


Figure 7.1: Spectra of the LAEs with a velocity resolution of 50 km s^{-1} . The relative velocities are with respect to the frequency expected for the [C II] line including absorption by the IGM. The redshifts of the target are $z=6.965$ for IOK-1, $z=6.541$ for SDF J132415.7+273058 and $z=6.554$ for SDF J132408.3+271543 .

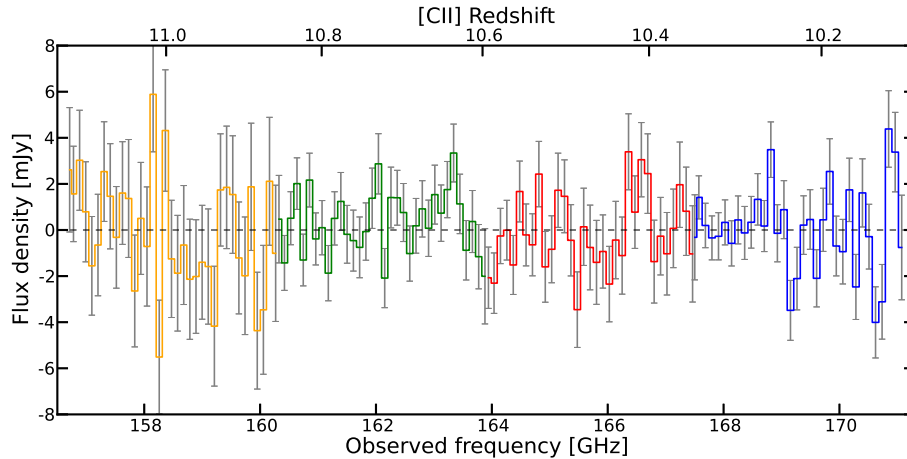


Figure 7.2: Spectrum of MACS0647-JD . The spectrum shows the added fluxes measured on the positions of the two lensed images JD1 and JD2 (combined magnification $\mu \sim 15$). The 4 setups are plotted in different colors, blue, red, green and orange the colors for the setups A, B, C and D respectively. The errors bars correspond to the quadrature of the errors of the individual measurement of the fluxes for JD1 and JD2 in each frequency channel. For display purposes, the spectrum is sampled at a channel resolution of 200 km/s, but the search of the [C II] line as well as the analysis was made with the spectrum sampled to 50 km s⁻¹.

viously assumed value.

In support of a the narrow emission line is the detection of [C II] in a LAE at $z = 4.7$ ($\text{Ly}\alpha - 1$) with ALMA (Carilli et al., 2013) already mentioned in Sec. 4.3. The FWHM of the emission line is 56 km s⁻¹, which is one order of magnitude narrower than the width of the $\text{Ly}\alpha$ emission line of ~ 1100 km s⁻¹ of the same source (Petitjean et al., 1996; Ohyama et al., 2004). Despite of the LAE being at a separation of 2.3'' (~ 15 kpc) to the quasar BRI 1202-0725, there is no evidence for a significant influence of the quasar on the properties of the LAE from the observations. Carilli et al. (2013) tried to model the emission of the LAE taking into account the radiation coming from the luminous nearby quasar. All the models that reproduce the [C II] and $\text{Ly}\alpha$ luminosities predict higher luminosities for other UV lines that are not detected (Ohyama et al., 2004). Given this results, they conclude that the quasar is unlikely the source of heating and ionization in the LAE. Based on deep, spatially resolved optical spectroscopy of the LAE, Ohyama et al. (2004) argue that the LAE is likely the composition of a normal star-forming galaxy and an extended nebula with violent kinematic status (see also the right-hand panel of Fig. 1.4). This nebula emission would produce a broadening of the $\text{Ly}\alpha$ emission. This nebula can be explained, at least in a qualitative way, as a superwind caused

by the supernovae explosion of OB stars in the late phase of the evolution of a starburst. In conclusion, this LAE is not intrinsically different from the general population of LAE. The [C II] detection in this LAE can thus be used as a reference for [C II] searches in other LAEs at high redshift.

As discussed in Chapters 4 and 6, our model also suggests narrow [C II] emission lines at high redshift for LAEs. As can be noted by inspecting Fig. 4.2 the spectrum for the simulated [C II] emission from our $z = 6.6$ galaxy has a FWHM of the main peak of $\sim 50 \text{ km s}^{-1}$, very similar to the 56 km s^{-1} of the LAE at $z = 4.7$. This suggest that the width of the [C II] line is at first order determined by the gravitational potential of the clumps. The [C II] emission produced in CNM follows the gravitational potential of the clumps, resulting in narrow emission lines associated with each clumps.

Hence, the value of $\sim 50 \text{ km s}^{-1}$ for the [C II] line in LAEs adopted in the analysis presented in Sec. 7.1.1 agrees with recent observations and simulations. Nevertheless, the only way to discard the possibility of [C II] lines being broader than this assumption is detecting them with much deeper observations.

7.1.3 Modeling [C II] emission from IOK-1

Using the same procedure outlined in Chapter 4 to calculate the [C II] emission from the diffuse medium of a $z = 6.6$ galaxy, we estimate the emission of [C II] for IOK-1 at $z \sim 7$. The sub-grid model has been re-run assuming a star formation rate of $20 M_{\odot} \text{ yr}^{-1}$ and a stellar population age of 10 Myr. The metallicity was set to solar to have a conservative estimation of the [C II] emission. The simulation does not include the emission from PDRs and should be seen as a lower limit. In Fig. 7.3, we show the [C II] emission produced by the three modeled phases, cold neutral medium (CNM), warm neutral medium (WNM) and the ionized medium. Most of the [C II] emission comes from the CNM ($\sim 50\%$), the rest is coming from the WNM ($\sim 20\%$) and from the ionized medium ($\sim 30\%$). For comparison, in Himiko, 95% of the emission is produced in the CNM and the rest in the WNM. No emission from the ionized medium was modeled in the simulation of Himiko (Vallini et al., 2013). We can also see in the emission that the FWHM of the main peak is $\sim 50 \text{ km s}^{-1}$, just as expected.

In Fig. 7.4, we present the integrated flux of [C II] for a different combination

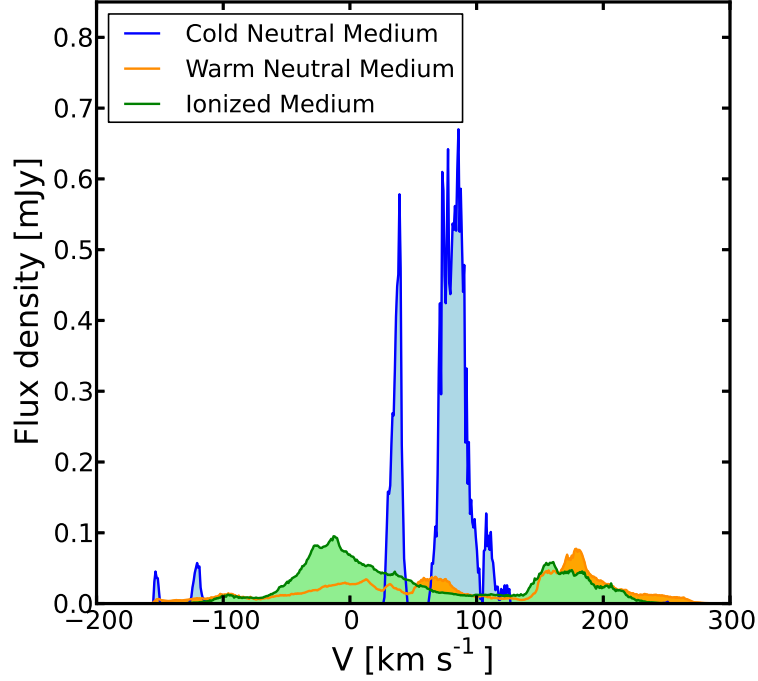


Figure 7.3: Simulated [C II] spectrum of a galaxy similar to IOK-1 at $z \sim 7$. The parameters set for this simulation were a SFR of $20M_{\odot}\text{yr}^{-1}$, and stellar population age of 10 Myr and a solar metallicity. The blue spectrum corresponds to the emission produced in the cold neutral medium, the orange spectrum corresponds to the emission produced in the warm neutral medium and the green spectrum corresponds to the emission produced in the ionized medium. The main peak (at $\sim 80 \text{ km s}^{-1}$) of the cold neutral medium has a FWHM of $\sim 50 \text{ km s}^{-1}$. For more details on the simulations of [C II] emission in high redshift galaxies see [Vallini et al. \(2013\)](#).

of metallicities and stellar population ages. This shows a strong dependency on the metallicity, which is expected, since it is treated linearly with the abundance of [C II] in the gas. The second main feature of this results is the dependency with the stellar population age. Here we assumed a continuum star formation rate of $20 M_{\odot} \text{ yr}^{-1}$, for the older stellar populations there is a higher amount of heating photons coming from the UV part of the spectrum. This is a result of using a continuum star formation mode, for a given SFR, older populations have more time generating young UV emitting stars. These extra heating photons avoid the cooling of the gas, which decrease the amount of gas in the cold neutral medium, where most of the [C II] emission is produced.

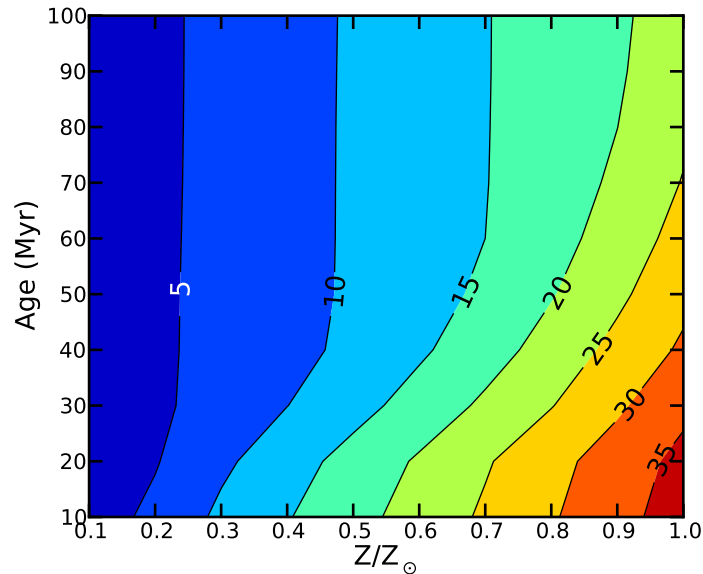


Figure 7.4: Contour plot of the integrated [C II] flux of IOK-1 in mJy km s^{-1} for different simulation conditions. As comparison, our upper limit for integrated flux of IOK-1 is $175 \text{ mJy km s}^{-1}$. The two independent parameters are the stellar population age and the metallicity of the gas. The flux is integrated over the whole area of the cube and in a channel resolution of 500 km s^{-1} around the peak of the emission. The integrated flux is a conservative upper limit for the different parameters. We can see from the contour plot that the [C II] emission is very sensitive to the metallicity of the galaxy, and in a less significant way to the age of the stellar population. The different ages correspond to a different amount of heating photons coming from the young stars, which is critical for the cooling of the gas.

7.1.4 Spectral Resolution

For a Gaussian emission line, with a FWHM of 50 km s^{-1} observed at a channel resolution of 200 km s^{-1} , emission lines will be significantly diluted. In the best case scenario of the line falling completely in one channel, we will recover 38% of the peak flux of the line. This suggests to carry out observations a sufficiently high spectral resolution. E.g. with a line of FWHM of 50 km s^{-1} and a channel resolution of 10 km s^{-1} , we expect to recover 97% of the peak flux of the line.

7.1.5 Atomic Mass Estimation

We use Equation 1 from (Hailey-Dunsheath et al., 2010) to give a rough upper limits to the atomic mass associated with PDRs in our targets (Assuming all [C II] would arise from PDRs). As approach to the PDRs conditions we use the result of Vallini et al. (2013) for the temperature and density in the CNM of Himiko,

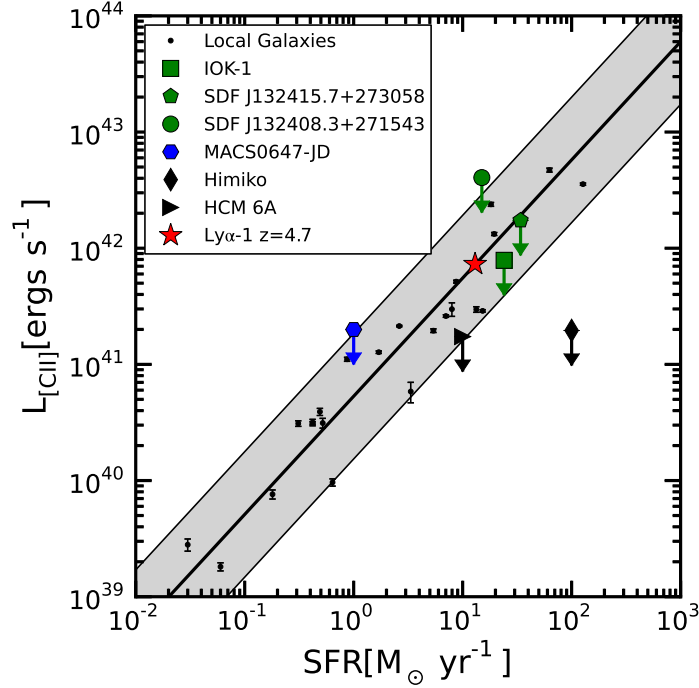


Figure 7.5: Relation of the [C II] luminosity with the UV-derived star formation rate of galaxies. The black solid lines correspond to the relation found by [de Looze et al. \(2011\)](#), with the gray area corresponding to 2σ of the scatter in the relation. The black dots with error bars correspond to the data used to find the relation of [C II]-SFR. The green circle, square and pentagon correspond to the LAEs with the [C II] upper limits presented in this paper assuming the star formation rate estimated from the UV fluxes. The blue hexagon corresponds to the [C II] upper limit of MACS0647-JD with based in the most sensitive setup and the star formation rate estimated from the UV fluxes. The red star corresponds to the LAE detected with ALMA at $z \sim 4.7$ ([Carilli et al., 2013](#)). The black triangle corresponds to the upper limit of the [C II] emission found for HCM-6A by [Kanekar et al. \(2013\)](#). The black diamond corresponds to the upper limit of the [C II] emission found for Himiko by [Ouchi et al. \(2013\)](#).

$n = 5 \times 10^4 \text{ cm}^{-3}$ and $T=250 \text{ K}$. Using our upper limits for [C II] we obtain the following upper limit to the atomic mass: For IOK-1 $M_{\text{HI}} \lesssim 2 \times 10^8 M_{\odot}$, for SDF J132415.7+273058 $M_{\text{HI}} \lesssim 4 \times 10^8 M_{\odot}$, for SDF J132408.3+271543 $M_{\text{HI}} \lesssim 1 \times 10^9 M_{\odot}$ and for MACS0647-JD $M_{\text{HI}} \lesssim 5 \times 10^7 M_{\odot}$.

7.1.6 [C II] - SFR relation

As already mentioned in Chapter 6, the [C II]-SFR is an useful diagnostic whose applicability at high- z is still matter of discussion. Regarding this argument, in Fig. 7.5 is shown the L_{CII} upper limits with the UV-SFR estimated for the targets in GL14 together with upper limits detections for published LAEs ([Carilli & Walter, 2013](#); [Kanekar et al., 2013](#); [Ouchi et al., 2013](#)). The black solid lines corresponds to

the relation found by [de Looze et al. \(2011\)](#), with the gray area corresponding to 2σ scatter in the relation. The upper limits for the [C II] luminosity fall within the scatter of the [C II]-SFR, with the exception of SDF J132408.3+271543, where the upper limit falls above the relation due to the moderate depth of its observations. The detection of the LAE at $z=4.7$ ($\text{Ly}\alpha$ -1) agree very well with the relation found by [de Looze et al. \(2011\)](#) using the UV-SFR estimated by [Ohyama et al. \(2004\)](#). The upper limits for the lensed LAE at $z = 6.56$ HCM 6A and Himiko suggest that LAEs at $z > 6$ could fall below the relation found at low redshift. More observations are needed to clarify if there is an intrinsic difference between the LAEs at $z \sim 4.5$ with the higher redshift population. From a theoretical point of view, the study discussed in the previous chapter suggests that any deviation (more precisely [C II] deficit) from the local [C II]-SFR would imply or modified Kennicutt-Schmidt relation in $z > 6$ galaxies or, alternatively/in addition, might be explained by low gas metallicities.

As a final consideration, it must be noted that the high magnification of MACS0647-JD allows to explore an UV-SFR one order of magnitude lower than the ones of the LAEs, showing the advantage of observing lensed galaxies to cover the intrinsically faint population at high redshift.

7.2 ALMA observations of $z \approx 7$ galaxies

7.2.1 Source selection

The second observation presented in this Chapter relies on an ALMA program targeting a sample of three spectroscopically confirmed galaxies at $6.8 < z < 7.1$. The main goal of the project was to detect them either in the [C II] line and in the continuum.

The observed galaxies are listed in Tab. 7.3. These targets were initially selected as Lyman Break Galaxies through their z -Y dropout ([Vanzella et al., 2011](#); [Ono et al., 2012](#)). All of them have solid spectroscopic confirmations, through the detection of $\text{Ly}\alpha$ with clearly asymmetric profile due to absorption of the blue side by the intervening IGM. The redshift given in Tab. 7.3 refers to that inferred from the peak of the $\text{Ly}\alpha$ emission. This is likely to be significantly in excess (even by about a few 100 km/s) with respect to the real systemic redshift of the sources, because

of the IGM absorption of Ly α . The quoted star formation rates are based on their UV emission, assuming no dust extinction (which however is likely to be very low given the very steep UV continuum [Vanzella et al., 2011](#)). We have also corrected them by adopting the new relation provided by [Kennicutt & Evans \(2012\)](#).¹

Target	redshift (Ly α)	SFR (UV)
BDF-3299	7.109	5.7
BDF-512	7.008	6.0
BDF-46975	6.844	15.4

Table 7.3: List of galaxies observed. The quoted redshift refers to that inferred from Ly α , the star formation rates are based on the UV emission by adopting the new relation provided by [Kennicutt & Evans \(2012\)](#).

7.2.2 [C II] detection in BDF3299

The important achievement of this observational campaign is that [C II] emission is actually detected in a gas clump close to BDF3299 primary galaxy. To better illustrate this scenario, in Fig. 7.6 we show synthetic maps produced with the model presented in Chapter 4 ([Vallini et al., 2013](#)), but tailored to a galaxy at $z = 7.1$ and with the same SFR as BDF3299. The magenta points show the distribution of young hot stars, i.e. what we observe as UV rest-frame continuum emission. The color image shows the distribution of warm ionized gas, which is observed as Ly α emission. The contours show the [C II] emission associated with the neutral gas. Clearly the central galaxy is expected to emit strong UV continuum and Ly α , but being completely photoionized, it does not emit any [C II]. However, very interestingly, the model expects [C II] emission from gas clumps at a few/several kpc from the primary galaxy.

These are satellite gas clumps in the process of accreting onto the primary galaxy, which have survived photoionization, owing their distance from the source of UV photons (and because a significant fraction of UV photons is absorbed internally by the ISM of the primary galaxy). In these systems the [C II] excitation is not expected to primarily originate from in-situ star formation, but as a consequence of soft-UV irradiation from the central primary galaxy. Such [C II] emission in the

¹The MA15 data are still not public, this is the reason why we briefly introduce them without going deep into details. We refer the reader to the upcoming paper by Maiolino et al. 2015 for further details about the data reduction and [C II] maps and spectra.

satellite, accreting gas clumps is expected to be faint, but our deepest observation, the one of BDF3299, does have the sensitivity to detect it.

The map of the [C II] and the resulting spectrum of the observation will be published soon by Maiolino et. al 2015. In this forthcoming paper it will be shown that the emission is fully consistent with the scenario discussed above in which this [C II] emission is associated with a gas cloud accreting onto the primary galaxy and excited by its UV radiation field (Vallini et al., 2013).

In the right panel of Fig. 7.6 we have smoothed the simulation to the angular resolution of the optical (0.5") and ALMA observations. The simulation is not meant, by any means, to exactly reproduce our observations (this would require a huge number of simulated objects with the same full treatment of the IGM, currently beyond our capabilities, and finding the best matching case). However, the figure illustrates that the offset between Y-band emission and [C II] emission is indeed expected to be resolved for various [C II] clumps (and especially for the brightest one) with the angular resolution delivered by our ALMA observation. Lower angular resolution observations would probably hamper the capability of resolving the spatial offset and would probably associate the [C II] emission to the primary UV-Ly α emitting galaxy. The simulation also highlights that more than one [C II] clump may be present around BDF3299, but probably below our detection limit and likely also because of beam dilution. In principle the line width and spatial extension can provide information on the dynamical mass of the blob. Determining a dynamical mass of the [C II] clump detected in the vicinity of BDF3299 is not easy, either because we do not know whether the line width is tracing a rotating system or a velocity dispersion dominated system, and because the [C II] map is only marginally resolved, hence the intrinsic dimension (beam deconvolved) is difficult to estimate. If we assume that the system is rotationally supported and with a radius of about 1.5 kpc, we obtain a rough estimate of the clump dynamical mass of about $2 \times 10^9 M_{\odot} \text{ yr}^{-1}$. If the system is not virialized, then this is actually an upper limit to the dynamical mass. If we adopt a similar analysis to BDF3299, by assuming that the Ly α profile is primarily tracing rotation (i.e. neglecting outflows and velocity dispersion), and assuming that half of Ly α is absorbed by the IGM, then we obtain a rough estimation of the dynamical mass of about $2 \times 10^9 M_{\odot} \text{ yr}^{-1}$. Although all these dynamical mass estimates are very uncertain, they suggest that indeed the [C II] clump is a small satellite of the more massive primary galaxy. For the same reason we cannot exclude that some of the [C II] emission in the clump could be excited by

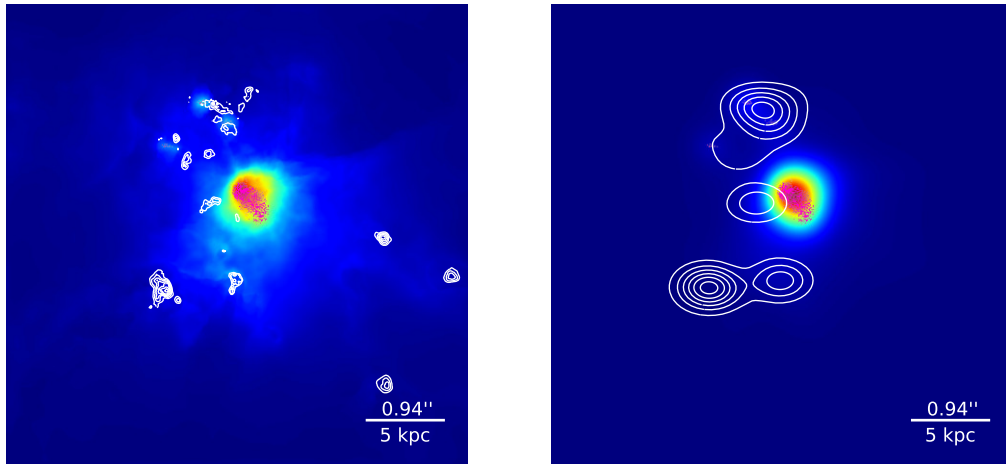


Figure 7.6: Left panel: simulation of a primeval galaxy at $z = 7.1$ with SFR similar to BDF3299. The distribution of ionized gas (traced by $\text{Ly}\alpha$) is shown in colors. The magenta points show the distribution of young stars. The contours show the emission of $[\text{C II}]$ tracing the neutral gas (distributed in clumps orbiting/accreting the primary galaxy). Right panel: same as the left panel in which the image of the ionized gas has been convolved with the angular resolution of the Y-band images ($0.5''$) and the $[\text{C II}]$ map has been convolved with the ALMA beam.

in-situ star formation. Indeed, if we assume that all of the $[\text{C II}]$ emission detected in the $[\text{C II}]$ clump is associated with star formation, by taking the local scaling relations, this would imply a $\text{SFR} = 0.2 - 0.4 M_{\odot} \text{ yr}^{-1}$, i.e. certainly not detectable with the Y-band (UV-restframe) image considered in this work. We finally note that the integrated $[\text{C II}]$ spectrum inferred from the simulation, shown in Fig. 7.7, expects additional narrow emission $[\text{C II}]$ lines emitted from small accreting/satellite clumps illuminated by the primary source. We have tentatively identified narrower ($10\text{-}20 \text{ km/s}$) $[\text{C II}]$ emission sources in the vicinity of BDF3299, but which need to be confirmed with deeper and higher angular resolution observations.

7.2.3 The $[\text{C II}]$ -SFR relation

As extensively discussed in Chapter 6 the $[\text{C II}]$, especially at low- z , is found to be a good tracer of the star formation and the extrapolation at high- z of the $[\text{C II}]$ -SFR relation (de Looze et al., 2011; De Looze et al., 2014) would have implied that, with the sensitivity reached within this study, the $[\text{C II}]$ would have been observed also from the targets presented in Tab. 7.3.

However, the $[\text{C II}]$ line is not detected in any of the three sources at the location of their Y-band emission. Fig. 7.8 shows L_{CII} versus SFR for various classes of

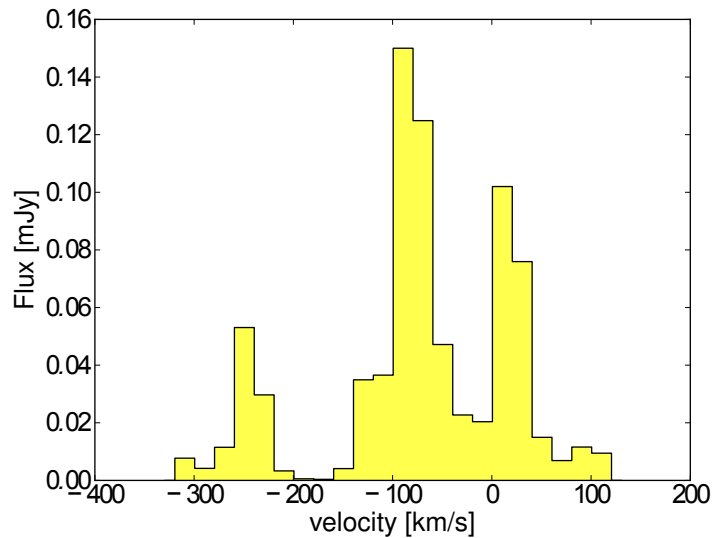


Figure 7.7: Integrated [C II] spectrum from the simulation.

galaxies presented in [De Looze et al. \(2014\)](#). The blue line indicates the relation for local normal star forming and starburst (non-ULIRG) galaxies, with the shaded blue region giving the $\pm 1\sigma$ dispersion. The orange line and hatched region shows the relation and dispersion of local low metallicity galaxies, down to $0.02 Z_{\odot}$. These data have been already presented, with the corresponding metallicity, in [Fig. 6.3](#) (courtesy of I. De Looze) when we investigated theoretically the applicability of the [C II]-SFR at high redshift. The green line and hatched region indicate the relation inferred for high- z galaxies, at $1 < z < 6.5$, but which have $\text{SFR} > 100 M_{\odot} \text{yr}^{-1}$, hence their comparison with the [Tab. 7.3](#) sample which have much lower SFR, should done with care.

Normal galaxies at $z \approx 7$ (i.e. those with $\text{SFR} < 100 M_{\odot} \text{yr}^{-1}$) are indicated with red upper limits. Circles indicate our new observations, while squares are for additional galaxies at $6.8 < z < 11$ ([Ota et al., 2014](#); [Schaerer et al., 2015](#); [González-López et al., 2014](#)). Clearly the bulk of galaxies at $z \sim 7$ (at least those for which a meaningful constraint on L_{CII} has been obtained) have, at a given SFR, a [C II] luminosity significantly lower than observed most local galaxies, even by including the low metallicity ones. However, it is particularly interesting that for BDF3299, which is the galaxy at $z = 7.1$ with the deepest ALMA observation, the 3σ upper limit on the [C II] luminosity is 6 times lower than expected from normal local galaxies, even those at low metallicity. As pointed out in [Chapter 6](#) the [C II]

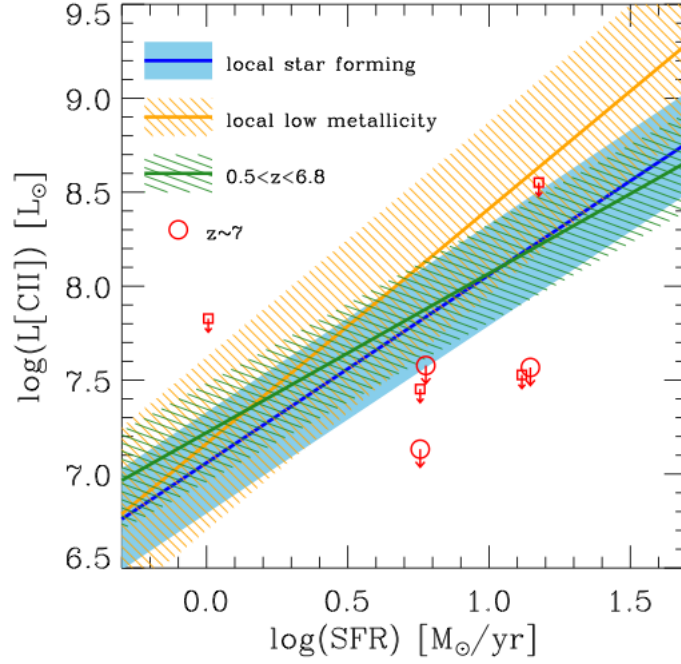


Figure 7.8: [C II] luminosity versus SFR. The blue line shows the relation found by (De Looze et al., 2014) for local star forming galaxies and starbursts (non including ULIRGs), while the shaded region shows the 1σ dispersion. The orange line and hatched region show the relation and dispersion found by De Looze et al. (2014) for local low metallicity dwarfs and irregular. The green line and hatched region show the relation and dispersion found by (De Looze et al., 2014) for high- z galaxies ($z < 6.5$), although all of them with $\text{SFR} > 100 M_{\odot} \text{yr}^{-1}$. The red symbols are the [C II] upper limits for galaxies at $z \approx 7$: circles are our new sources and squares are sources from the literature (Ota et al., 2014; Schaerer et al., 2015; González-López et al., 2014).

line deficit in high redshift normal galaxies could be ascribed to low metallicity.

7.3 Summary

In this Chapter we have discussed two distinct observations in which the use of the theoretical model developed in this Thesis allowed to interpret the data. In both cases the main goal was the search of [C II] emission from $z > 6$ LAEs and LBGs. We summarize the main achievements in what follows:

- The Observation 1 ends up with a non detection in any of the targeted galaxies. For the LAEs the $3\sigma L_{[\text{C II}]}$ upper limit are < 2.05 , < 4.52 and $< 10.52 \times 10^8 L_{\odot}$ for IOK-1, SDF J132415.7+273058 and SDF J132408.3+271543 respectively. Our [C II] upper limits are consistent with the relation of SFR- $L_{[\text{C II}]}$ found by de Looze et al. (2011). The 3σ upper limit in the [C II]

luminosity of MACS0647-JD is $< 5.27 \times 10^7 \times (\mu/15)^{-1} L_{\odot}$. However, we point out that the sensitivity reached with PdBI and CARMA in Observation 1 is shallower than that of Observation 2, and so they are the upper limits.

- We present the results of simulations supporting the brightest component of the [C II] line having a width of the order of 50 km s^{-1} . Here we want to emphasize the necessity of resolving such emission lines in future ALMA observations, to not lose signal-to-noise ratio, by selecting a channel resolution that is too low.
- Simulations are already showing us that the task of detecting [C II] in high redshift galaxies is going to be difficult even with ALMA, as confirmed by the recent sensitive non-detection of Himiko by [Ouchi et al. \(2013\)](#). Accordingly to our IOK-1 simulations, a key parameter for the [C II] emission in LAEs is the metallicity, as we discussed in Sect. 7.1.3.
- If these simulations were applicable to all high redshift LAEs, we should first try to detect [C II] in the LAEs with the highest metallicity. Estimating the metallicity of LAEs at high redshift is not an easy task, however, [Cowie et al. \(2011\)](#) found that for the sample of LAEs discovered by the Galaxy Evolution Explorer (GALEX) grism in the redshift range of $z = 0.195 - 0.44$, there is an anti-correlation of the equivalent width of the $H\alpha$ emission line with metallicity. Higher $EW(H\alpha)$ sources all have lower metallicities, bluer colors, smaller sizes, and less extinction. [Cowie et al. \(2011\)](#) also found a broad general trend that for higher $EW(H\alpha)$, the $EW(Ly\alpha)$ is also higher. If we assume that these relations are valid for the LAEs at high redshift, and that the goal is to observe the LAE with the highest metallicity possible, it may be best to target the brightest LAE in the UV but with the lowest $Ly\alpha$ equivalent width. Lyman-break galaxies with $Ly\alpha$ detection may thus be ideal targets for [C II] searches at high redshift.
- The Observation 2, carried out with ALMA ends up with a non-detection of the [C II] line in any of the three LAEs (BDF-3299 at $z = 7.109$, BDF-512 at $z = 7.008$, and BDF-46975 at $z = 6.844$) at the location of their Y-band emission.
- The important achievement of this observational campaign is that [C II] emission is actually detected in a gas clump close to BDF3299 primary galaxy.

This is in agreement with the theoretical prediction provided by our model (see Chapter 4) either if we consider only the contribution of the diffuse neutral gas and if we include the proper treatment of the emission from PDRs and diffuse gas and we take into account of the effect of the CMB on the radiative transfer of the line luminosity (see Chapter 6)

Conclusions 8

THE ADVENT of the Atacama Large Millimeter/sub-millimeter Array, the most powerful sub-millimeter interferometer on the Earth, has opened a new window on the high redshift Universe. One of the major goals of ALMA is to observe a great number of atomic and molecular lines arising from the neutral, ionized and molecular gas in the interstellar medium of galaxies placed at the end of reionization epoch. This will help to shed light on the internal properties of sources that appeared within the first billion years of the cosmic history. Until now, we have witnessed to the outcome of the first two ALMA observing cycles and, as it usually happens in the Science, while the detections can be used to answer many questions, new open issues have emerged. For instance, the observation of the [C II] $158\ \mu\text{m}$ transition, the most luminous among the metal cooling lines, from MilkyWay-like galaxies at $z > 6$ seems more difficult than expected from the mere extrapolation at high- z of local luminosities. What do we learn from this? What are the physical conditions within the ISM of these sources? This Thesis answers these questions and it helps to draw out from the ALMA observations a complete picture of the physics of the ISM.

We construct physically motivated models that allow to predict the FIR line luminosities and relate them to other quantities: the SFR and the metallicity of the galaxies. We started with a semi-analytical approach, explained in Chapter 3, to evaluate the fraction of molecular hydrogen in a sample of simulated Lyman Alpha Emitters at redshift $z = 5.7, 6.6$. We then focus the attention on a single galaxy extracted from a cosmological simulation evolved until $z \approx 6.6$. The hydrodynamical simulation was carried out with GADGET-2 and then further treated with a full UV

ionizing radiative transfer performed with LICORICE. The spatial resolution reached (≈ 60 pc) allows to catch the internal properties of the galaxy. As shown in the Chapter 4, we implement on top of the simulation a sub-grid model describing the thermodynamical equilibrium of the diffuse gas in the ISM and hence the luminosities of several metal cooling lines ([C II], [O I], and [N II]). By knowing the proper velocities of the gas within the ISM we have been able to produce synthetic spectra that have been tested against PdBI and ALMA observations.

The diffuse gas model described in the Chapter 4 has been further implemented by searching for the locations of the MCs within the galaxy, and by calculating FIR line emission from the photodissociation regions. To do that, as explained in the Chapter 5, we coupled the simulation with UCL_PDR. As a final expansion of the work, we explored the relation between the [C II] luminosity and the SFR. This part of the Thesis is presented in the Chapter 6. The main results obtained from all these works, which have formed my PhD Thesis, are now summarized:

The molecular content in high- z galaxies

With the semi-analytical model outlined in Chapter 3 we provide a global estimate of the molecular hydrogen fraction in $z \approx 5.7, 6.6$ Lyman Alpha Emitters. The value of f_{H_2} peaks and ranges between 0.5 – 0.9 for intermediate mass LAEs with $M_* \approx 10^{9-10} M_\odot$, decreasing for both smaller and larger galaxies; this trend also holds at $z \approx 6.6$. We find a decreasing trend of the mean molecular fraction with the redshift that can be explained with the lower abundance of dust in the ISM with increasing z . We translate the predicted mass of the molecular hydrogen into the CO luminosity, that is the most widely used tracer for the molecular gas. We find that L_{CO} scales with L_α for the two redshifts considered making the most luminous LAEs the most promising objects to be targeted with ALMA. However, even an optimistic ULIRG-like conversion factor between M_{H_2} and the CO luminosity ($\alpha = 0.8 M_\odot / [\text{K km s}^{-1} \text{ pc}^2]$) drives to the conclusion that only about 1-2% of the $z \approx 5.7$ LAEs could be detectable in CO(6–5) with an integration time of 5-10 hours respectively. Our results at $z \approx 6.6$ are even more pessimistic; none of the LAEs would be detectable in CO.

These conclusions, drawn out from this semi-analytical model, have been confirmed in the subsequent work. As shown in Chapter 5, we coupled a zoomed *single*

galaxy simulation with a physically motivated model that allows to locate molecular clouds and photodissociation regions within the ISM. The molecular clouds, constituted by dense ($n_{\text{MC}} \sim 10^2 - 10^4 \text{ cm}^{-3}$) and small ($r_{\text{MC}} \sim \text{pc}$) clumps, lies predominantly at the center of the galaxy or in small overdense regions, probably accreting satellites, at the periphery of the galaxy. The synthetic spectrum achieved shows a maximum flux density of \approx tens of μJy (depending on the metallicity) that would be very hardly detectable even with the full ALMA capabilities hence confirming the trend found with the semin-analytical model.

The predicted intensity of the CO(6-5) arising from the MCs is consistent with a CO-to-H₂ conversion factor $\alpha \simeq 2 M_{\odot}/[\text{K km s}^{-1} \text{ pc}^2]$ and the integrated flux is in agreement with the predictions provided by [Muñoz & Furlanetto \(2013\)](#).

Multiphase contribution to the FIR lines

Our study of the luminosity of metal cooling lines from high- z galaxies has been carried out with of an high-resolution galaxy simulation coupled with a sub-grid model that describes the thermodynamical equilibrium of the diffuse neutral gas in the interstellar medium. To achieve the emission from PDRs we coupled the simulation with UCL_PDR code. We find that warm neutral medium lies in overdense regions located sufficiently far from the star forming region of the simulated galaxy where the strong ionizing UV field does not allow the presence of neutral gas. Cold gas resides instead in more dense clumps and, as pointed out in the Chapter 4, accounts for the major fraction of the [C II] and [O I] emission from the diffuse gas. However, as pointed out in Chapter 6, the transmitted flux arising from the CNM is strongly attenuated by the fact that the spin temperature of the [C II] transition is close to that of the CMB. As a consequence, the transmitted flux is only $\zeta \approx 0.1 - 0.2$. This issue does not affect the PDR emission where the T_{s} is well above the T_{CMB} and $\zeta \approx 0.8 - 1.0$. Without the attenuation of the CNM luminosity, we obtain the fraction of the flux arising from the diffuse phase $F_{\text{diff}}/F_{\text{tot}} = 0.05 - 0.45$ as function of the star formation rate. Regardless the metallicity profile, the ratio increases from $\text{SFR} = 1.0 M_{\odot} \text{ yr}^{-1}$ to $\text{SFR} = 1.0 M_{\odot} \text{ yr}^{-1}$ when it reaches the peak, and then it decreases with increasing SFR. At high- z , $F_{\text{diff}}/F_{\text{tot}}$ drops to $F_{\text{diff}}/F_{\text{tot}} = 0.002 - 0.1$ because of the CNM attenuation due to the increased CMB temperature.

FIR line emission: spectral features

With our simulation of the $z \approx 6.6$ galaxy we produce the observed [C II] spectrum as we have enough resolution to recover the proper velocity of the gas within the ISM. We achieve a multi peak spectrum produced by the overdense clumps at the periphery of the galaxy. These are the location of the CNM and also of a small fraction of the PDRs. The typical FWHM of the peaks is of order of $\approx 50 \text{ km s}^{-1}$. We find that the, after correcting for the CMB effect on the line luminosity, the main peak of the emission (produced by the PDRs) lies at center of the galaxy. The metallicity is a fundamental parameter in our model, and we have shown that it affects the spectrum so that the lower is $\langle Z \rangle$ the lower is the expected flux density of the various lines. To distribute metals in the simulated galaxy we exploit the correlation between Z and the overdensity and the natural consequence is that regions where MCs are located (i.e. the most over dense in the simulation) are more metal enriched than the rest of the galaxy. The important implication of this result is that metallicity measurements through FIR lines that trace PDRs deliver upper limits on the average metallicity of the galaxy.

The [C II]-SFR relation

By adopting our FIR line emission model we have investigated whether the [C II]-SFR relation observed in local galaxies applies at high- z .

The main conclusion is that we reproduces the corresponding relation found in local dwarfs remarkably well. Any deviation at high- z from the local [C II]-SFR would imply (i) a modified Kennicutt-Schmidt relation in $z > 6$ galaxies and/or (ii) low metallicities within the galaxy ISM.

Through the work we neglected the possible effect of stellar feedback (i.e. photo-evaporation, radiation pressure, H II thermal pressure) on molecular clouds. Broadly speaking, these effects should act to reduce the mass of the molecular gas. On the other hand, the expansion of H II regions might have either a positive effect, by triggering new star formation, or a negative effect, by dispersing the surrounding cloud. Our study allows to argue that a [C II] deficit in $z \sim 6 - 7$ galaxies, if confirmed by deeper observations, would favor a scenario in which star formation in early galaxies blows the molecular gas apart, reducing the amount of material from which most of the [C II] emission arises, i.e. PDRs.

Finally, we note that the MC density distribution may play a role. For instance,

molecular clouds characterized by densities 10 times higher (lower), for a fixed gas metallicity (e.g. $\log(Z/Z_{\odot}) = -1.5$), would result into a [C II] emissivity 5 times higher (20 times lower) than found in our fiducial model. Although we consider such large variations unlikely, at present we cannot exclude that a shift in the mean MC density plays some role in the interpretation of the results.

Intepreting [C II] observations from high redshift

The search of the FIR lines from high- z galaxies is now entering in a golden era thanks to the capabilities of sub-millimeter interferometers such as PdBI and to the unprecedented sensitivities reached by ALMA. Our model represents a helpful tool to understand the physical conditions of the gas producing these lines and it has been used as theoretical support in two observational campaigns. The first one, aim at detecting the [C II] line emission from LAEs and LBGs at $z > 6.5$ with PdBI and CARMA, the second one focused on an ALMA program targeting a sample of three spectroscopically confirmed galaxies at $6.8 < z < 7.1$. The main goal of the project was to detect them either in the [C II] line and in the continuum. Our simulations suggest that the difficulties faced with PdBI and CARMA are due either to the unexpected (at the time of the proposal) narrowness of the [C II] line (FWHM ≈ 50 km/s) and to the low metallicity of these objects. From the second observation we strongly support with our theoretical model the detection of a displaced [C II] emission from the location of the Ly α emission. This is indeed expected by our high- z simulations that show many emitting clumps, constituted by neutral gas and dense PDRs, around the central ionized region of the galaxy.

8.1 Novelty of the Thesis and future prospects

The work presented in this Thesis has opened a new fruitful route to link the theoretical modeling aiming at describing the formation and the properties of the first galaxies that appeared in the Universe, with the observations of far infrared emission lines arising from their ISM. We built for the first time a tool that can reproduce the FIR lines luminosity that one would observe from a galaxy at a given redshift with given SFR and metallicity. We are also able to construct high resolution synthetic spectra and maps directly comparable with the ones achievable with ALMA or other sub-millimeter facilities.

Moreover, our study on the reliability of the [C II]-SFR relation at high- z will be also employed in theoretical works aiming at evaluating the expected signal in [C II]-intensity mapping experiments. The line intensity mapping is a technique to access high- z galaxies below the detection limit without losing redshift information. Optimistically, it only collects radiation from galaxies in a selected redshift range, as the spurious flux due to foregrounds, contaminating radiation and noise can be in principle removed or suppressed. By applying the [C II]-SFR relation inferred from our work we can very precisely predict the [C II] flux arising from galaxies with very low SFRs ($< 1.0 M_{\odot} \text{ yr}^{-1}$) that makes them very faint and hence unresolved (see Yue et al. 2015, submitted).

However, many other physical processes can be added to our model. Just to mention few of them, we are currently working the effect of the AGN activity on the line luminosities. This will be achieved by running single galaxy simulation, fully implemented with a radiative transfer calculation that takes into account of the presence of a super massive black hole at the center of the galaxy. Then, we will couple the simulation with X-ray Dominated Regions (XDR) codes able to reproduce the effect of the X-rays on FIR lines such as high-J CO rotational transition. Furthermore we are planning to self consistently consider the photoionization feedback on the molecular clouds. This effect could affect not only the line intensities but also the shape of the spectrum quenching the central peak of the emission.

These are just few examples regarding the new pieces that we are adding to the complex puzzle of modeling the interstellar medium of high redshift galaxies. In the forthcoming years ALMA full capability observations, the upcoming Square Kilometer Array and the future advent of JWST will represent a breakthrough in our understanding of the first billion year of the cosmic history but they will surely open new exciting questions. Theoretical models, such the ones presented in this work, will then face the challenge of including increasingly more sophisticated ingredients to describe the marvelous complexity of the Universe.

Bibliography

- Baek S., Di Matteo P., Semelin B., Combes F., Revaz Y., 2009, *A&A*, 495, 389
- Baek S., Ferrara A., Semelin B., 2012, *MNRAS*, 423, 774
- Bakes E. L. O., Tielens A. G. G. M., 1994, *ApJ*, 427, 822
- Barkana R., Loeb A., 2001, *Phys. Rep.*, 349, 125
- Bayet E., Gerin M., Phillips T. G., Contursi A., 2009, *MNRAS*, 399, 264
- Bell T. A., Viti S., Williams D. A., 2007, *MNRAS*, 378, 983
- Bell T. A., Viti S., Williams D. A., Crawford I. A., Price R. J., 2005, *MNRAS*, 357, 961
- Bertoldi F. et al., 2003, *A&A*, 409, L47
- Bianchi S., Schneider R., 2007, *MNRAS*, 378, 973
- Bigiel F., Leroy A., Walter F., Brinks E., de Blok W. J. G., Madore B., Thornley M. D., 2008, *AJ*, 136, 2846
- Bisbas T. G., Wünsch R., Whitworth A. P., Hubber D. A., Walch S., 2011, *ApJ*, 736, 142
- Black J. H., 1981, *MNRAS*, 197, 553
- Bolatto A. D., Wolfire M., Leroy A. K., 2013, *ARA&A*, 51, 207
- Bolton A. S., Treu T., Koopmans L. V. E., Gavazzi R., Moustakas L. A., Burles S., Schlegel D. J., Wayth R., 2008, *ApJ*, 684, 248

- Boselli A., Gavazzi G., Lequeux J., Pierini D., 2002, *A&A*, 385, 454
- Bouwens R. J. et al., 2011, *ApJ*, 737, 90
- Bouwens R. J. et al., 2004, *ApJ*, 616, L79
- Bromm V., Yoshida N., 2011, *ARA&A*, 49, 373
- Calzetti D., Armus L., Bohlin R. C., Kinney A. L., Koornneef J., Storchi-Bergmann T., 2000, *ApJ*, 533, 682
- Carilli C., Walter A., 2013, arxiv
- Carilli C. L., Dwarakanath K. S., Goss W. M., 1998, *ApJ*, 502, L79
- Carilli C. L., Riechers D., Walter F., Maiolino R., Wagg J., Lentati L., McMahon R., Wolfe A., 2013, *ApJ*, 763, 120
- Carniani S. et al., 2013, *A&A*, 559, A29
- Castellano M. et al., 2010, *A&A*, 524, A28
- Ciardi B., Ferrara A., 2005, *Space Sci. Rev.*, 116, 625
- Coe D. et al., 2013, *ApJ*, 762, 32
- Combes F. et al., 2012, *A&A*, 538, L4
- Coppin K. E. K. et al., 2012, *MNRAS*, 427, 520
- Cormier D. et al., 2012, *A&A*, 548, A20
- Cowie L. L., Barger A. J., Hu E. M., 2011, *ApJ*, 738, 136
- Cowie L. L., Hu E. M., 1998, *AJ*, 115, 1319
- Cox P. et al., 2011, *ApJ*, 740, 63
- Cox P. et al., 2002, *A&A*, 387, 406
- da Cunha E. et al., 2013, *ApJ*, 766, 13
- Dale J. E., Bonnell I. A., Clarke C. J., Bate M. R., 2005, *MNRAS*, 358, 291
- Dalgarno A., McCray R. A., 1972, *ARA&A*, 10, 375

- Dayal P., Ferrara A., 2011, MNRAS, 417, L41
- Dayal P., Ferrara A., Gallerani S., 2008, MNRAS, 389, 1683
- Dayal P., Ferrara A., Saro A., 2010, MNRAS, 402, 1449
- Dayal P., Ferrara A., Saro A., Salvaterra R., Borgani S., Tornatore L., 2009, MNRAS, 400, 2000
- Dayal P., Maselli A., Ferrara A., 2011, MNRAS, 410, 830
- De Breuck C., Maiolino R., Caselli P., Coppin K., Hailey-Dunsheath S., Nagao T., 2011, A&A, 530, L8
- De Breuck C. et al., 2014, A&A, 565, A59
- de Looze I., Baes M., Bendo G. J., Cortese L., Fritz J., 2011, MNRAS, 416, 2712
- De Looze I. et al., 2014, A&A, 568, A62
- Decarli R. et al., 2014, ApJ, 782, L17
- Decarli R. et al., 2012, ApJ, 752, 2
- Dijkstra M., Lidz A., Wyithe J. S. B., 2007, MNRAS, 377, 1175
- Dijkstra M., Mesinger A., Wyithe J. S. B., 2011, MNRAS, 414, 2139
- Dobbs C. L., 2008, MNRAS, 391, 844
- Downes D., Solomon P. M., 1998, ApJ, 507, 615
- Draine B., 2010, *Physics of the Interstellar and Intergalactic Medium*, Princeton Series in Astrophysics. Princeton University Press
- Draine B. T., Bertoldi F., 1996, ApJ, 468, 269
- Draine B. T., Lee H. M., 1984, ApJ, 285, 89
- Dunlop J. S., 2013, in *Astrophysics and Space Science Library*, Vol. 396, *Astrophysics and Space Science Library*, Wiklind T., Mobasher B., Bromm V., eds., p. 223
- Dwek E., Galliano F., Jones A. P., 2007, *Nuovo Cimento B Serie*, 122, 959

- Einstein A., 1916, *Annalen der Physik*, 354, 769
- Fangano A. P. M., Ferrara A., Richter P., 2007, *MNRAS*, 381, 469
- Ferkinhoff C. et al., 2011, *ApJ*, 740, L29
- Ferrara A., Loeb A., 2013, *MNRAS*, 431, 2826
- Ferrara A., Pettini M., Shchekinov Y., 2000, *MNRAS*, 319, 539
- Field G. B., Goldsmith D. W., Habing H. J., 1969, *ApJ*, 155, L149
- Finkelstein S. L. et al., 2013, *Nature*, 502, 524
- Finkelstein S. L., Rhoads J. E., Malhotra S., Grogin N., 2009, *ApJ*, 691, 465
- Finkelstein S. L., Rhoads J. E., Malhotra S., Pirzkal N., Wang J., 2007, *ApJ*, 660, 1023
- Fixsen D. J., 2009, *ApJ*, 707, 916
- Gallerani S., Ferrara A., Fan X., Choudhury T. R., 2008, *MNRAS*, 386, 359
- Gallerani S. et al., 2012, *A&A*, 543, A114
- Galliano F., Dwek E., Chianial P., 2008, *ApJ*, 672, 214
- Genzel R. et al., 2011, *ArXiv e-prints*
- Glover S. C. O., Clark P. C., 2012, *MNRAS*, 421, 116
- Glover S. C. O., Federrath C., Mac Low M.-M., Klessen R. S., 2010, *MNRAS*, 404, 2
- Gnedin N. Y., 2000, *ApJ*, 535, 530
- Gnedin N. Y., Kravtsov A. V., 2010, *ApJ*, 714, 287
- Gong Y., Cooray A., Silva M., Santos M. G., Bock J., Bradford C. M., Zemcov M., 2012, *ApJ*, 745, 49
- González-López J. et al., 2014, *ApJ*, 784, 99
- Gould R. J., Gold T., Salpeter E. E., 1963, *ApJ*, 138, 408

- Greve T. R. et al., 2005, MNRAS, 359, 1165
- Greve T. R., Sommer-Larsen J., 2008, A&A, 480, 335
- Haardt F., Madau P., 1996, ApJ, 461, 20
- Habing H. J., 1968, Bull. Astron. Inst. Netherlands, 19, 421
- Hailey-Dunsheath S., Nikola T., Stacey G. J., Oberst T. E., Parshley S. C., Benford D. J., Staguhn J. G., Tucker C. E., 2010, ApJ, 714, L162
- Haworth T. J., Harries T. J., 2012, MNRAS, 420, 562
- Hayes M. et al., 2014, ApJ, 782, 6
- Hayes M., Östlin G., Mas-Hesse J. M., Kunth D., 2009, AJ, 138, 911
- Heiles C., Troland T. H., 2003, ApJ, 586, 1067
- Hennabelle P., Chabrier G., 2011, ApJ, 743, L29
- Hennabelle P., Chabrier G., 2013, ApJ, 770, 150
- Hennabelle P., Falgarone E., 2012, A&A Rev., 20, 55
- Herrera-Camus R. et al., 2014, ArXiv e-prints
- Hirashita H., Ferrara A., 2005, MNRAS, 356, 1529
- Hollenbach D., McKee C. F., 1979, ApJS, 41, 555
- Hollenbach D., McKee C. F., 1989, ApJ, 342, 306
- Hollenbach D., Salpeter E. E., 1971, ApJ, 163, 155
- Hollenbach D. J., Tielens A. G. G. M., 1999, Reviews of Modern Physics, 71, 173
- Hu E. M., Cowie L. L., Barger A. J., Capak P., Kakazu Y., Trouille L., 2010, ApJ, 725, 394
- Hu E. M., Cowie L. L., McMahon R. G., Capak P., Iwamuro F., Kneib J.-P., Maihara T., Motohara K., 2002, ApJ, 568, L75
- Iye M. et al., 2006, Nature, 443, 186

- Jiang L. et al., 2013, *ApJ*, 772, 99
- Jura M., 1975, *ApJ*, 197, 575
- Kainulainen J., Tan J. C., 2013, *A&A*, 549, A53
- Kanekar N., Wagg J., Ram Chary R., Carilli C. L., 2013, *ApJ*, 771, L20
- Kapala M. J. et al., 2015, *ApJ*, 798, 24
- Kashikawa N. et al., 2006, *ApJ*, 648, 7
- Kashikawa N. et al., 2011, *ApJ*, 734, 119
- Keating L. C., Haehnelt M. G., Becker G. D., Bolton J. S., 2014, *MNRAS*, 438, 1820
- Kennicutt R. C., Evans N. J., 2012, *ARA&A*, 50, 531
- Kennicutt, Jr. R. C., 1998, *ARA&A*, 36, 189
- Kim W.-T., Ostriker E. C., 2002, *ApJ*, 570, 132
- Kim W.-T., Ostriker E. C., Stone J. M., 2003, *ApJ*, 599, 1157
- Klessen R. S., Glover S. C. O., 2014, *ArXiv e-prints*
- Kobayashi M. A. R., Totani T., Nagashima M., 2007, *ApJ*, 670, 919
- Kobayashi M. A. R., Totani T., Nagashima M., 2010, *ApJ*, 708, 1119
- Komatsu E. et al., 2009, *ApJS*, 180, 330
- Komatsu E. et al., 2011, *ApJS*, 192, 18
- Kramer C. et al., 2013, *A&A*, 553, A114
- Krumholz M. R., Matzner C. D., McKee C. F., 2006, *ApJ*, 653, 361
- Krumholz M. R., McKee C. F., 2005, *ApJ*, 630, 250
- Krumholz M. R., McKee C. F., Tumlinson J., 2008, *ApJ*, 689, 865
- Krumholz M. R., McKee C. F., Tumlinson J., 2009, *ApJ*, 693, 216

- Lai K., Huang J.-S., Fazio G., Cowie L. L., Hu E. M., Kakazu Y., 2007, *ApJ*, 655, 704
- Langer W. D., Pineda J. L., Velusamy T., 2014, *A&A*, 564, A101
- Lehner N., Wakker B. P., Savage B. D., 2004, *ApJ*, 615, 767
- Leitherer C. et al., 1999, *APJS*, 123, 3
- Leroy A. K. et al., 2009, *ApJ*, 702, 352
- Lidz A., Furlanetto S. R., Oh S. P., Aguirre J., Chang T.-C., Doré O., Pritchard J. R., 2011, *ApJ*, 741, 70
- Linde A. D., 1982, *Physics Letters B*, 116, 335
- Mac Low M.-M., Ferrara A., 1999, *ApJ*, 513, 142
- Maiolino R. et al., 2005, *A&A*, 440, L51
- Malhotra S., Rhoads J. E., Finkelstein S. L., Hathi N., Nilsson K., McLinden E., Pirzkal N., 2011, *ArXiv e-prints*
- Malhotra S. et al., 2005, *ApJ*, 626, 666
- Mapelli M., Ferrara A., Pierpaoli E., 2006, *MNRAS*, 369, 1719
- Mathis J. S., Rumpl W., Nordsieck K. H., 1977, *ApJ*, 217, 425
- Matsuda Y. et al., 2005, *ApJ*, 634, L125
- McDowell M. R. C., 1961, *The Observatory*, 81, 240
- McGreer I., Mesinger A., D'Odorico V., 2014, *ArXiv e-prints*
- McKee C. F., Krumholz M. R., 2010, *ApJ*, 709, 308
- McKee C. F., Ostriker E. C., 2007, *ARA&A*, 45, 565
- McKee C. F., Ostriker J. P., 1977, *ApJ*, 218, 148
- McLure R. J. et al., 2011, *MNRAS*, 418, 2074
- Meijerink R., Spaans M., 2005, *A&A*, 436, 397

- Mellema G., Arthur S. J., Henney W. J., Iliev I. T., Shapiro P. R., 2006, *ApJ*, 647, 397
- Mortlock D. J. et al., 2011, *Nature*, 474, 616
- Muñoz J. A., Furlanetto S. R., 2013, *MNRAS*, 435, 2676
- Murray N., 2011, *ApJ*, 729, 133
- Nagamine K., Wolfe A. M., Hernquist L., 2006, *ApJ*, 647, 60
- Nagao T., Maiolino R., De Breuck C., Caselli P., Hatsukade B., Saigo K., 2012, *A&A*, 542, L34
- Narayanan D., Krumholz M., Ostriker E. C., Hernquist L., 2011, *MNRAS*, 418, 664
- Narayanan D., Krumholz M. R., Ostriker E. C., Hernquist L., 2012, *MNRAS*, 421, 3127
- Nilsson K. K., Tapken C., Møller P., Freudling W., Fynbo J. P. U., Meisenheimer K., Laursen P., Östlin G., 2009, *A&A*, 498, 13
- Norman M. L., Paschos P., Abel T., 1998, *Mem. Soc. Astron. Italiana*, 69, 455
- Nozawa T., Kozasa T., Habe A., Dwek E., Umeda H., Tominaga N., Maeda K., Nomoto K., 2007, *ApJ*, 666, 955
- Nozawa T., Kozasa T., Umeda H., Maeda K., Nomoto K., 2003, *ApJ*, 598, 785
- Obreschkow D., Heywood I., Klöckner H.-R., Rawlings S., 2009, *ApJ*, 702, 1321
- Ohyama Y., Taniguchi Y., Shioya Y., 2004, *AJ*, 128, 2704
- Omont A., 2007, *Reports on Progress in Physics*, 70, 1099
- Omukai K., 2000, *ApJ*, 534, 809
- Ono Y. et al., 2012, *ApJ*, 744, 83
- Östlin G. et al., 2014, *ApJ*, 797, 11
- Östlin G., Hayes M., Kunth D., Mas-Hesse J. M., Leitherer C., Petrosian A., Atek H., 2009, *AJ*, 138, 923

- Ostriker E. C., Stone J. M., Gammie C. F., 2001, *ApJ*, 546, 980
- Ota K. et al., 2014, *ApJ*, 792, 34
- Ouchi M. et al., 2013, *ApJ*, 778, 102
- Ouchi M. et al., 2009, *ApJ*, 696, 1164
- Ouchi M. et al., 2008, *ApJS*, 176, 301
- Ouchi M. et al., 2010, *ApJ*, 723, 869
- Padoan P., 1995, *MNRAS*, 277, 377
- Padoan P., Federrath C., Chabrier G., Evans, II N. J., Johnstone D., Jørgensen J. K., McKee C. F., Nordlund Å., 2013, *ArXiv e-prints*
- Padoan P., Nordlund Å., 2011, *ApJ*, 741, L22
- Padovani P., Matteucci F., 1993, *ApJ*, 416, 26
- Palla F., Salpeter E. E., Stahler S. W., 1983, *ApJ*, 271, 632
- Pallottini A., Ferrara A., Gallerani S., Salvadori S., D'Odorico V., 2014, *ArXiv e-prints*
- Parkin T. J. et al., 2013, *ApJ*, 776, 65
- Petitjean P., Pécontal E., Valls-Gabaud D., Chariot S., 1996, *Nature*, 380, 411
- Pineda J. L., Langer W. D., Goldsmith P. F., 2014, *A&A*, 570, A121
- Pineda J. L., Langer W. D., Velusamy T., Goldsmith P. F., 2013, *A&A*, 554, A103
- Pirzkal N., Malhotra S., Rhoads J. E., Xu C., 2007, *ApJ*, 667, 49
- Planck Collaboration et al., 2014, *A&A*, 571, A11
- Planck Collaboration et al., 2013, *ArXiv e-prints*
- Planck Collaboration et al., 2015, *ArXiv e-prints*
- Postman M. et al., 2012, *ApJS*, 199, 25
- Press W. H., Schechter P., 1974, *ApJ*, 187, 425

- Riechers D. A., 2011, ArXiv e-prints
- Riechers D. A. et al., 2013, *Nature*, 496, 329
- Riechers D. A. et al., 2014, *ApJ*, 796, 84
- Riechers D. A., Hodge J., Walter F., Carilli C. L., Bertoldi F., 2011, *ApJ*, 739, L31
- Röllig M. et al., 2007, *A&A*, 467, 187
- Salvaterra R., Ferrara A., Dayal P., 2011, *MNRAS*, 414, 847
- Santos M. R., Ellis R. S., Kneib J.-P., Richard J., Kuijken K., 2004, *ApJ*, 606, 683
- Sargsyan L. et al., 2012, *ApJ*, 755, 171
- Saro A., Borgani S., Tornatore L., Dolag K., Murante G., Biviano A., Calura F., Charlot S., 2006, *MNRAS*, 373, 397
- Schaerer D., Boone F., Zamojski M., Staguhn J., Dessauges-Zavadsky M., Finkelstein S., Combes F., 2015, *A&A*, 574, A19
- Sheth R. K., Tormen G., 1999, *MNRAS*, 308, 119
- Shimasaku K. et al., 2006, *PASJ*, 58, 313
- Shull J. M., van Steenberg M. E., 1985, *ApJ*, 298, 268
- Solomon P. M., Rivolo A. R., Barrett J., Yahil A., 1987, *ApJ*, 319, 730
- Solomon P. M., Vanden Bout P. A., 2005, *ARA&A*, 43, 677
- Spaans M., 1996, *A&A*, 307, 271
- Springel V., 2005, *MNRAS*, 364, 1105
- Springel V., Hernquist L., 2003, *MNRAS*, 339, 312
- Springel V., Yoshida N., White S. D. M., 2001, *New A*, 6, 79
- Stacey G. J., Geis N., Genzel R., Lugten J. B., Poglitsch A., Sternberg A., Townes C. H., 1991, *ApJ*, 373, 423
- Steidel C. C., Adelberger K. L., Shapley A. E., Pettini M., Dickinson M., Giavalisco M., 2000, *ApJ*, 532, 170

- Steidel C. C., Giavalisco M., Dickinson M., Adelberger K. L., 1996, *AJ*, 112, 352
- Sturm E. et al., 2010, *A&A*, 518, L36
- Sutherland R. S., Dopita M. A., 1993, *ApJS*, 88, 253
- Tacconi L. J. et al., 2006, *ApJ*, 640, 228
- Taniguchi Y. et al., 2005, *PASJ*, 57, 165
- Tanvir N. R. et al., 2009, *Nature*, 461, 1254
- Tasker E. J., 2011, *ApJ*, 730, 11
- Tasker E. J., Tan J. C., 2009, *ApJ*, 700, 358
- Tasker E. J., Wadsley J., Pudritz R., 2015, *ArXiv e-prints*
- Tielens A. G. G. M., Hollenbach D., 1985, *ApJ*, 291, 722
- Todini P., Ferrara A., 2001, *MNRAS*, 325, 726
- Tornatore L., Borgani S., Dolag K., Matteucci F., 2007, *MNRAS*, 382, 1050
- Tornatore L., Borgani S., Viel M., Springel V., 2010, *MNRAS*, 402, 1911
- Valiante R., Matteucci F., Recchi S., Calura F., 2009, *New A*, 14, 638
- Vallini L., Dayal P., Ferrara A., 2012, *MNRAS*, 421, 3266
- Vallini L., Gallerani S., Ferrara A., Baek S., 2013, *MNRAS*
- van den Hoek L. B., Groenewegen M. A. T., 1997, *A&AS*, 123, 305
- van Dishoeck E. F., Black J. H., 1988, *ApJ*, 334, 771
- Vanzella E. et al., 2011, *ApJ*, 730, L35
- Vasta M., Barlow M. J., Viti S., Yates J. A., Bell T. A., 2010, *MNRAS*, 404, 1910
- Vazquez-Semadeni E., 1994, *ApJ*, 423, 681
- Venemans B. P. et al., 2012, *ApJ*, 751, L25
- Venemans B. P. et al., 2007, *A&A*, 461, 823

- Verhamme A., Schaerer D., Atek H., Tapken C., 2008, *A&A*, 491, 89
- Verhamme A., Schaerer D., Maselli A., 2006, *A&A*, 460, 397
- Wada K., 2008, *ApJ*, 675, 188
- Wagg J., Kanekar N., 2012, *ApJ*, 751, L24
- Wagg J., Kanekar N., Carilli C. L., 2009, *ApJ*, 697, L33
- Walch S. K., Whitworth A. P., Bisbas T., Wünsch R., Hubber D., 2012, *MNRAS*, 427, 625
- Walter F., Carilli C., Bertoldi F., Menten K., Cox P., Lo K. Y., Fan X., Strauss M. A., 2004, *ApJ*, 615, L17
- Walter F. et al., 2012a, *Nature*, 486, 233
- Walter F. et al., 2012b, *ApJ*, 752, 93
- Wang R. et al., 2010, *ApJ*, 714, 699
- Wang R. et al., 2013, *ApJ*, 773, 44
- Weiß A., Downes D., Neri R., Walter F., Henkel C., Wilner D. J., Wagg J., Wiklind T., 2007, *A&A*, 467, 955
- Williams R. J. et al., 2014, *MNRAS*, 439, 2096
- Willott C. J., Omont A., Bergeron J., 2013, *ApJ*, 770, 13
- Wolfire M. G., Hollenbach D., McKee C. F., Tielens A. G. G. M., Bakes E. L. O., 1995, *ApJ*, 443, 152
- Wolfire M. G., McKee C. F., Hollenbach D., Tielens A. G. G. M., 2003, *ApJ*, 587, 278
- Woosley S. E., Weaver T. A., 1995, *ApJS*, 101, 181
- Zaroubi S., 2013, in *Astrophysics and Space Science Library*, Vol. 396, *Astrophysics and Space Science Library*, Wiklind T., Mobasher B., Bromm V., eds., p. 45